Development of Monte-Carlo Simulation Model of the UiB Gamma-ray tomography system using MCNP

University of Bergen

Frida Jogole Sandtorv

Department of Physics and Technology

Faculty of Mathematics and Natural Sciences

A thesis submitted for the degree of Master in Measurement Science and Instrumentation

11. September 2019

Abstract

The purpose of this thesis project is to study and quantify the amount of Compton scattered radiation that is present in UiB GRT and to develop a benchmarked MCNP simulation model of the UiB GRT. Scattered radiation from adjacent sources, build-up and Rayleigh scatter introduce an error in the data that is used for image reconstruction in the UiB GRT, this causes less contrast and blurriness in the reconstructed image. The development of a MCNP simulation enables a further study of scattered radiation, which may lead to correcting measures that can be taken to improve image quality. In this thesis project a simulation model of the UiB GRT has been developed. This has been done by benchmarking the developed model to experimental and finding the parameters that minimize the chi-square sum, which was found when the density of the pipe-wall material PP was set to a density ρ=0.92 g/cm^3. Thus, this thesis has consisted of both simulations, experimental runs on UiB GRT and comparison between simulation runs and experimental response. By studying the scattered radiation with a medium inside the pipe, the total scatter contribution was studied. While the study of scattered radiation when the pipe is empty allows the study of scatter contribution that is mainly from the collimator blades and pipe-wall. Amount of Compton scattered radiation that is present in the MCNP simulation model and experimental measurements have been presented. An overestimation was observed in the developed MCNP simulation model, this may be due simplifications in the MCNP model geometry.

Acknowledgments

This thesis project is written in collaboration with the University of Bergen, Department of Physics and Technology, Faculty of Mathematics and Natural Science. And is submitted for the degree in M.Sc. degree of master in measurement science and instrumentation.

Frist I would like to give a big thanks to my co-supervisors Camilla Sætre at UiB and Ilker Meric HVL, thank you for guidance and support through this thesis project. I would also like to give a big thanks to Rachid Maad, who has been a great support and assisted me with collecting data from UiB GRT, software tools and practical tools. Moreover, thank you to Professor Bjørn Tore Hjertaker for always being available.

I am thankful for the support my family and husband Joachim Sandtorv has given, without your support and encouragement this thesis would not be submitted.

Contents

List of Figures

List of Tables

List of Abbreviations

CT	Computed tomography
GRT	Gamma-ray tomograph
HSE	Health safety and environment
HVL	Western Norway University of applied Sciences
LLS	Least-squares
MC	Monte-Carlo Simulation
MCNP	Monte-Carlo-N-Particle Transport Code System Version 6.2 EXE
M.Sc	Master of science
SRC	Saskatchewan Research Council's
UiB	University of Bergen

Chapter 1

Introduction

1.1 Background and motivation

Gamma-ray tomography involves imaging with a measurement system that has one or several ionising sources and one or several detectors. Ionising radiation is radiation with sufficient energy to ionize atoms in matter, thus making the atoms either positively or negatively charged. This kind of radiation includes both electromagnetic radiation such as gamma rays and X-rays, as well as energetic particles such as α- and β-particles [1]. Tomography comes from the Greek words *tomos,* which means a cut, a slice or a section and *graphein*, which means to write or record [2]. Tomography or spectroscopy allows imaging of the two-dimensional (2D) cross-section of a three-dimensional (3D) object. This is very useful for industrial purposes e.g. in the oil and gas industry where the distribution of flow components are of interest, as well as the well-known X-ray tomography which is used in medicine e.g. to locate or check for bone raptures [3]. Gamma-ray tomography or gamma-ray computed tomography (CT) is in high demand and of interest in many fields since they are none-invasive, which means that the measurement method does not disrupt the measurement volume, since they are usually installed with a clamp-on solution. This imaging modality has high precision, but are costly since they demand high health, safety and environment (HSE) requirements [1] [4] [5]. In gamma-ray tomography the fact that photons are attenuated when they pass through matter is exploited, the attenuation of a photon beam depends on the density and composition of the matter as well as the distance the photons travel in the matter and photon energy. Thus, the attenuation of the beam is nearly proportional to the density of the process flow [5]. Attenuation means a reduction in intensity, thus photoelectric effect, Compton scattering and Rayleigh scattering that are different interactions modes that photons go through result in photons being removed from the beam. Compton scattering leads to both attenuation of incident beam and degraded photon energy. In this thesis project the experimental data will be acquired from the University of Bergen's gamma-ray tomograph (UiB GRT), which was

originally developed by Geir Anton Johansen and Bjørn Tore Hjertaker at the University of Bergen. The UiB GRT consists of five radioactive ^{241}Am sources and five detector pentants that each consist of 17 semiconductor detectors. The detector pentants are oriented around the circumference of a pipe with an inner dimeter of 80mm and outer diameter of 88mm. When the sources decay, they emit gamma-rays with principal energy of 59.5keV that travel from the sources, through the pipe wall, through the medium or mediums inside the pipe and out through the other side of the pipe, till they are absorbed by the detectors. Due to the varying density in the multicomponent flow at a given time and the density of the pipe-wall, different amounts gamma ray photons will be able to pass through, thus attenuation occurs both in pip-walls and pipe medium [6]. Hence, the detectors are able to locate more dense and less dense areas in the pipe, the intensities in the different locations or projections from the five detectors pentants are imputed to an algorithm and a 2D image of the cross section is reconstructed, which represents the phase distribution inside the pipe. [6]. The UiB GRT was developed to be a reference instrument, used for imaging the cross-section of rapidly changing flow regimes. The UiB GRT is able to image a two-component flow where the components have differing densities, e.g. crude oil and gas have densities of $\varrho=0.83g/cm^3$ and $\varrho \approx 0.0012g/cm^3$, respectively. The cross-section images enable visualization of the distribution of the two phases in the pipe. To develop an image of the cross-section all sources in UiB GRT must be open, the number of detected counts in the detectors are inputted to the reconstruction algorithm that visualizes the cross section of the flow regime. A reference instruments may be of special interest for the gas and oil industry where a homogeneous mix of components in a flow is needed for accurate fraction measurements, for example a homogenous mix of oil and gas. Thus, the UiB GRT could be used to identify an inhomogeneous mix of components or for example restrictions which may be due an accumulation of a substance in the pipe diameter. By using the UiB GRT, a problem may be identified, and proper actions can be taken to obtain wanted flow conditions, e.g. increasing the flowrate to achieve a homogenous mix. The UIB tomograph permits visualization of the phase distribution of two components with differing densities e.g. oil and gas, which is information that would otherwise not be available to us. Figure 1 shows a 2D and 3D image of the UiB GRT.

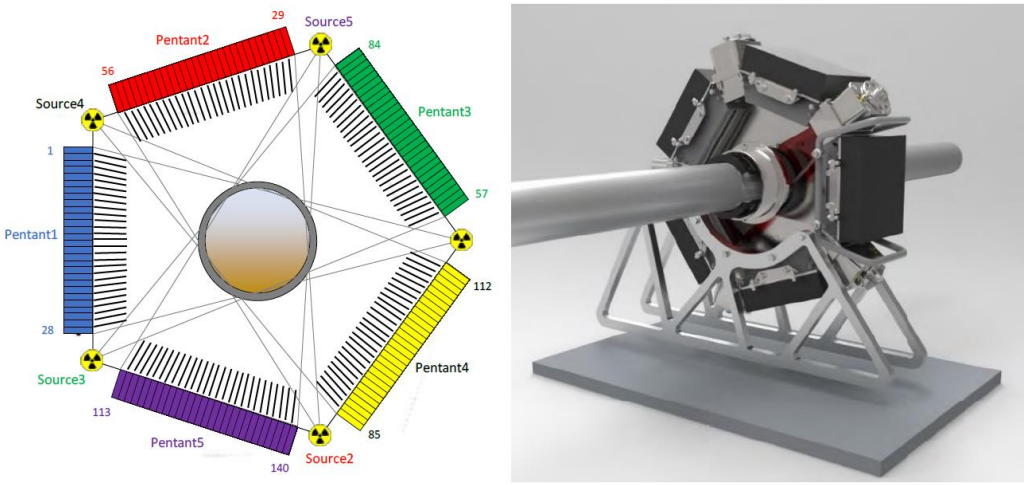

Figure 1. Schematic setup and illustration of UiB GRT setup. The image to the left shows the arrangement of sources, pentants (detectors), collimator blades and measurement volume. The image to the left shows a 3D image of the 3rd generation GRT that has been built in Sskatchewan Reaserch Concuils's (SRC). The UiB GRT is the 1st generation GRT and the SRC is based on the UiB GRT but with more advanced detectors, thus the 3D image on the left gives a good and accurate visualisation of the UiB GRT. The SRC GRT is build by CMR Prototech The image to the left shows 3D image of measurements setup as well the radiation beam path [7].

Ideally, we would want only the photons from a source that is positioned directly opposite of a detector module to be detected at the detector module, thus photons from source 1 to be detected at detector pentant 1, and so forth. This is not the case in real life, in real life we have scattered radiation. By scattered radiation, it is meant radiation that originates from a source that is not directly opposite of a detector pentant [8]. When the photons pass through the pipe walls, phantom and thereafter hit the detector, the photons will be attenuated through photoelectric effect, Compton scattering and Rayleigh scattering. Each of these interactions have an associated probability of occurring, which depends on the photon energy, atomic number of absorber material and atomic number of absorber material. Furthermore, since the gamma source energy is at an intermediate energy of 59.5keV, the probability of photoelectric effect and Compton will increase with higher atomic numbers, thus there is a greater probability of photon interactions in the pipe-wall and in a dense medium inside the pipe. In photoelectric effect the incident photon collides with an inner electron and completely disappears, this is followed by the ejection of a photoelectron and characteristic x-ray radiation. A characteristic x-ray has an energy which is equal to the energy difference of two atomic states in an atom. Compton scattering is the process where a photon gets scattered by an outer electron that can be seen as a "free electron", this process results in energy loss of the incident photon. Thus, some of the energy from the incident photon get absorbed by the "free electron". This results in the scattered photon having less energy than the indecent photon,

thus continuing in another direction and the ejection of the loosely bound electron from its orbit, thus ionization of the atom. Rayleigh scattering leads to no energy loss of the photon, however the photon might get scattered in a significant angle, which would lead to attenuation of a narrow gamma-ray beam. Rayleigh scattering is minor compared to Compton and photoelectric effect. Scattered radiation in a multiple source system is a well-known CT problem and results in reduction of the accuracy in the image that is being reconstructed by the acquired projection data, which is shown in the previous work of (R. Maad et al. 2008) [9] [8]. Maad's work concerned developing a semi-empirical model that describes the scattered radiation that occurs in the UiB GRT. This work was conducted by acquiring experimental data from the UiB GRT under different flow regimes, as well as with different gas and oil fractions. The scattered radiation from each source was recorded by having one active source at a time, and closing the other sources, and so forth. Based on this experimental data a semi-empirical model that describes the scatter contribution to each of the detectors was developed [9]. Semi-empirical means a model or equation that is created based on experimental data. Further work on the UiB GRT has been conducted by (I. Meric et al. 2015). The work conducted involved using a least-squares (LLS) approach to estimate the amount of scattered radiation from adjacent sources to a detector pentant. The LLS technique is based on the fact that all spectrums can be broken into components which can describe the spectrum in linear combination, which is also the basis of Fourier transform. Thus, any spectrum acquired by a detector can be broken into several components, where one component is due to transmitted photons and the other due to scattered photons. This is done by making a scatter library spectrum for each detector; the spectrum is acquired by shifting the threshold and recording photons counts at different thresholds to get a spectrum. Thus, if a spectrum with an unknown scatter contribution is recorded the unknown scatter contribution can be found by using the LLS library as a search engine. This search will find the two components of transmitted and scattered, which in linear combination will give the unknown spectrum. Both Maad's and Ilker's work are scatter correction methods that aim to correct for the error that is introduced in the experimental data due to scattered radiation that occurs in the UiB GRT. By correcting this error more accurate and fine data can be input to the reconstruction algorithm, thus resulting in a better reconstructed image. Further work has been conducted in Saskatchewan Research Council's (SRC) where a 3rd generation GRT has been built, this also been mentioned in Figure 1. The UiB GRT is the 1st generation GRT and SRC GRT has been appointed the name as 3rd generation since there has been done significant upgrade in the electronics. For instance, the SRC GRT has five detectors that each consist of 7

crystal where each crystal is composed of a matrix that is 16 pixels wide and 8 pixels high (16×8×7), which results in 4480 individual detecting pixel elements [7]. The detectors have energy resolution which enables acquisition of the energy spectrum directly from the meter. Maad's and Ilker's previous work has paved way for this thesis and is driven by the interest of further investigation of scattered radiation.

1.2 Objectives

Scattered radiation in a multiple source tomography setup is a known problem that leads to errors in the output data, which leads e.g. to less contrast and blurriness in the reconstrued image. Monte-Carlo (MC) simulation models are powerful tools that simulate the random trajectory of individual particles (photons), by using pseudo-random numbers and probability distributions [1]. The development of a MC simulation model that describes the UiB GRT enables the investigation and the acquisition of information that otherwise would not be available. The detector's in the UiB GRT do not have energy resolution, thus the detectors count number of photons hits above a set threshold of 48keV. A MCNP model of the UiB GRT can therefore be used to investigate a vast area of different properties like Compton scatter, build-up and Rayleigh scatter. All types of scattered radiation are a topic of interest since it decreases the signal-to-noise ratio and leads to less contrast in the reconstructed image. The scattered radiation introduces an error in the UiB GRT data that follows into the reconstruction algorithm. By quantifying the amount of scattered radiation, build up and Rayleigh scatter that occurs this error can be corrected for in the experimental data, thus image quality can be improved [9] [8]. The objective of this thesis project is to firstly develop a Monte-Carlo simulation model (MC) in Monte-Carlo-N-Particle Transport Code System Version 6.2 EXE (MCNP), that describes the UiB GRT. The benchmarking of the developed model will be done by comparing the MCNP model to acquired experimental data from the UiB GRT. Furthermore, fine-tuning of the MCNP model will be done by finding the optimal model parameters by using Chi-square test, this is done to ensure that the developed simulation model exhibits similar behaviour to true conditions. Secondly, the amount of Compton scattering in each detector pentant will be studied, and the results from the developed MCNP model and experimental data will be compared. Furthermore, in the UiB GRT all detected hits are assumed to be transmitted photons, even if they are Compton scattered, Rayleigh scattered

or build-up, this leads to additional noise and error. Transmitted photons are the photons that reach the detectors and are detected at the detectors. Thus, it is of interest to quantify the amount of Compton that is present under normal running conditions of the UiB GRT. Compton scattering is the most prominent scattering contribution. Lastly, the total amount of Compton scattering that is present under normal running conditions of the UiB GRT will be quantified by studying the results from the MCNP model and experimental. A comparison between MCNP model and experimental data will be done to see if there is any deviation. In this scope of work Rayleigh scattering and forward scattering will not be included. Rayleigh scattering is the process where the incoming photon gets scattered by the atom as a whole, without any energy loss. This process is often neglected since the probability of this interaction occurring is much smaller than photoelectric effect and Compton at intermediate energies [10]. Forward scattering or build-up is scattering that originates from the sources that is directly opposite a detector module, where the photon has undergone a scattering event before detection in the detector.

1.3 Approach

The following approach was used: Firstly, a simulation model input file of the UiB GRT was developed in MCNP. Secondly, the developed MCNP model was benchmarked to experimental data that was acquired during experimental runs of the UiB GRT. The benchmarking process of the simulation model is conducted numerically by using the chi-square test (goodness of fit), which finds the model fit that gives the lowest chi-square value, this is done to ensure that the model shows good agreement with true conditions. A lower chi-square sum indicates a better fit. The amount of Compton in each detector pentant has been quantified, as well as the amount Compton scattering that is present under normal running conditions of the UiB GRT. The amount of Compton scattering from experimental data and simulation model have been compared. Furthermore, an elaboration on uncertainties and assumptions that have been made in the developed MCNP model, benchmarking process and in the acquisition of experimental data have been discussed.

1.4 Outline

In this thesis project the following outline is used: Chapter 2 is a theory chapter that explains basic radiations physics, what gamma rays are and how they interact with matter. Chapter 3 gives an overview and explains how the UiB GRT works with a focus on the ^{241}AM source, scintillator detectors and measurement volume. In Chapter 4 the developed MCNP simulation model is presented and the working methods of MCNP are explained. Furthermore, an introduction to software tools that have been used in this project are presented. Chapter 5 presents experiments, simulation, results and discussion. In chapter 6 a proposal for future work is presented.

Chapter 2

Background theory of how gamma-rays interact with matter

In this thesis project, the UiB GRT will be further studied and analysed by developing a MC simulation model in MCNP. Thus, it is crucial to understand how photons interact with matter. The gamma rays that are used in the UiB GRT are produced from the ^{241}Am source that decays to ^{237}Np through alpha decay leaving the daughters in excited states, consequently emitting the full energy peak of Eγ=59.5keV. When the photons pass through the pipe walls, phantom and thereafter hit the detector the photons will be attenuated through photoelectric effect and Compton scattering. Both processes lead to a partial or total transfer of gamma ray photon energy to electrons. Attenuation of the bam leads to sudden and abrupt changes in gamma ray histories, since the photons either disappear completely or get scattered in significant angles. [11]

2.1 Basics of gamma-rays

This subchapter is meant to give a good fundament for understanding the processes that occur in the UiB GRT that will be discussed later. Thus, basic radiation physics and gamma radiation will be presented.

2.1.1. γ-ray basics

Electromagnetic radiation are waves that are composed of a time-varying electric and magnetic field. When a magnetic field or electric field varies with time, a field of the other kind will be induced in an adjacent region of space [12]. This changing of an electric field, which induces a magnetic field and vice versa composes an electromagnetic wave. Thus, an electromagnetic wave consists of a time varying electric and magnetic field [13]. Figure 2 shows the electromagnetic spectrum, which accounts for the most important frequency bands in nature. Despite the vast difference in use and production of the different bands, they are all electromagnetic waves that propagate through space (in vacuum) with the speed of light, $c=3\cdot10^8$m/s, they can even propagate if there is no matter [12]. Ionising radiation is electromagnetic radiation with enough energy to ionize an atom, hence changing the charge of an atom to positive or negative. This is done either by giving an electron sufficient energy to free itself from the atom or by acquiring an electron in the atom. From the electromagnetic spectrum Figure 2, the ionising radiation is found in the upper range of ultraviolet, X-ray, γ-ray, bremsstrahlung and annihilation radiation, all of these radiation types have enough energy to ionise an atom. Radiation are discrete massless bundles or quanta of energy called photons, this quantum mechanical approach of looking at photon as "particle" instead of a wave enables the description of how ionising radiations interacts with matter [1]. This principle of viewing a photon as a particle in some situations and as a wave in other situation is called wave-particle duality of light. The absorption of a photon by an electron and photon emission shows the "particle" behaviour of photons, while the diffraction and interference show wave behaviour. Thus, electromagnetic waves are not continuous, but the energy of an electromagnetic wave is quantized, it is emitted and absorbed in particle like massless packages called photons [12]. For frequencies under infrared, electromagnetic radiation is accurately described as a wave, while frequencies in the gamma and X-ray range they must be viewed as photons to describe the absorption, emission and scattering [14]. The interaction of ionising radiation with matter will be discussed later in this Chapter 3.

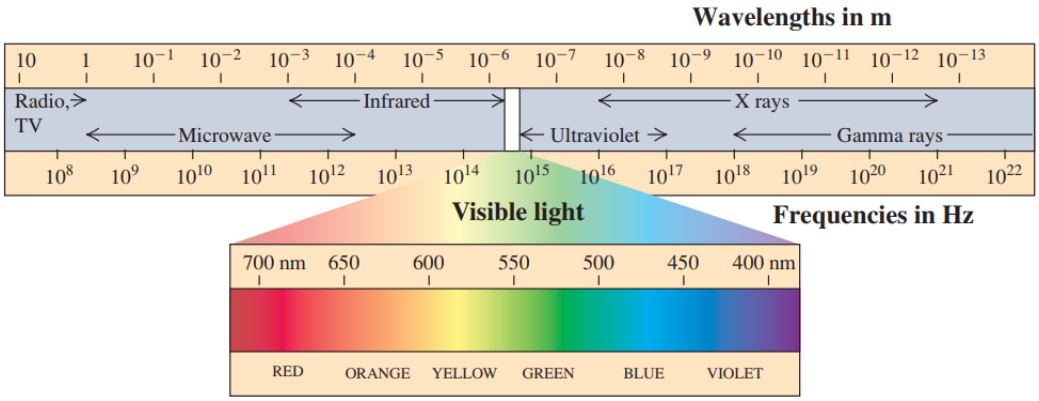

Figure 2. The electromagnetic spectrum. The spectrum extends over a broad range of frequencies and wavelengths in nature. The boundaries are somewhat arbitrary. *[12].*

Gamma rays are electromagnetic radiation with frequencies higher than approximately 10^{18} Hz, which is equivalent to wavelengths shorter than $1{\cdot}10^{-12}$m. They are produced when an excited nucleus wants to reach ground state, and the nucleus de-excites by emitting gamma rays. Alpha and beta decays are often followed by the emission of gamma rays from the nucleus, since alpha and beta decays often leave the nucleus in excited states [15]. Alpha and beta particles are charged particles that are emitted for heavier unstable atoms. An alpha particle is a helium nucleus while a beta particle is either an electron (e^-) or a position (e^+); the latter is the electrons antiparticle. X-rays are electromagnetic radiation with frequencies in the range of roughly 10^{16} to 10^{21}Hz, which corresponds to wavelengths in the range of $7{\cdot}10^{-7}$m to $7{\cdot}10^{-12}$m. X-rays can be produced in an x-ray tube and originate from the atom shells. From this, one can observe that the region of gamma rays and X-rays overlap, see Figure 2. [16]. X and γ-rays are both photons, but they differ due to their origin. Gamma rays are produced due to excess energy in the nucleus; hence, they originate from the nucleus. X-rays are produced due to an atomic process where electrons transition between atomic shells, the characteristic energy that is emitted is the energy difference between the two states, thus characteristic for specific atoms. The difference in origin of gamma rays and X-rays also place them in different energy ranges. Even though gamma rays and X-rays overlap, gamma rays are associated with having higher energies than X-rays, since they originate from the nucleus where the short-ranged strong force dominates. While X-ray origins from transition is the atomic shell where the weaker Coulomb force dominates.

2.2 Gamma-ray sources

When a radioisotope decays by emitting an alpha particle, the nucleus is often left in an excited state, thus it wants to reach the less energetic ground state, which often occurs by the emission for gamma rays from the nucleus. These gamma rays have specific energies, which are distinct for each gamma-ray source. The rate at which a radioisotope decays, thus emits radiation is given by the sources activity. Activity or A is defined as number of disintegrations per second which is the same as saying decays/s or s^{-1} and is given by [1]

$$\mathrm{A} = \left|\frac{dN}{dt}\right| \tag{2.1}$$

where dN is the number of nucleuses that will decay in the time dt. The SI unit for activity is Becquerel [Bq] where 1 Bq =1 disintegration per second, which is the same as decays/s or s^{-1}. However, the original or historical unit for activity is Curie where 1 Ci= 3.7×10^{10}Bq, this unit is frequently used today. The activity of a source decays exponentially as shown in Figure 3 [1].

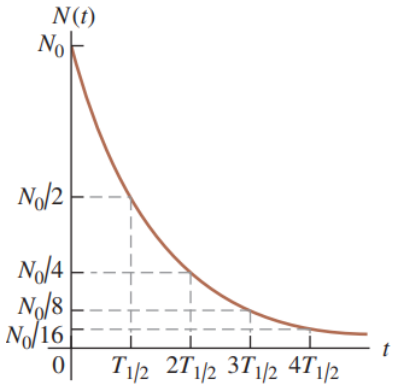

Figure 3. Decay of radioactive source. Half-life, $T_{1/2}$, is the time when half of the nuclei has decayed *[17]*.

Thus with time the source activity will decrease, meaning a reduction in photons per second. However, the signature energy spectrum hence full peak will stay the same. The rate of which nucleons decay in the period dt can be found from

$$\mathrm{dN} = -\lambda \mathrm{N}\ \mathrm{dt} \tag{2.2}$$

where λ is the decay constant with the unit [s^{-1}] or [decays/s] and N is the number of radioactive nuclei that all have the same probability λ to disintegrate in the time interval. The radioisotopes will not decay instant or simultaneously, they

will however decay in a random manner due energy fluctuations inside the nucleus. However, the average number of random decays that occur in a time interval can be predicted and is given by the decay constant λ [18].

2.2.1 Poisson distribution

Radioactive decay is a random and stochastic process; this means that each decay event is independent of the previous and following event. If number of counts from a radioactive source is recorded with a constant time interval, the number of detected photons will vary in this constant time interval when recorded several times. This occurs due to the random nature of radioactive emission, thus the time between succeeding radioisotope disintegration is not constant. For this reason, there is a corresponding uncertainty or statistical fluctuation. This fluctuation or spread of sampled data points can be studied through the Poisson probability distribution, since radioactive decay follows this distribution.

This random emission during radioactive decay forms a Poisson probability distribution, when an adequate amount of counts is recorded. Consequently, the integration time or observation time must be much smaller than the half-life of the source. From the probability distribution, we can observe the spread of data. The middle value on the x-axis that is shown in Figure 4 is the mean value, which would be number of counts at principal energy of 59.5keV for the ^{214}Am gamma ray source. The y-axis shows the probability; naturally, there is a higher probability of the sampled data point to be near the mean, since the probability is higher here. The standard deviation σ shows the spread in data points. Using a coverage factor of $\pm 1\sigma$ on the sampled parameter, means that we can say that we are 68.3% confident that the sampled value will be in the interval $q_{mean} \pm \sigma$. Thus, it follows that a confidence interval 2σ means that there is 95.5% probability that the sample value will lie within the interval $q_{mean} \pm 2\sigma$, and 3σ means that there is 99.9% probability that sampled value will lie within the interval $q_{mean} \pm 3\sigma$. However, 95.5% of the sample values will lie within $\pm 2\sigma$ and the rest outside. Figure 4 shows a normal distribution, the Poisson distribution is narrower and skewed, which can be seen on the right side of Figure 6, which shows the energy spectrum of the ^{241}Am source. [1] [18].

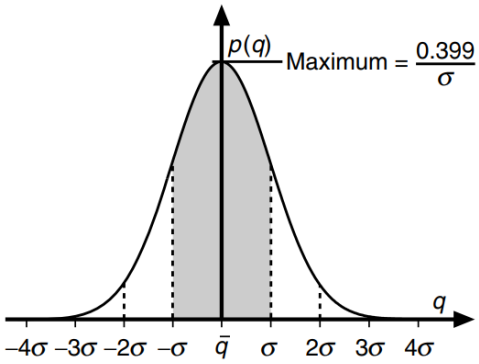

Confidence limits	Coverage factor k	Probability
$\pm\sigma$	1	68.3%
$\pm 1.645\sigma$	1.645	90.0%
$\pm 1.96\sigma$	1.96	95.0%
$\pm 2\sigma$	2	95.5%
$\pm 2.326\sigma$	2.326	98.0%
$\pm 2.576\sigma$	2.576	99.0%
$\pm 3\sigma$	3	99.9%

Figure 4. This is the Gaussian distribution where σ is the standard deviation and q is the observed or measured value. The shaded area within $q_{mean} \pm \sigma$ 68.3% of the total are of the envelope curve. For a large number of counts the Gaussian distribution adequately describes the radioactive nature, but in general, Poisson distribution is used. The difference between Gaussian and Poisson is that the Gaussian distribution is continuous as shown, while the Poisson denotes the number of time an event occurs, thus this figure should have been dotted and not a continuous line to show Poisson distribution *[1]*.

A Poisson distribution is a model of discrete events where the average time between successive events is known, which is given by λ for gamma ray emission. However, the exact timing of when an event occurs, respectively the exact time when a nuclei decays is unknown. For a radioisotope, thus for a Poisson distribution the standard deviation, σ, can be found from the equation below.

$$\sigma(n) = \sqrt{n} \tag{2.3}$$

where n is the number of photon counts. This approximation is valid when n is big (must be bigger that 100 counts) [1]. Furthermore, combined uncertainties have been calculated with the following equation below

$$\sigma_{combined} = \sqrt{\sigma_x^2 + \sigma_y^2} \tag{2.4}$$

where $\sigma_{combined}$ is the combined or total uncertainty of the system, while σ_x and σ_y are the individual uncertainty contributes of the system. Equation (2.4) can be used for calculating both combined uncertainties and combined standard deviation.

2.2.2 ^{241}Am source and spectrum

The high speed UIB GRT is equipped with five [1]500mCi ^{241}Am sources, each with principal energy of 59.5keV. These five ^{241}Am sources decay to ^{237}Np through alpha decay leaving the daughters in excited states, consequently emitting the principal mono-energetic energy of Eγ=59.54keV, which is given by the equation below. As stated in previous sections, the emission of alpha particles from a nucleus is often accompanied by the emission of gamma-ray emission, when the nucleus has been left in an existed state, thus the nucleus wants to reach ground state. The ^{241}Am has a half-life of 432.6 years, while the daughter ^{237}Np has a half-life of 2.144×10^{6} years. Furthermore, the more unstable a radioisotope is the shorter the half-life [19] [20].

$$^{241}_{95}\mathrm{Am} \xrightarrow{432.6\mathrm{years}} {}^{237}_{93}\mathrm{Np} + {}^{4}_{2}\mathrm{He} + \gamma 59.5\mathrm{keV} \qquad (2.5)$$

The decay scheme of the ^{241}Am source to ^{237}Np is presented below in Figure 5.

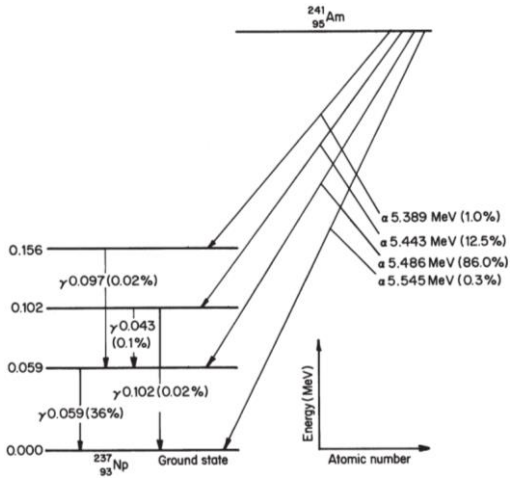

Figure 5. Decay scheme of ^{241}Am. Relative intensities are presented on the left scale. In addition to the competing decay modes and corresponding probabilities of their occurrence *[20]*.

[1] 1Ci is equal to 3.7×10^{10} decays per second or Becquerel (Bq). Becquerel is the SI unit for radioactive activity with the unit's decays per second or s^{-1}. Thus, 500mCi is equal to 18.5MBq.

From Figure 5 we can see that the ^{241}Am source has four competing or possible alpha-particle transitions modes, where each transition corresponds to a specific gamma ray energy. The alpha decay transition with the highest probability of happening is the 5.486MeV alpha particle with 86%, this alpha transition corresponds to the principal gamma ray energy of interest of Eγ=59.54keV. Thus, we can say that the principal gamma energy from the ^{241}Am source is 59.54keV. All radioisotopes that emit gamma rays have a characteristic output gamma-ray spectrum that cannot not be altered in quality; they also have a constant decay rate usually described in the terms of half-life [21]. Thus, all gamma ray spectrums consist of one or several discrete lines corresponding to the different gamma-ray transition modes. A ^{241}Am gamma-ray spectrum is shown below in Figure 6.

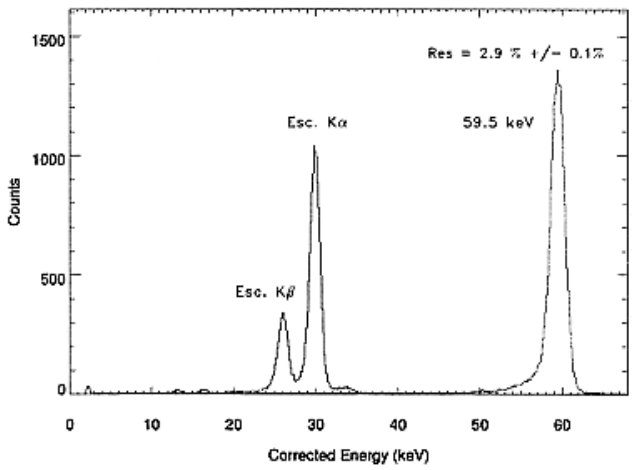

Figure 6. The graph shows the energy spectrum of Americium-241 source, which was recorded during a scintillation experiment, performed by researchers from the Research institute di Fisicia Cosmica in Palermo, Italy. In the spectrum, the full energy peak of 59.5keV for ^{241}Am can be observed. *[22]*

The alpha particles that are emitted from the ^{241}Am will ionise and deposit their energy inside the source housing, in the source windows and in air, thus they can be ignored. Consequently, the source ^{241}Am can be seen as a pure gamma-ray emitter. Alpha particles interact with matter in a very different manner than photons. Alpha particles lose their energy continuously through inelastic collisions with matter and come to a sudden halt where most of their energy is deposited, also called the Bragg-peak. The very ionising short-ranged alpha particle that consists of two protons and two neutrons (helium nucleus) is heavy and has a range of 5cm in air and can be stopped by a piece paper; thus, they will never reach the detector but disappear in the source housing. Some alphas will collide with the source housing and create ion pairs that will recombine when the alpha particles is gone, and the excess energy will be dissipated as heat.

2.3 Different modes of interaction with matter

In this sub chapter, the main interactions that occur when photons interact with matter will be discussed. These four main processes are photoelectric effect, Compton scattering, Rayleigh scattering and pair production. Which interaction process that dominates or takes place depends on the photon energy and the atomic number of the material that the photons pass through. Photoelectric effect is dominant at low photon energies in the range of 0-300keV and its dominance increases with increasing Z-number of absorber material [23]. Pair production is dominant at photon energies above 1022keV, while Compton scattering is dominant in between these two extremes, thus Compton scattering is dominant at intermediate photon energy levels (~500keV). Rayleigh scattering occurs in the same energy range as Compton scattering; however, the Compton scattering process is often the predominate process in this range; this will be further discussed later in this thesis project. The relationship between which interaction mode that will occur and their dependency on photon energy and atomic number of absorber material is shown below in Figure 7.

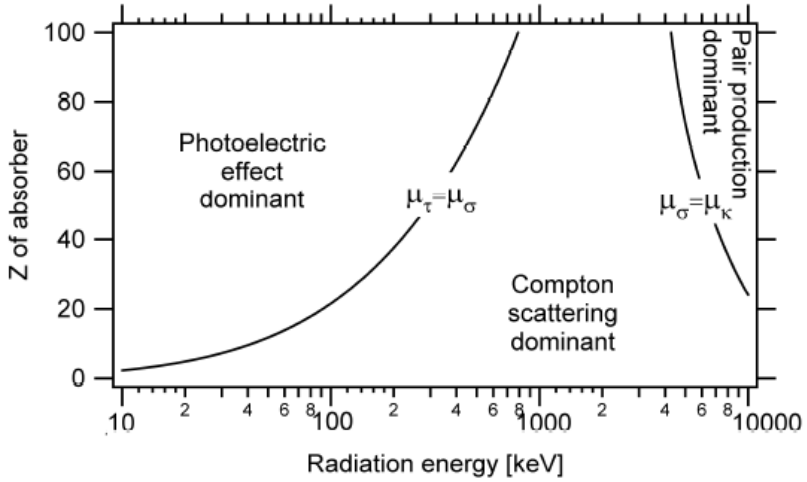

Figure 7. Graph illustrates boundary regions of where the different interactions are dominant. From the figure, we can observe that photoelectric effect (absorption) is dominant for low energies and high Z, while Compton is dominant for intermediate energies and low Z. Pair production μ_K will not be discussed since this phenomena happens at higher energy levels that the energy range of this project discussions *[1]*.

The ^{241}Am gamma source that is used in the UiB GRT emits photons with principal energy of $E\gamma$=59.5keV, for that reason the energy range of interest will

be 0 to 59.5 keV. The lower energy limit is set to 0keV, since Compton interactions with mediums will lead to loss of photon energy. In the energy range on interest 0-59.5keV the dominate modes of interaction will be photoelectric effect and Compton scattering, which mode predominate depends on the Z number of the absorber material, this can be seen in Figure 7. The pipe wall in the UiB GRT is made of Polyvinyl Chloride (PVC) which consist of carbon and hydrogen, with atomic numbers 6 and 1, respectively. Thus, there will a lot of Compton scattering. Rayleigh scattering may occur but will be neglected since it has a much less probability of occurring compared photoelectric effect and Compton scattering. In addition, pair production will not occur since the photon energy is too low for this interaction. For this reason, only Photoelectric effect and Compton scattering will be further discussed in this subchapter.

2.3.1 Photoelectric effect – absorption process

In the photoelectric effect a photon collides with an atomic bound electron, this results in the photon completely disappearing, thus a complete absorption of the incident photon. This process if followed by the ejection of a photoelectron and the emission of characteristic x-ray, due to rearranging in the atomic shells. The emission of characteristic x-ray occurs since an outer electron at a higher energy level, jumps down and fills the less energetic vacant position that the photoelectron has left empty. Thus, emitting an X-ray with an energy that is equal to the energy difference of these to energy states. All the energy from the incident photon is transferred to the electron; this statement is true for low energy photon in the range of a few hundred keV. The kinetic energy that the photoelectron is ejected with is equal to the energy of the incident photon, subtracted by the binding energy of the electron, as expressed below [18] [23].

$$E_{e^-} \approx h\nu - E_b \tag{2.6}$$

where $h\nu$ is the energy of incident or incoming photon, E_b is the binding energy of the electron and E_{e^-} is the kinetic energy of the ejected photoelectron. In order of upholding energy and momentum conservation laws, the energy of the incident photon must be greater than binding energy of a specific shell to eject an electron from the shell [18] [11]. The condition of the photon energy having to be larger than the binding energy of the electrons in a shell to eject an electron is clearly shown in Figure 8, where the cross section σ_τ is plotted against photon energy.

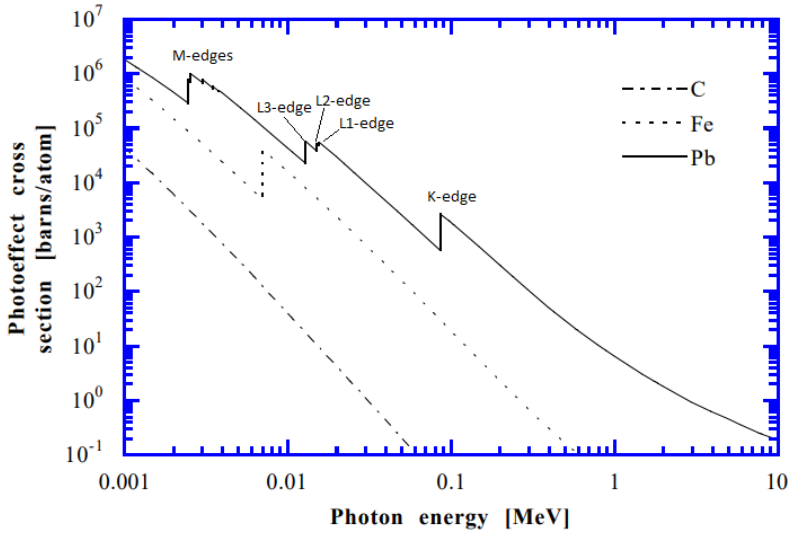

Figure 8. The plot shows the strong dependency of photoelectric absorption cross section on atomic Z number of the absorber material and photon energy. Carbon (Z=6), iron (Z=26) and lead (Z=82). From the plot we can see that lead, which is the absorber with the biggest atomic number has the greatest cross section, and that the cross section decreases with increasing photon energy. *[14] [24]*

The cross section σ tells us the probability of a photon interacting with a target atom per square meter, where the lower subscript τ indicates cross section for photoelectric effect [1]. From Figure 8 we can observe that the cross section for photoelectric effect is strongly dependent on photon energy E and the atomic number Z of the absorber. The edges in Figure 8 are called absorption edges and originate from the different binding energies in the different shells, thus we can see that the cross section increases drastically when the photon energy is just above the binding energy of a specific shell. Thus, photoelectric effect is most probable when the photon energy is just above a shell energy, if the photon energy is below a shell ejection cannot occur. Thus if the photon energy is below K shell, ejection from L can still occur but it is most probable when the energy is just above the shell energy [18] [11]. The photoelectric process is the predominate mode of interaction for low energy gamma rays and x-rays, and the process is enhanced for absorber materials with a high-Z. The order of magnitude of the photoelectric absorption cross section is given by [23]

$$\sigma_\tau \sim \begin{cases} \sim \dfrac{Z^4}{(h\nu)^3} & low\ energy \\ \sim \dfrac{Z^5}{h\nu} & high\ energy \end{cases} \tag{2.7}$$

From Equation (2.7), we can see that in the area of low photon energy the photoelectric effect will decreases with $1/E^3$ for increasing energies, where $E=h\nu$.

Moreover, at higher energies it strongly dependent on high-Z. However, as stated in previous section, photoelectric effect is predominant at low energies, thus at higher energy levels other interaction modes will be more prominent. Low photon energy and high absorber density Z results in the biggest cross section for photoelectric absorption, from this we see the dependency of σ_{pe} on E and Z for [25]. In the energy range of interest 0 to 59.5 keV, most of the energy after a photoelectric effect will be deposited near where the photoelectric effect found place. The photoelectron will not have sufficient energy to cause secondary ionization; it will rapidly lose its energy by inelastic collisions and deposit all of its energy near its original location [18]. The characteristic X-ray that is emitted may escape and cause an auger electron, which means that the X-ray escapes and ejects an outer electron. The characteristic X-ray can escape and cause secondary ionization which is ionization of a nearby atom, or secondary fluorescence, fluoresce means that the photon energy is in the visible light, thus causing illumination [26] [23]. An illustration of photoelectric effect and the different relaxations modes are shown below in Figure 9.

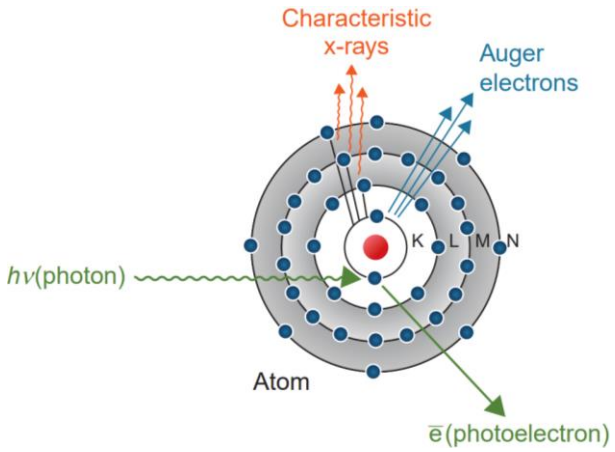

Figure 9. Illustration of photoelectric effect and the different relaxation modes *[17]*

2.3.2 Compton scattering - incoherent scattering

Compton scattering is the process where a photon gets scattered by a free atomic electron. A free electron in matter does not exist, since atomic electrons are bound in matter. However, an electron can be seen as free if the photon energy is much larger than the binding energy of the electron. Thus, Compton scattering occurs with outer electrons since they have the least energy. The Compton scattering does not lead to absorption of the photon. This process results in a less energetic photon continuing in a different trajectory and a scattered electron that carries away the energy that the incident photon lost in the collision [10] [27]. Another word for Compton scattering is incoherent scattering, which means that the

scattering process leads to a loss of photon energy, thus an inelastic process. The kinematic of the Compton scattering process is shown below in Figure 10.

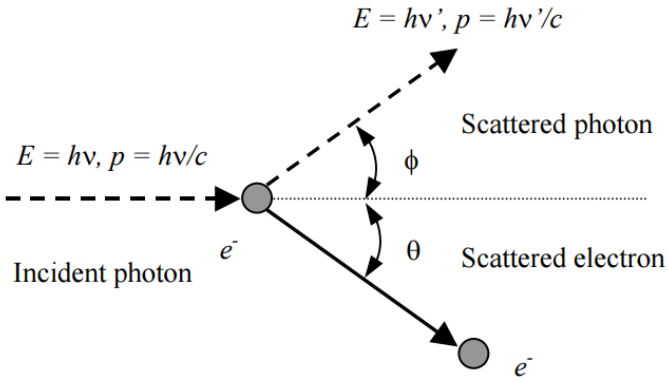

Figure 10. Illustration of the Compton scattering process.

By applying the laws of momentum and energy conservation, and assuming negligible binding energy for the electron, it can be found the scattered photon will have an energy that is equal to [1] [10]

$$E_{\gamma'} = \frac{E_\gamma}{1 + \frac{E_\gamma}{m_e c^2(1-\cos\varphi)}} \tag{2.8}$$

where $E_{\gamma'}$ is the energy of the scattered photon, E_γ is the incident photon, φ is the scattering angle of the photon and $m_e c^2$=511keV is the electron rest mass energy [1]. The energy of the scattered electron can be found by subtracting the energy of the scattered photon from the energy of the incident photon. When the photon is scattered at small angles (φ <10°) there is a small energy transfer to the recoil electron, hence the energy of the scattered photon is almost the same as the incident photon. Thus, the greater the scattered angle of the photon the more energy gets transferred to the electron, with a maximum energy transfer when photon backscatters φ=180° and the recoil electron continuous straightforward θ =0°, this phenomena is also called direct hit [1] [28]. High-energy photons are scattered in a forward direction; thus, their energy is almost the same as the incident photon. While low-energy photons scatter in all directions including backscatter [29]. For the ^{241}Am sources that are used in the UiB GRT that emit E_γ=59.5 keV, backscattering and scattering in all directions will occur since the photons have low energy. The Compton scattering process is the predominate process at intermediate gamma ray energies (~1MeV) and materials with loosely bound electrons which can be found in both high and low Z materials. The order of magnitude of the Compton scattering cross section is given by [23] [25].

$$\sigma_\sigma \sim \begin{cases} \sim ZE \; low \; energy \\ \sim \dfrac{Z}{E} \; high \; energy \end{cases} \tag{2.9}$$

The probability of Compton interaction per atom of the absorber depends on the number of scattering electron targets that are in the vicinity of the incoming photon. Since the Compton scattering process essentially is an interaction between free electrons, an increase in electron target electrons leads to an increase in the Compton scattering cross section. Thus, Compton interaction is independent of Z and solely dependence on electron density and photon energy [11]. Compton scattering is an interaction between a photon and a free electron the photon energy must be large compared to the electron binding energy. As stated in the previous section, the cross section for photoelectric effect increases strongly when the photon energy is slightly above the electron binding energy, hence the edges in Figure 8. Thus, when the photon energy increases beyond the binding energy of K-shell electron, which are the most tightly bound electrons, the photoelectric cross section decreases rapidly and the Compton cross section increases and becomes more are more important [17] [30]. Figure 11 shows dependency of the Compton scatter cross section as function of photon energy.

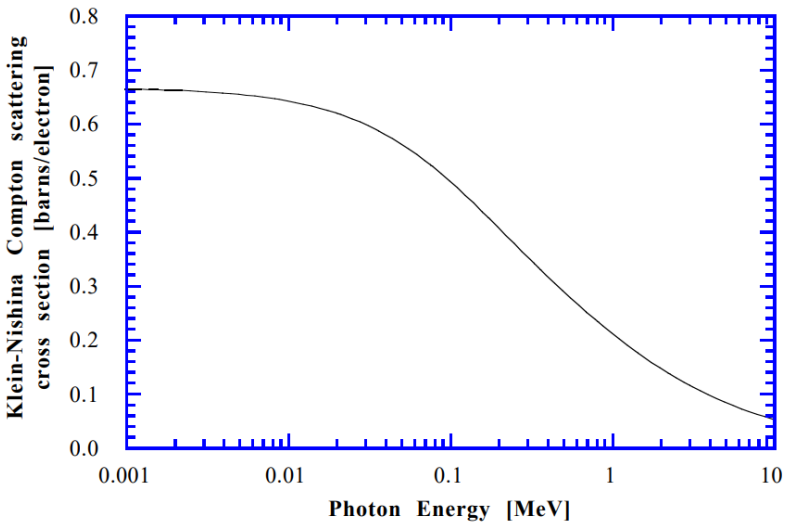

Figure 11. The plot shows the Compton cross section as a function of energy. At higher energy levels, the cross section for Compton scattering decreases with 1/E, which is also shown in Equation (2.8). This is due to an increasing cross section for pair production at energy levels above 1.022MeV pair production becomes the dominant interaction process. *[14]*

From Figure 11 and Figure 7 we can see that Compton scattering is dominant at intermediate energies. When the energy increases the Compton scattering cross section decreases since the competing process pair-production that occurs for at energy equal to or above 1.022MeV becomes more dominant.

2.4 Interaction of low energy gamma radiation Eγ = 59.5 keV with matter

From the discussion above, we can see that the gamma radiation from the ^{241}Am with energy of E_γ=59.5 keV will interact with matter either through photoelectric effect where the photons completely disappears. Alternatively, photons will interact through Compton scattering where the photons will be scattered in all directions which in most cases will lead to photons being deflected away and prohibited from reaching the detector. In the UiB GRT all photons that are detected in the detectors are assumed to be transmitted. However, we know that these transmitted consist of both photons that have undergone no interaction before detection ergo un-collided photons, and scattered photons that have decreased photon energy [27]. The amount of attenuation that occurs in a photon beam depends on the density and composition for absorber material, as well as photon energy. A photon with higher energy can travel farther that a photon with lower energy before interacting in the same absorber material.

2.4.1 Linear attenuation coefficient μ, cross section σ and build-up scatter

Let us consider a highly collimated beam of mono-energetic photons that travel through a slab of homogenous material with thickness t, shown in Feil! Fant ikke referansekilden.. This is more or less the same scenario as for the UiB GRT, where photons from the ^{241}Am source travel through the pipe-wall, phantom and pipe-wall, followed by detection on the other side. The total probability per unit length for the removal of photons from the beam or photon attenuation is called the total linear attenuation coefficient, μ (usually in units cm^{-1}). This coefficient is composed additively and is simply the sum of the respective probabilities for the independent interactions photoelectric effect (μ_τ), Compton (μ_σ) -and Rayleigh scattering ($\mu_{\sigma R}$), as shown below [27] [1] [24]

$$\mu_{tot} = \mu_\tau + \mu_\sigma + \mu_{\sigma R} \tag{2.10}$$

The linear absorption coefficient μ_{tot} depends on the photon energy and the atomic number of the absorber; thus, the type of interaction that occurs per unit length depends on the photon energy and atomic number of the absorber, see Figure 7. The cross section σ is the probability of a photon interacting with a target atom

per atom square meter. σ has the unit barns, which is equal to $10^{-24}cm^2$. The total cross section is the sum of this interaction mechanisms and is given by [1]

$$\sigma_{TOT} = \tau + \sigma + \sigma_R \tag{2.11}$$

The cross section σ is related to the linear attenuation coefficient μ by

$$\mu_{tot} = \mu_\tau + \mu_\sigma + \mu_{\sigma R} = \frac{N_A}{A} \cdot \rho \cdot (\tau + \sigma + \sigma_R) = N \cdot \sigma_{TOT} \tag{2.12}$$

where N is the number of atoms per unit volume, N_A is Avogadro's number which is equal to 6.02252×10^{23}, A is the average atomic mass (or molecular mole weight) and ϱ is the density in g/cm^3. Thus, as stated above the different interaction modes have their independent linear probability of occurring. From Equation (2.12) we observe that the linear attenuation coefficient also depends on the density of the absorber material, which implies that it to some extent depends on the physical state or composition of the material (liquid or vapour phase) [1]. To avoid the dependency of physical state of the absorber material the mass attenuation coefficient μ/ϱ is often used, since it is independent of density.

The fractional loss of intensity as the mono-energetic beam passes through a homogenous material is given by Lambert Beer's exponential decay law:

$$I(t) = I_0 e^{-\mu(E,Z)\cdot t} \tag{2.13}$$

where I_0 is the incident or initial intensity, x is the thickness of the absorber, I is the reaming beam intensity and μ is the linear attenuation coefficient [1].

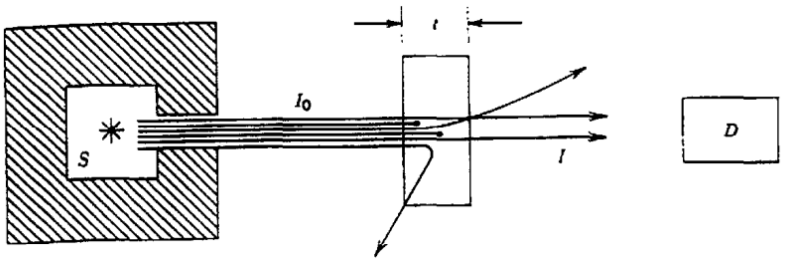

Figure 12. An experiment to measure the experimental absorption of mono-energetic gamma radiation as they pass through an absorber material with thickness *t*. The source is well collimated so that scattered radiation in the source is absorbed here, the intensity I reaches the detector. The intensity of the photon beam decays exponentially as it passes through the absorber material. Narrow beam/good geometry *[27]*

This scenario of a well-collimated beam or narrow beam as discussed above is usually not the case in real life. Thus, the simple exponential attenuation of the beam that is given by Equation (2.13) is violated in real life due to "broad beam" and "bad geometry". In real life measurements, the severe collimation of a gamma

ray source that leads to narrow beam is usually absent. Collimators are materials with high density and atomic number that are used for shaping and definition of a beam or beams, these same materials are used as shielding material for radioisotopes, due to their ability of absorbing high energy levels. However, the source intensity decays with distance from the source location, since we get a broad beam with a cone shape. This effect of decreasing source intensity with distance from source can be enhanced by bad geometry, see Figure 13 [1] [4] [11].

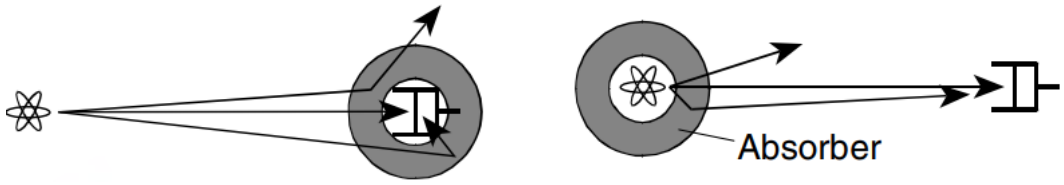

Figure 13. These figures illustrate broad beam or bad source geometry. The figure to the left shows the cone shape of the beam as the photons move away from the source location. The figure on the right shows forward scattered photons being detected as well as photon that are scattered out *[1]*.

In addition, in real life measurements build-up must be accounted for. Build-up also called forward scattering, are photons that are detected in the detector that have undergone a scatter interaction before detection, this is shown in Figure 9Feil! Fant ikke referansekilden.. In most cases, the detectors will not be able to distinguish between photons that are transmitted directly from the source, gamma rays that have been scattered in the absorber or other types of secondary interactions before reaching the detector. This is the case for the detectors in the UiB GRT.

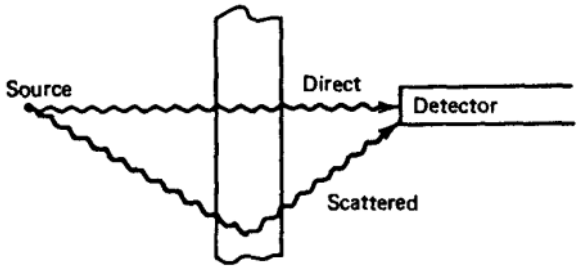

Figure 14. Illustration of transmitted photons where the first interaction process occurs in the detector; in this figure this process is called "Direct". While the other photons in this figure are forward scattered photons also called build-up. In this figure build-up is referred to as "Scattered".

By introducing a build-up factor B a simple multiplicative correction can be done.

$$I(t) = B(\mu, t) I_0 e^{-\mu(E,Z)\cdot t} \tag{2.14}$$

The build-up factor cannot be found analytically by solving an equation; it must be determined from experiments or through MC simulations. Build-up depends on linear attenuation coefficient and its composition, as well as the thickness and

geometry of the material the scatter occurs in. The source of build-up is normally due to Compton scattering. The measurement volume itself, the pipe-walls surrounding the phantom, the source shielding and detector housing are common build-up and scatter sources. One way of reducing unnecessary build-up and scatter is by using high-Z materials rather that low-Z materials in housing, e.g. to increase the probability of full absorption, as well as efficient collimation. MC simulations tool are powerful and can quantify amount build-up and Rayleigh scattering. The simulations models that has been developed in project can be used to quantify the amount of build-up and Rayleigh that occurs in the UiB GRT [1] [11].

2.5 Experimental measurement methods

This subchapter presents the methods that have been used on the experimental data from the UiB GRT to achieve minimize statistical fluctuations of the data.

2.5.1 Chi-square test – a goodness of fit test

The chi-square test has been used to evaluate the developed MCNP simulation model, to ensure that the simulation model shows a good agreement with the sampled experimental data. This test is used when the observed random parameter follows a particular distribution, the purpose of the test is to compare a sampled experimental distribution with a theoretical distribution for various values and see if there is a good agreement. Subsequently, the χ^2-test has been used to benchmark the developed simulation model to the sampled experimental data. Moreover, the chi-square test has also been used to compare the effect different fine-tuning methods have on the simulation model. By, comparing the chi-square value for different fine-tuning approaches, the best geometry parameter for the model can be found. The chi-square equation is given by

$$\chi^2 = \sum_{i=1}^{n} \frac{(y_i - f_i)^2}{f_i} \tag{2.15}$$

where χ^2 is the chi-squared value, y_i is the observed value, f_i is the expected value or true value and subscript i indicates a specific detector in a detector module. The best simulation model fit is obtained for the smallest χ^2 value; thus, we want to minimize the chi-squared sum that is given by Equation (2.15). Ergo, the smaller the χ^2 value is, the better the fit. The chi–squared sum is often referred to as the sum of residuals, since the χ^2 value is the sum of several values, as can been seen in the equation below [31] [20]. A criterion for the use of this model is that all observation must be independent of each other, which is exactly the case for a disintegrating radioisotope [1]. The chi-square test is used to compare a theoretical distribution, thus true value, to sampled experimental data of a population. The experimental data from the UiB GRT is assumed to be the expected value or true value, since these are the actual measurements. Furthermore, a radioactive decay process follows a Poisson distribution, thus the UiB GRT measurements are a theoretical model that can be used in the χ^2-test. The MCNP model is assumed to be the observed value with a negligible

uncertainty, since the MCNP has an uncertainty which is equal to or less than 0.01% for successful simulation runs.

2.5.2 Moving mean

To minimize the statistical fluctuation of the experimental data that has been acquired from the UiB GRT, a moving mean has been applied to the experimental data. Moving mean eliminates fluctuations in data sets which makes the trends of the data sets more apparent. For this reason, the moving mean filter has been applied to the experimental in the benchmarking process of the MCNP model to experimental data, to ensure the best possible fit between experimental data and the developed MCNP simulation model. The moving mean filter smooth in MATLAB has been used on the experimental data, since a good agreement was observed between the experimental data and the experimental data that has been applied with the smooth filter. Smooth calculates the mean of all preceding data points and the two following data points in the data set. The endpoints are not smoothed out, hence the first and last point of the data set does not change.

Chapter 3

UiB GRT

The UiB GRT was originally developed by Professor Geir Anton Johansen and Professor Bjorn-Tore Hjertaker at the University of Bergen. It was developed to enable high-speed pattern imaging for hydrocarbons in a two-phase flow; thus, to be used as a reference instrument for multiphase flow meters (MPFMs). Consequently, the UIB GRT is designed with a high temporal resolution of a few milliseconds to enable pattern imaging of rapidly changing flow regimes. The UIB GRT is a none-intrusive flowmeter, which means that it does not disrupt the flow regime. It enables imaging of two components with differing densities, e.g oil and gas or water and gas since, typical densities for hydrocarbons are $\varrho_{gas} \approx 0$ g/cm^3, $\varrho_{crude\ oil} \approx 0.83$ g/cm^3 and $\varrho_{process\ water} \approx 1$ g/cm^3 [1] [19] [32].

MPFMs that are used for measuring mass flow rates for gas, oil and water in production pipes have shown a considerable growth in sales in the past decades. They operate by combing instantaneous velocity and cross section fraction measurements of the individual components that the hydrocarbon flow consists of, ergo finding the mass flow rate of each phase. The MPFMs are dependent on having a homogenous mix of hydrocarbons in the flow to achieve an accurate fraction measurement. One of the major measurement errors in MPFMs are the variations in flow-regime of the distributions of gas and liquid in the measurement cross section of the pipe. The type of flow regime in the pipe depends mainly on the component velocities and fraction, as well as fluid properties and orientation of the pipe. Thus, the varying liquid/gas or water/gas distribution leads to errors in fraction measurements since they lead to different amount of attenuation along the beam, thus causing deviations in measurements fraction unless corrected. The UiB GRT was therefore developed to be used as a reference meter for MPFMs, to enable visualisation of the phase distribution in the cross section of the pipe. The information from the UiB GRT can be used to correct inhomogeneity in the cross section of the pipe, as well as other unwanted occurrence that may be present in cross section. By using the extra information that the UiB GRT provide, correcting measures may be taken e.g. increasing flowrate in MPFMs to achieve the wanted flow regime. The main application for industrial tomography in the petroleum industry is to provide additional information and enable further improvement of methods, models processes and equipment. [1] [33].

3.1 UiB GRT setup

The UiB GRT consists of five 500mCi ^{241}Am radioisotope sources, each with principal gamma-ray energy of 59.5keV. Furthermore, the meter has five detector modules that each consist of 17 CdZnTe semiconductor detectors, which gives 85 detectors in total. By module, it meant the whole detectors and detector housing, thus the whole detectors setup. All the 85 detectors have associated read-out electronics, which are optimized for high-speed imaging [33]. The detector pentants and detectors are oriented around the circumference of a pipe with an inner diameter of 80mm and an outer diameter of 88mm. The fan beam sources face the grid-collimated detectors as shown below in Figure 15.

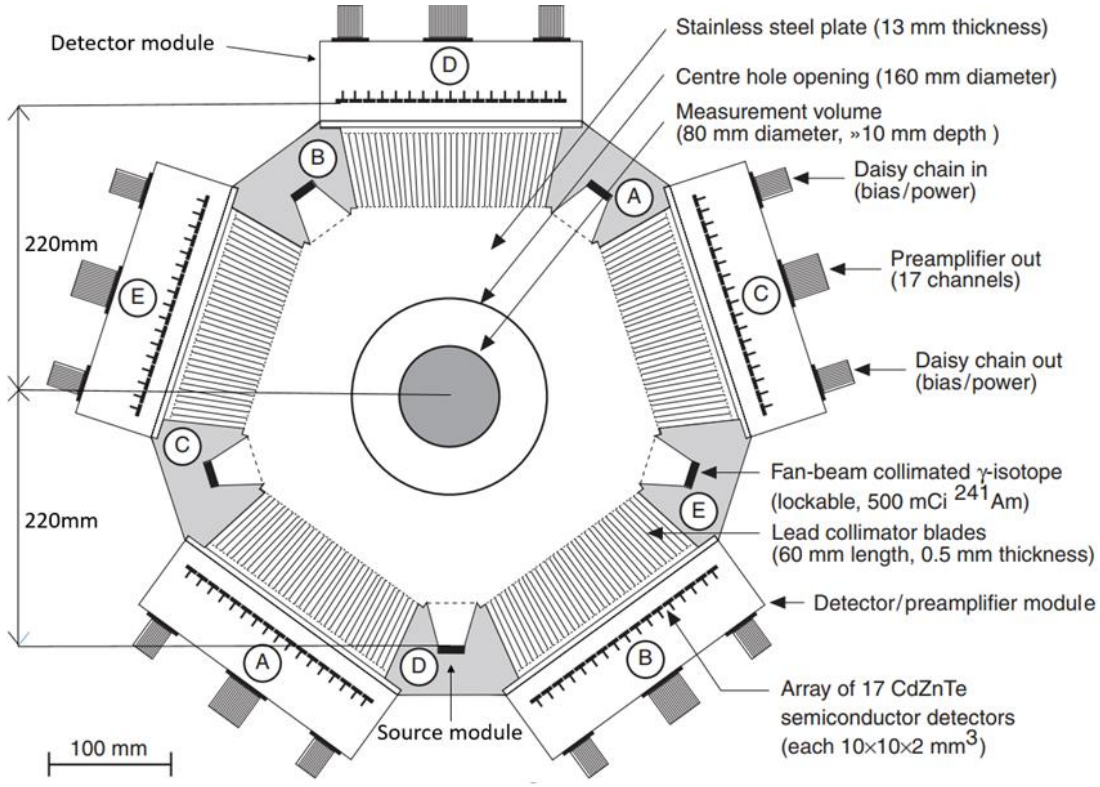

Figure 15. Geometrical design of the 85-channel UiB GRT with five sources and five detectors that face each other. For subsequent measurements, the detectors are numbered anti clockwise, so that detectors 1-17, 18-34, 35-51, 52-68 and 69-85 are in modules A-E or 42-46, respectively. The distance between each collimator is 0.5cm [9] [19].

3.2 Source module

3.2.1 Source module geometry

The source geometry of the UiB GRT is shown in Figure 16, each of the source are fan beam collimated sources that face the grid collimated detectors [34].

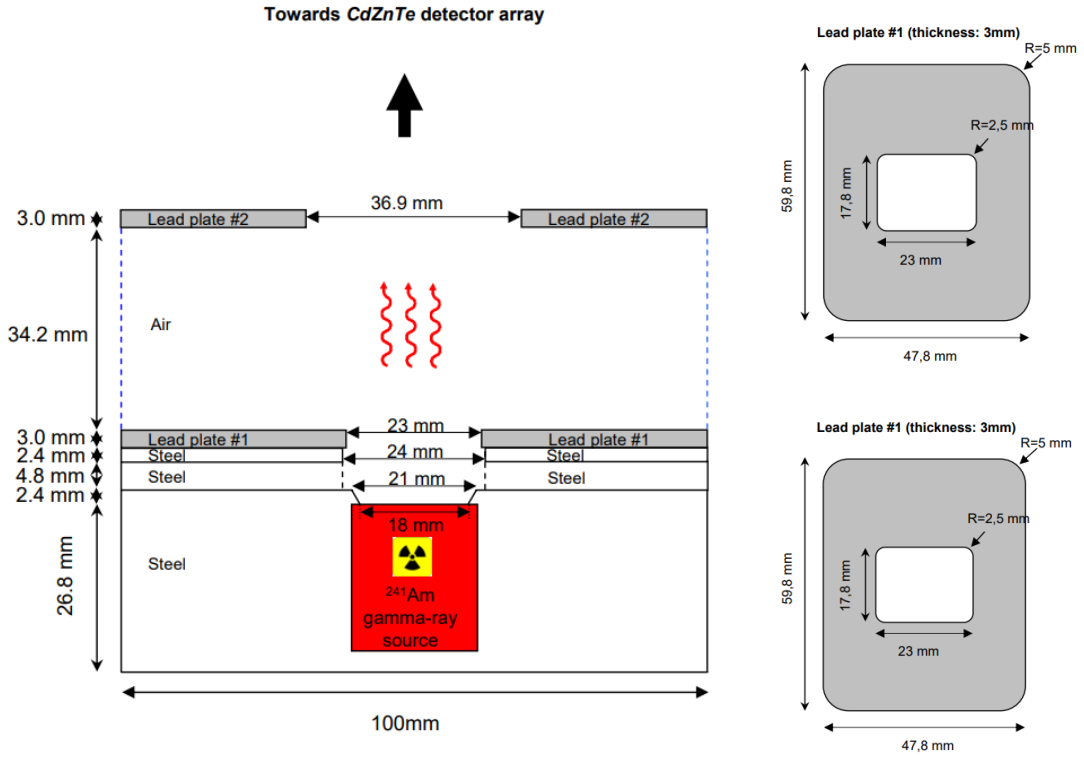

Figure 16. Source geometry of the UiB GRT verified by R.Maad, G.A. Johansen and BT Hjertaker, November 2, 2011.

From Figure 16 we can observe that the ^{241}Am source is collimated with lead (Z=82) collimators in two-steps by an inner -and outer collimation window of with the same dimension 17.8×23mm. As stated previously, collimators are materials with high density and atomic number that are used for beam shaping and definition. Thus, they cause scattered photons to be absorbed, ensuring that only transmitted photons exit the source housing, hence they limit the influence of scattered radiation [9]. Transmission windows or entrance windows or simply windows, is the detector housing, wall or encapsulation that faces towards detectors. A 3D drawing of the source housing is shown below in Figure 17.

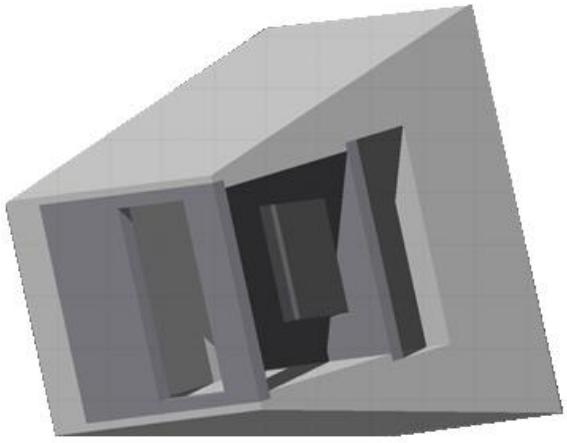

Figure 17. 3D plot of the source module, that shows the fan-beam collimation of the sources. A cut is made in the through the detector to expose the inner details (cut through ZY-plane). *[34]*

From Figure 17 we can see that the source module is fan beam collimated, this can be seen from the shape of the source housing. The fan beam collimation shape is clearly shown in the Figure 18, these plots give a good visualization of the source modules.

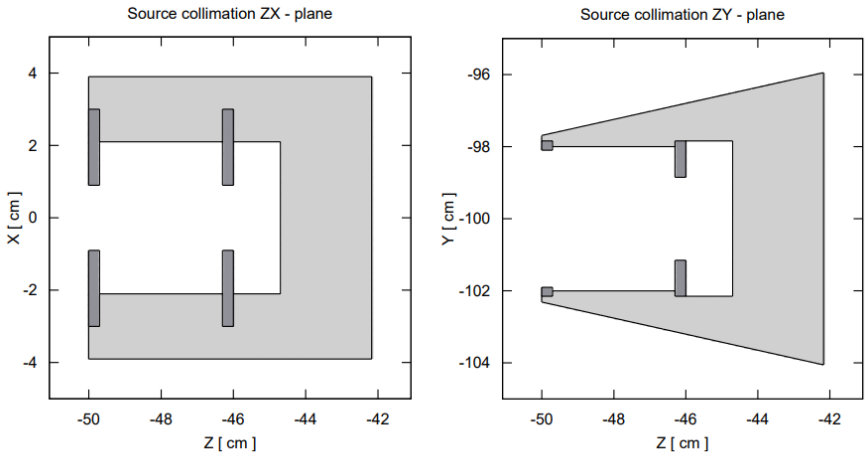

(a) *ZX plane.* **(b) *ZY plane.***

Figure 18. Cross section plots of the source module. In both source plots a cut as been made through the source module to expose the inner geometry. These plots are developed by Ketil Roed *[34]*

From Figure 18 we can clearly see the shape of the source modules. In the MCNP simulation that has been developed for the UiB GRT, there is no need to implement the specific geometry for the source, source housing and source collimation, ergo the source module. In Chapter 4, an energy distribution that is similar to the energy distribution of the whole source module has been setup. This topic will be further discussed in Chapter 4.

3.3 Detector module

3.3.1 Working methods of semiconductor detectors

The purpose of radiation detectors is to convert radiation energy to an electrical signal. In a semiconductor, this is done by producing secondary electrons that can be detected as an electrical signal, since they can be sensed and read by electronic equipment. The production of secondary electrons for measurement and detection of ionising radiation is a requirement in all measuring methods of ionising radiations. Semiconducting materials are materials with a valence bound that is full of electrons and an empty conducting band. The energy gap between the valence band and conductive band is not so large. For sake of comparison, conducting materials have a small energy gap, in addition they have electrons in both conducting -and valence band. On the other hand, isolating materials only have electrons in the valence band with a very big energy gap between valence and conducting band. Figure 19 schematically illustrates the basic structures of semiconductors, conductors and isolators, consisting of a valence band, a "forbidden" energy gap and a conduction band [10].

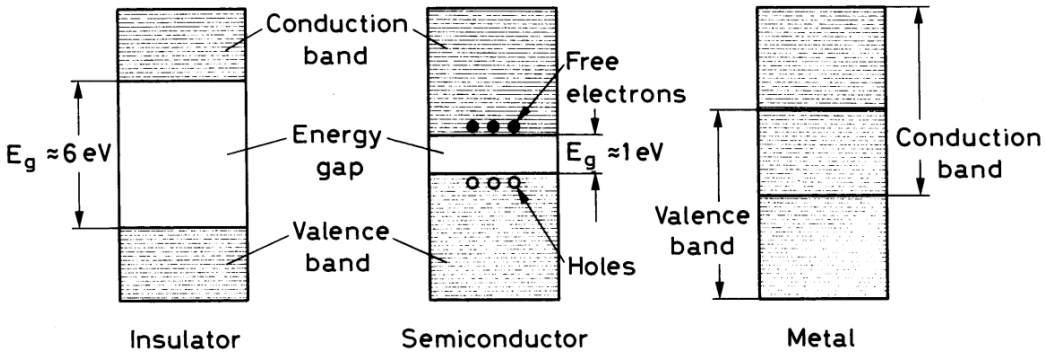

Figure 19. Energy band structure of conductors, insulators and semiconductors that shows the valence band, conductive band and energy gap *[10].*

The incoming photon hits the active area of the semiconductor causing excitation ergo ionization of an electron to the conductive band. This creates an electron-hole pair, thus a positive hole in the valence band and an electron in the conductive band. The holes and electrons can move in the valence band due to the positive holes and negative electrons, which leads to the creation of an electric current that can be detected by electronic equipment. Thus, detection of gamma radiation is done by detecting secondary ionization. Secondary ionization is the production of electrons that are produced due to gamma ray interactions with matter through photoelectric effect where a photoelectron is produced.

Alternatively, through Compton where a recoil electron is produced or auger electrons. From these discussions about photon interaction modes, we can observe that the same interaction processes that occurs when photons travel through the pipe-wall of the UIB GRT and source housing also occur in the detector. Consequently, these interactions allow the detection of gamma-ray radiation. The secondary ionization or secondary electrons enable the detection of gamma-radiation. The performance of a detector depends on its ability of efficiently producing secondary electrons and converting them to an electric signal, which can be sensed by the read-out electronics. In the UiB GRT the charge signal is read out in pulse mode which means that the total charge produced from each event is processed separately, by processed it is meant filtering and amplification. Pulse mode read out systems outputs a trail of pulses that correspond to the number of photons that hit the detectors. This readout mode gives information about timing and energy of individual photons if the detectors have energy resolution, which is not the case for the UiB GRT. In the UiB GRT an integration time is set manually and number of photons in the integration period is counted and displayed for each of the individual detector [1]. The detectors in the UiB GRT do not have energy resolution, thus a threshold is set and all events above this energy threshold is counted. As stated previously, Rayleigh scattering neither excites nor ionizes an atom, therefore no energy deposition or energy transfer occurs, thus no production for secondary electrons. To detect which photons that has been undergone Rayleigh scatter, a simulation like MC must be used by flagging or tracking photons. This would give us information about which full energy peaked photons have undergone an interaction before detection, hence Rayleigh scattered photons.

3.3.2 Detectors in UiB GRT

The high-speed UiB gamma-ray tomograph consists of five detector modules that each consist of 17 CdZnTe semiconductor detectors, which gives a total of 85 detectors. These 85 detectors are associated with read-out electronics, which are optimized for high-speed imaging [33]. Each of the individual detector in the UiB GRT has an active area of 10×10 mm and a thickness of 2 mm. By active area, it is meant the area on the detector where every radiation interaction contributes to the output signal of the system. Interactions that occur outside the active volume, e.g. in the pipe walls and detector housing do not contribute to the output signal, unless secondary interaction from these events reach the detectors [1] [34]. A detector thickness of 2 mm is used to secure a stopping efficiency of nearly 100%. To be able to measure ionising radiation, secondary electrons must be

produced in the detectors, thus ionization must occur in the detector material. Hence, it is important to ensure that the semiconducting material that is used is able to attenuate the beam, hence absorb or stop the photons that hit the detectors, which is done through photoelectric effect, Compton scattering and auger electrons. Consequently, we talk about detection efficiency or stopping efficiency of detectors, which is the detectors ability to attenuate the beam and produce an electric pulse. The stopping efficiency is the ratio of number of photons interacting in detector, thus creating a pulse, to number of incident photons to the detector. A detectors ability to stop photons is crucial to achieve an exact and precise output signal, ergo radiation measurement. The detection efficiency is dependent on attenuation coefficient through its radiation energy and the density and atomic number of the detector material. In addition to the thickness of the detector material [1] [33]. A 3D source geometry of the UiB GRT which is developed by Ketil Røed is shown below in Figure 20. The middle collimator that are placed in the middle of each detectors has not been included in Figure 20. Regardless, Figure 20 gives a very good visualization of the full detector module.

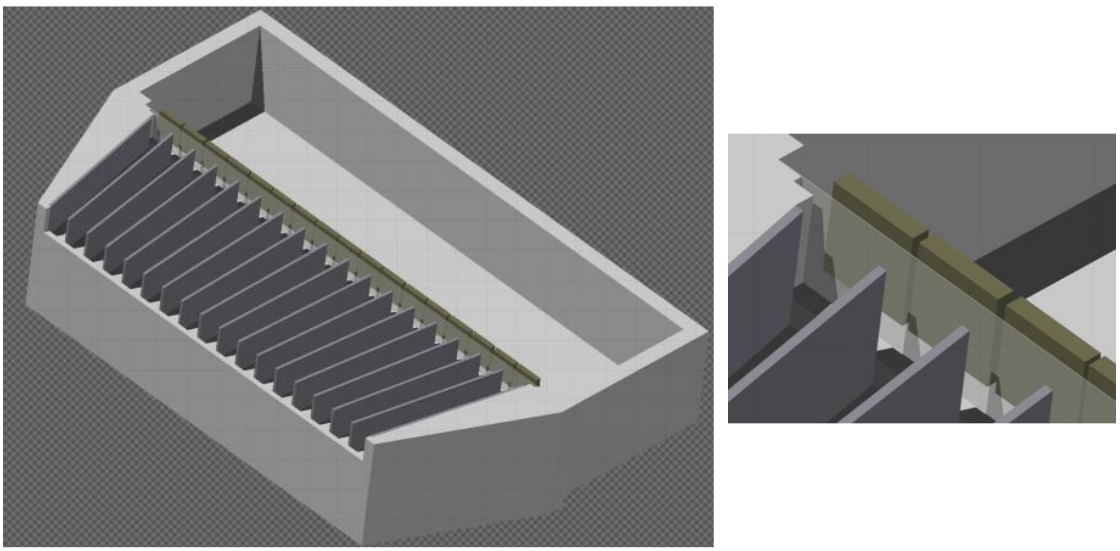

Figure 20. 3D plot of the detector module. A cut is made through the detector in the ZY-plane to expose the inner details. The figure to the left shows the full detector module, while the left figure shows a close-up. The middle collimators are not included, thus this figure only shows 18 collimators. *[34]*

In Figure 20 the 17 CdZnTe detectors have a dark green colour, the collimators have a dark grey shade and the housing is light grey. The 35-lead collimator

blades are situated in front of the detectors; their aim is to only allow transmitted photons passage, thus diminishing the effects of scattered radiation. The 35 collimators blades have a length of 60mm, height of 10mm and a thickness of 0.5 mm. As mentioned, they have an active area of 10×10 mm. Moreover, the spacing between the collimators blades are filled with silicone rubber to reduce the influence of microscopic noise that will occur in the areas in-between and around the detectors [34]. Figure 21 below has also been included since these plots give a very good visualization of the source module and its collimation and windows.

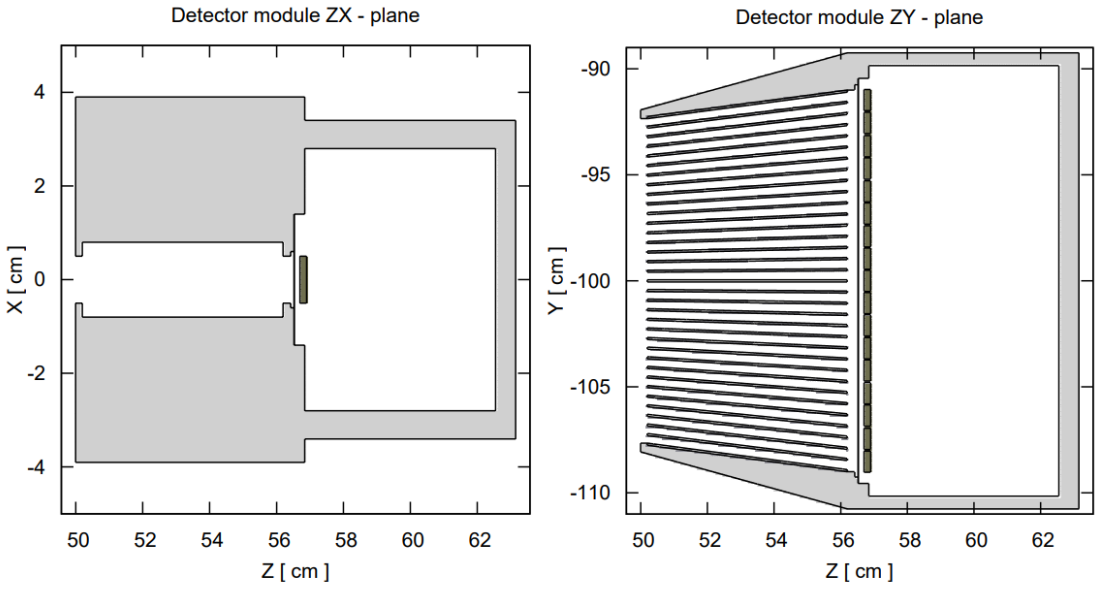

(a) *ZX plane.* **(b) *ZY plane.***

Figure 21. Cross section plots of the source module. In both source plots a cut has been made through the source module to expose the inner geometry. The detector modules are collimated in four steps. Firstly, an entrance window upstream of the collimator blades (10mm×153mm×2mm), as well as an entrance window downstream of the collimator blades (10mm×153mm×2mm). Furthermore, a thin stainless-steel sheet situated to the left for the detectors and an entrance window to the detector housing (28mm×191mm0.1mm). These plots are developed by Ketil Roed *[34]*.

In addition to the 35 collimator blades that are situated in front of the detectors, it can been seen from Figure 21 that the detector module is collimated by an additional four windows. The first two entrance windows are two lead windows; they are situated up -and downstream of the 35-collimator blades, this can be seen in figure a. Furthermore, the third collimation is a thin sheet of stainless steel that is situated after the downstream entrance windows and in front of the detectors, this can been seen in Figure 21 in both figure a and b. Lastly, a collimation window can be found in the entrance window to the detectors housing. The detector geometry that has been developed in MCNP consists of 17 detectors and 35 collimators per module. Thus, the 4-collimation windows in the housing and rubber between the detectors has not been included. Why this approximation

or simplification of source geometry is valid for this thesis project, will be further discussed and explained in Chapter 4.

3.4 Phantom - Measurement volume

The UiB GRT uses phantoms that consist of polypropylene and air to mimic a gas and oil flow, since they are similar in density. Crude oil and polypropylene have densities of ϱ=0.83g/cm^3 and ϱ=0.91g/cm^3, respectively. While air is a gas with a density of ϱ=0.001205 g/cm^3 at 15°C. Measurements on the UiB GRT can be conducted in a static or dynamic mode, where the latter indicates that the phantom is rotated to mimic flowing hydrocarbon flow. All experiments in this project will be conducted on a static system. Figure 22 shows an illustration of the different phantoms that will be used in the project. The [9].

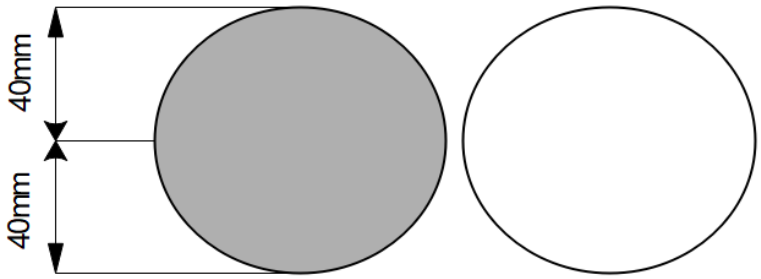

Figure 22. Phantom A (left) and phantom B (centre) which are used in the experiments, where white=air, grey= polypropylene.

Chapter 4

Modelling geometry setup

In this chapter, the geometry model that has been developed in MCNP6 will be discussed, as well a review of the most relevant parameters of the geometry setup. Firstly, an introduction to MCNP will be given, as well as a mention of Mortiz, which is the software that has been used for 3D visualization of the geometry. Visualization of the geometry makes it easier to detect errors in geometry definition. In addition, the inbuilt 2D geometry plotter in MCNP has also been used. Additional software tools that have been used in this project are briefly mentioned. MC simulation tools are vital, powerful and versatile tools that are widely used in physics for studying interaction of ionizing radiation with matter. This is due to the random nature of radioisotopes. As stated previously, radioactive decay is a stochastic process (random process). MC simulation are probabilistic models which means that each scenario has probability of occurring; hence, it forms a Poisson probability density distribution in the case of ionising radiation. MC tools can therefore be used to mimic or duplicate complex statistical processes, such as interactions of ionising radiation with matter [38] [35] [36].

The geometry model of the UiB GRT has been developed by reviewing previous works that have been conducted on the UiB GRT, among other works by Ilker Meric, Rachid Maad, Bjørn Tore Hjertaker and Geir Anton Johansen. In addition to a review of mechanical drawings of the UiB GRT. Implementing all the geometry from the UiB GRT to the simulation model is not necessary and is very time consuming. Thus, some geometry simplifications have been made, these will be addressed in the following sub chapters. Simplifications of the model are valid if the model shows good agreement with the real-life measurements, thus if benchmarking is successful. However, the model can be expanded with additional geometry in future projects. Previous model geometry of the UiB GRT has been used for guidance and as a starting point to learn MCNP. However, these geometry models where less complex and consisted of one source and one detector pentant with 17 collimator blades. Thus, alternations have been made. In Figure 15 the main dimension of the UiB GRT are presented.

4.1 Introduction to MCNP6.2

MCNP Version 6.2 is the simulation tool that has been used for executing the simulations that have been conducted in this thesis project; the developer of the code is Los Alamos National Laboratory [37]. MCNP is a 3-dimenisonal general-purpose Monte Carlo radiation transport code, which is designed to track particles over a broad range of energies. By general-purpose it is meant that it can be utilized to do numerous operations, which is also implied in the name MCNP. N particle refers to the fact that the software can simulate and track both photons, neutrons and electrons over a broad range of energies. For photons, this energy range is 1keV to 100keV. The code itself is ideal for simulating photons and neutrons, whereas electron interaction show more deviation compared to the real-life scenario. Due to the more complicated coulomb interactions, which can be small and many, thus hard to simulate. Relevant features that the code accounts for, for photons are: Coherent and incoherent scattering, secondary electrons, the possibility of fluorescent emission after photoelectric absorption and bremsstrahlung, thus it does not account for secondary ionization of nearby atoms [38] [37].

MC simulation consist of photons or particles that propagate through the detailed geometry that has been defined, during which several photons interact randomly (stochastic) with the geometry. The relevant physical interactions are photoelectric effect and Compton scattering, which all have individual probabilities of occurring, thus a Poisson probability distribution. In the MC method, random number generators are used to simulate the trajectory of each individual photon, which is analogous to throwing a dice in gambling casino – hence the name “Monte Carlo”. Random number generators are pseudorandom, hence deterministic since the random generator has a period or sequence of number it goes through. When the period is exceeded the same sequence of numbers will be run again but in a different order, resulting in new unique sequence of numbers. In each scenario, numbers are randomly sampled or generated from a density distribution to determine the fate of each photon. Hence, the trajectory of each photon from creation until death. Thus, the MC method mimics the behaviour of each photon individually and tracks their behaviour from the creation site in the source, throughout its lifetime to its death (absorption, escape, etc.). The tracks are sampled sequentially, and for each individual photon, this process from life until death is called a history. The history of a single photon may seem random, but as more histories are executed, the MCNP simulation model will start to resemble a real-life probability density function. More than

10^5 photons should at least be run for somewhat good statistics. Consequently, by developing a MC simulation model that mimics the real process, the model can be benchmarked towards the real process and utilized to acquire more data that normally would not be available. Benchmarking is the process of validating the simulation model and ensuring that model in fact describes the physical process within reasonable deviation from the true process [35] [37] [36]. MCNP has several libraries that contain e.g. cross section data and photon interaction data from 1eV to 100GeV, which are used in the simulations. Every photon that interacts in the geometry is scored, by scoring it is meant the parameters e.g. the 10 statistical checks that are developed in the output file, see chapter 4.1.3 Statics produced by MCNP for more information about the 10 statistical checks. The concept of how MCNP works is illustrated in Figure 23.

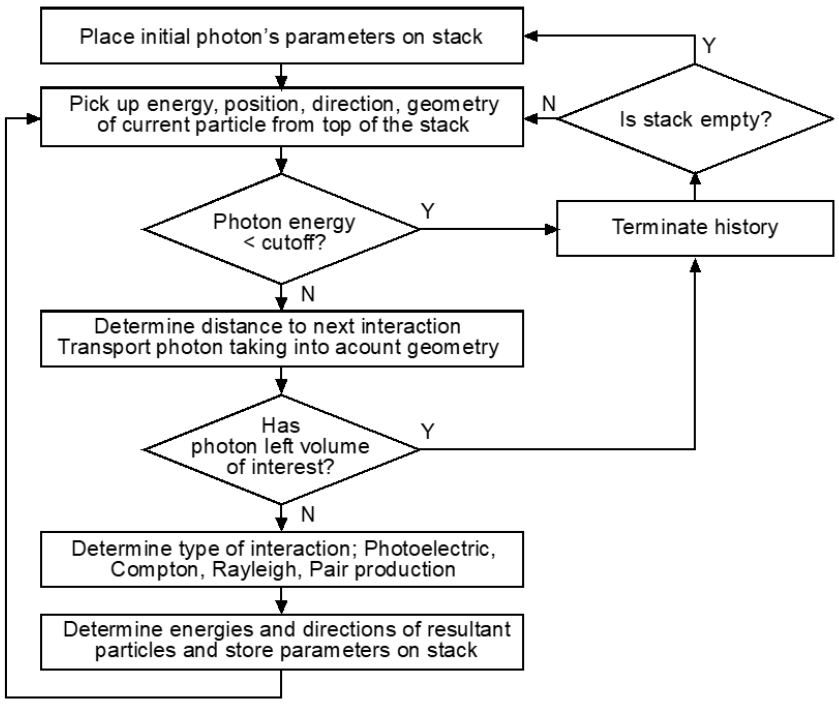

Figure 23. MC code concept that shows how photons are scored and how the MC process tries to mimic the random process, this is thus a pseudo-random process. (Source: PowerPoint MCNP5 introduction)

4.1.1 MCNP input file

To use MCNP6 an input file must first be developed with a set structure. The input file structure of MCNP is shown below in Figure 24.

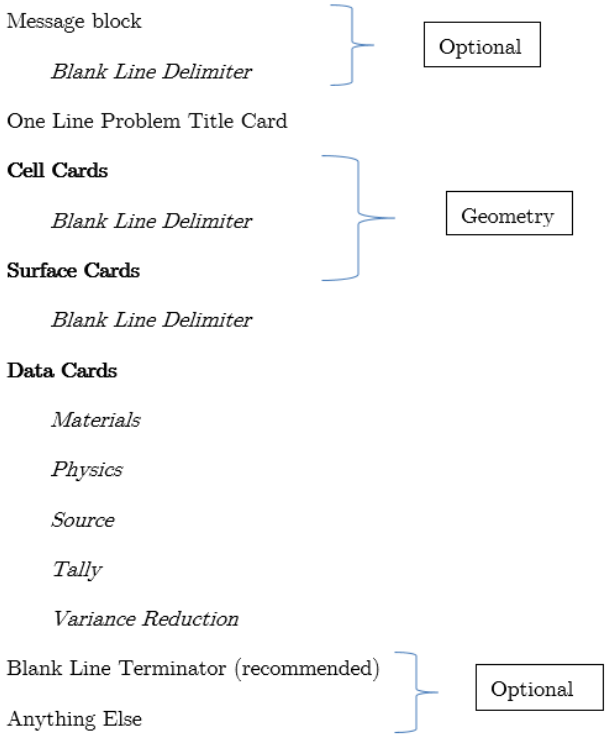

Figure 24. The structure of MCNP6 input files. Main sections are cell, surface -and data cards.

The input file in Figure 24 consists of three main sections that are cell, surface - and data cards. In the message block a title of the input file can be given. Surface cards are surfaces or 2D planes that are defined by the user. An example of surface definitions can be found below in Figure 25, which shows the surfaces 1-5 that have been defined in the MCNP geometry that has been developed in this project.

```
c  Problem surfaces
1  so  100.0  $ Inner/outer world
2  cy  4.065  $ Pipe inner radius boundary
3  cy  4.415  $ Pipe outer radius boundary
4  py  50.0   $ Pipe upper plane boundary
5  py -50.0   $ Pipe lower plane boundary
```

Figure 25. Surfaces 1-5 in the MCNP geometry that has been developed in this project. Further, the "c" indicates a comment, text or title.

Surfaces are defined with a specific structure where the first number is the surface number that uniquely identifies each surface. The second number is used for surface transformations; thus, surfaces can be set up in an auxiliary coordinate system that is related to the main coordinate system by a transformation. There are no surface transformations shown in Figure 25. However, there has been used

one surface transformation in total in the constructed geometry which can be found in Appendix A, further information about this topic can be found in the MCNP user manual. The last part of the surface definition is a mnemonic equation, thus some letters that describe the type of surface that is wanted. Which is followed by the location if it is a plane or its magnitude if it is a cylinder, etc. All surfaces pass through a point (x, y, 0) in reference to the origin. The origin of the developed MCNP model is defined as centre of pipe. In Figure 25, surface 1 is defined to enable definition of an inner -and outer world, which will be further elaborated on later in this section. Furthermore, surface 2 defines an infinitely long cylindrical surface which is parallel to the y-axis with a radius of 4.065 cm, thus the cylinder passes through the points (x=4.065 cm, y=4.065 cm, z=0). Note also the symbol $ denotes an in-line comment. Moreover, surface 3 defines an infinitely long cylindrical surface which is parallel to the y-axis with a radius of 4.415 cm. Lastly, surfaces 4 and 5 are planes that cut through y= 50cm and y= -50cm (x=0, z=0), thus they are parallel to the y-axis. These four surfaces 2-5 are used to define the pipe that is centred in the middle of the UiB GRT as shown in Figure 15, which is done by cell definition. Cell cards are volumes or 3D cells that are defined by intersections (space), unions (:) and complements (#) of regions that are defined based on the surfaces that have been defined in the surface section. The complements operator # (for NOT) is often a convention way of excluding an inner cell region, when e.g. want to define the material surrounding an inner cell with a different material. The definition of the measurements pipe volume can be seen below in the Figure 26 [37] [39] [40].

```
c Problem cells
c This file is a new verison of 42empi
1   0    1   imp:p=0  $ Outer world
2   0   -1   #3 #4 #444 #555 #666 #42 #43 #44 #45 #46 imp:p=1 $ Inner world
3   1   -1.38  2  -3 -4  5  imp:p=1 $ PVC pipe
```

Figure 26. Cells 1-3 in the MCNP geometry that has been developed in this project. Further, the "c" indicates a comment, text or title

Cells are defined with a specific structure where the first number is the cell number that uniquely identifies each cell. The second number is the material number, which corresponds to a specific material that has been specified in the material cards, which are found in the data card section. A zero is used in the material number section to specify a void; hence, the cell is a void consisting of nothing and is completely empty. Furthermore, the third number is the material density. If the material density is entered with a negative entry as in Figure 26, the mass density is in units of g/cm^3. Thus, for a void cell the material density is blank, as can be seen above in Figure 26. All the numbers that follow the material density section, are different surfaces that define the cell, thus these numbers

specify the geometry of the cell. As mentioned, cell 3 defines the pipe that is centred in the middle of the UIB GRT. Surface 3 is constructed with material number 1 (PVC), which has a density of -1.38g/cm^3. The cell consists of an intersection of the regions on the positive side of surface 2 (+2) and negative side of surface 3 (-3). As mentioned, surface 2 and 3 are both enclosed cylindrical surfaces, which can also be seen in Figure 25. For an enclosed surface a positive number in the cell definition card means that the cell that we want to define, is on the outside of this surface. While a negative surface means that the cell is on the inside of the enclosed surface. Thus, together the surfaces 2 and 3 form a pipe with a thickness that is the difference between surfaces 2 and 3. As, mentioned surfaces are infinite long. Thus, the plane surfaces -4 and 5 in Figure 26 gives the pipe (cell 3) a specific length, that goes from y= 50cm to y= - 50cm [39] [40].

One important property when designing the cell geometry is the cell importance card IMP:N. An importance is assigned to each cell in the geometry and specifies the relative importance of each cell, thus the cells that define the detectors should have a higher importance. How the IMP:N card is implemented in an input file can be seen in Figure 26. Furthermore, cell 1 and cell 2 define the outer and inner world of the model geometry. The outside world has in this problem been defined with an importance of zero to ensure particles are not tracked infinitely, this can be seen in Figure 26. Thus, MCNP terminates the particle's history if the particles reach the outer world or another region of importance equal to zero. From Figure 25 we can see that surface 1 is a sphere with a diameter of 100cm, thus the definition of cell 1 with a positive surface 1 indicates the cell we want to define is on the outside of surface 1, thus the outer world. The inner world has been defined with a -1, since the inner world is on the inside of surface 1. Furthermore, the complements # that are used in cell 2 are used so that inner cell regions of the inner world are not defined as void [37] [39] [40].

The last section in the input file is the data card section, which includes the source definition (sdef), material (m), tallies (f), problem cut-offs (number of particles = nps), energy -and thermal treatment (phys) cards. Thus, any other card except for cells and surfaces are included in the data card section. Tallies (f) are used to specify the desired information that is wanted in the simulation run, in this project the pulse-height or histogram tally f8 is used. Tally f8 counts the number of photons hits in a given energy range of interest, the units of the f8 tally is given as number of photons counts in a cell normalized to the total number of particle histories. Furthermore, the cut-off or number of particles (nps) defines the number of histories or particles that should be run before the simulation terminates. Moreover, epsilon –and zero bins have been used in the energy bins for the f8

tally that has been used in this simulation model. The epsilon bin (1.0e-5) catches scores from particles that have not interacted/deposited their energy in the detectors, thus these are lost particle. To find the total number of detected photons, the number of particles in the epsilon bin is subtracted from total number of histories. The zero bin catches none-analog knock in electron negative scores, which are secondary electrons with enough energy to travel far and cause secondary ionization. However, in this problem no electrons will have enough energy to do this. More information about input file definition can be found in the MCNP user manual. The MCNP output files contain the requested tally information and other requested information that has been specified in the input file.

4.1.2 MCNP output file

Once a problem is successfully run an output file will be generated. The output file is divided into several sections and starts with: (1) Input file listing followed by eventual errors. (2) Cells with their volume and mass, and a list of the cross-section libraries that have been used. (3) A summary of the run and how many particles that have been transported and the times it takes, as well as the number of particles lost. Followed by some more statics. (4) Followed by the tallies if they have been used. The tallies are marked with the energy bins that have been specified, and the number of particles detected in the bin normalised to number the total amount of starting particle/total number of histories. The relative error of each energy bin is also displayed. (5) Ten Statistical checks. (6) Tally fluctuations charts. Other standard tables are also printed, it is often convenient to turn some of them off by specifying which tables are wanted.

4.1.3 Statics produced by MCNP

One of the most important statics that MCNP produces are the 10 statistical checks, these must be studied. A brief review of these tests will be given, however more details can be found in MCNP user manual. The 10 statistical checks, checks each tally cell that has been specified, and statistical checks are run on the cells to ensure that each cell exhibit a certain statistical behaviour. Thus, the photons that hit a specific cell are analysed. As, mentioned the pulse distribution tally f8 has been used in the project which acts like a radiation detector and counts each pulse or particle that hits the detector cell, hence the behaviour in the cell is analysed. The simulation run should pass the 10 statistical checks, and if they are not passed one should question if the results are reliable. Regardless, one should

not blindly rely on these results, there may be other sources to why the simulation model does not show a wanted behaviour, this will be discussed later [39] [40].

Firstly, the 10 statistical checks display the mean for each tallied cell separately. The mean must exhibit only minor and random fluctuations for the last half of the problem, and only random behaviour as it increases in the start until the end. Thereafter, the relative error R is displayed for each tallied cell separately. For a well-behaved tally, the relative error R will be proportional to

$$R = \frac{1}{\sqrt{N}} \tag{5.1}$$

where N is the number of histories. If we want to half the relative error R, the total number of histories must be increased with a factor of four. Thus, increasing number of histories to reduce the relative error will result in an increased run-time for the simulation model. MCNP also produces confidence intervals for the tallies that are based on the estimated relative error. However, it is extremely important to be aware of the fact that the confidence estimates only refer to precision of the MCNP model, it says nothing about the accuracy of the results compared to the physical model. Further, they assume that all portions of the MC model are sampled well by the MC process. These estimates assume that all parts of the model have been sampled equally, which is often not the case. Thus, a benchmarking of the simulation model to experimental data will be conducted in chapter 6. However, the estimated relative error R should be presented with the mean in the MC results [35]. Guidelines for interpreting the relative errors in MCNP are given below in Table 1.

Table 1. Guidelines for interpreting Relative Error

Range of R	Quality of tally
>0.5	Meaningless
0.2 to 0.5	Factor of a few
0.1 to 0.2	Questionable
<0.10	Generally reliable
<0.05	Generally reliable for points detectors

Despite ones best effort, some important parts of the problem may not be sampled often enough, which causes the MCNP estimated confidence intervals to be

incorrect. To inform about this behaviour MCNP calculates the figure of merit (FOM) for each energy tally bin [35]. The FOM is defined as

$$\mathrm{FOM} = \frac{1}{R^2 T} \tag{5.2}$$

where T is computer runtime in minutes. An efficient and well-defined MC simulation has a larger FOM since this means less computer time is needed to reach the desired value of R. FOM must stay constant for the last half of the simulation run. Thereafter, the Variance of the variance (VOV) is presented, which tells us how accurately the relative error R of the mean has been estimated. VOV must decrease by 1/N for the last half of the problem and should always be less than 0.1 for all tallies. The last parameter in the 10 statistical checks is the pareto slope that examines the 201 largest scores/hits that occur, this parameter should be greater than 3. Below in Table 2 the 10 statistical checks table that was developed in a simulation are shown.

Table 2. The 10 Statistical checks that was developed when the model simulation was run for nps=2×10^9 histories, which resulted in a runtime of 3035.70 minutes. 468 indicated that tally f8 is run on detector module 46 (module 5). In this simulation run, only source 42 is open, and the statics show are based on the amount of radiation that is detected in detector 42 is recorded as a results of source 42. Source 42 and detector 42 are positioned directly "above" each other.

results of 10 statistical checks for the estimated answer for the tally fluctuation chart (tfc) bin of tally 428										
tfc bin behavior	--mean-- behavior	---------relative error--------- value	decrease	decrease rate	----variance of the variance---- value	decrease	decrease rate	--figure of merit-- value	behavior	-pdf- slope
desired	random	<0.10	yes	1/sqrt(nps)	<0.10	yes	1/nps	constant	random	>3.00
observed	random	0.00	yes	yes	0.00	yes	yes	constant	random	10.00
passed?	yes	yes	yes	yes	yes	yes	yes	yes	yes	yes

In the bottom of the output file, a tally fluctuation chart is developed by MCNP, which shows how the discussed parameters mean, tally error, FOM, VOV and slope behave as more histories are run. This is an important table and the parameters should behave in the manner as discussed above in this sub chapter. The fluctuation chart that was produced for the same simulation run as in Table 2 is shown below in Table 3.

Table 3. The fluctuation chart that was developed when the model simulation was run for nps=2×10^9 histories, which resulted in a runtime of 3035.70 minutes. 468 indicates that tally f8 is run on detector module 46 (module E). In this simulation run, only source 42 is open, and the statics that presented are based on the amount of radiation that is detected in detector 42 from source 42. Source 42 and detector 42 are positioned directly "above" each other. The parameters exhibit desired behaviour. The mean shows small and random variations, tally error decays with increasing nps and is constant in the last half (0.07%). FOM is large constant in the last half of the problem, VOV and slope are also good.

		tally 428			
nps	mean	error	vov	slope	fom
131072000	4.8974E-05	0.0028	0.0000	10.0	667
262144000	4.9041E-05	0.0020	0.0000	10.0	655
393216000	4.9120E-05	0.0016	0.0000	10.0	653
524288000	4.9128E-05	0.0014	0.0000	10.0	652
655360000	4.9069E-05	0.0012	0.0000	10.0	650
786432000	4.9107E-05	0.0011	0.0000	10.0	650
917504000	4.9091E-05	0.0011	0.0000	10.0	649
1048576000	4.9101E-05	0.0010	0.0000	10.0	649
1179648000	4.9073E-05	0.0009	0.0000	10.0	648
1310720000	4.9049E-05	0.0009	0.0000	10.0	648
1441792000	4.9062E-05	0.0008	0.0000	10.0	648
1572864000	4.9066E-05	0.0008	0.0000	10.0	647
1703936000	4.9072E-05	0.0008	0.0000	10.0	647
1835008000	4.9077E-05	0.0007	0.0000	10.0	647
1966080000	4.9082E-05	0.0007	0.0000	10.0	647
2000000000	4.9081E-05	0.0007	0.0000	10.0	647

If the test 10 statistical do not pass, a message will be developed and printed in the output file. The 10 statistical test and fluctuation chart provides an excellent indication to whether the simulation results are reliable, but they are not failproof. Some high-scoring rare event may not have been sampled. Thus, several runs should be run to show repeatability as well as study and insight to avoid traps. Furthermore, to obtain meaningful results from simulation runs, in most cases, a minimum of around 10^6 histories must be performed, which means that large utilization and computation power is needed [40].

4.1.4 Accuracy VS precision

Several variance reduction methods are available in MCNP, which can be used to improve the statistical results that are developed by a MCNP simulation model. One important remark is that using these variance methods may lead to very good MCNP statistics, however in most cases the use of many will result in big deviation between the simulation model and the true physics or model, which in this case is the UiB GRT. For this reason, the difference between accuracy and

precision will be elaborated on is presented below in Figure 27, this are important concepts for benchmarking of the MCNP model.

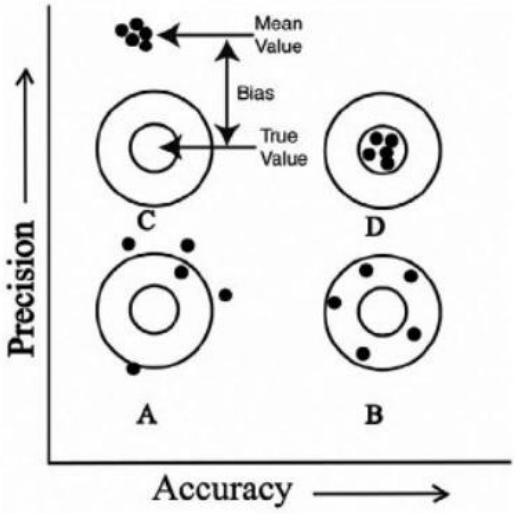

Figure 27. Graphical illustration of the relationship between accuracy, precision (repeatability) and bias (statistical error). A) Demonstrates a low accuracy and low precision; thus, a random behaviour, the method or model is therefore useless. B) Illustrates high accuracy but low precision since the dots are scattered. C) Shows high precision since there is little scatter, with poor accuracy since there exhibited a large bias (systematic error), which much must be corrected for. D) Shows an accurate and precise model or method. (Reprint from McCalden et al. J Bone Joint Surg Am 87:2323-2334, 2005) *[41]*.

Technically, uncertainty is precision, thus estimated relative error for the mean is a measure of how precise the MCNP model is. Moreover, the accuracy of the MCNP model is the measure of how close the simulation model is to the true conditions in UiB GRT. Factors that may affect the accuracy of the MCNP simulation model may be inaccuracies in MCNP itself, in the (1) physical models, (2) mathematical models, (3) uncertainties in nuclear/atomic data and cross section. However, MCNP is a mature code, thus these sources of errors are generally of no concern, thus neglected since these inaccuracies lead to a total uncertainty of 1%, which is negligible. Furthermore, inaccuracies in the MCNP model which may be due to, (1) improper modelling of source energy and angular distribution. Poor representation of the actual geometry in MCNP, the simulation model can never be more accurate than the geometry definition. Errors in material composition. Another source to inaccuracies in MCNP is human errors, which is often the most important and biggest source (1) incorrectly use of program use or making errors in the input file. Similarly, a novice often misunderstands which tally should be selected for the specific information that is wanted [40].

Factors that may affect the precision of the MCNP simulation may be (1) the choice of tally effects the precision considerable. E.g. a point detector is often less

precise than a surface detector in a medium where scatter occurs. (2) The use of different variance techniques may affect the precision tremendously. (3) Number of histories since increased nps lead to better tally precision, consequently a larger computer run-time is required to achieve the desired relative error [40].

4.2 Software tools

A brief review of some relevant software tools that have been used in this project.

4.2.1 Mortiz

Mortiz is a geometry editor that is designed to speed up the construction of the MCNP and other geometry models. Thus, in this project Mortiz has been used for 2D and 3D visualization of the MCNP geometry that has been developed in this project. By visualizing, the geometry errors in the geometry definition are easier and more quickly found and correcting measures may be made to the MNCP input files [42].

4.2.2 LabVIEW

LabVIEW is a data acquisition and hardware control system software that uses graphical programming of the system; hence it allows visualization of the system. In this project LabVIEW is interface between the UIB GRT and the PC, thus it permits communication between them. Thus, in this project LABVIEW is used to collect sampled data from the experiments that have been conducted on the UiB GRT [43].

4.2.3 MATLAB

MATLAB is a programming platform that can be used to solve a vast area of problems. In this project MATLAB is used for data handling, computation and plotting of the measured data from the UiB GRT and MCNP simulation output files. A script that reads the output files from MCNP has been developed in MATLAB, as well as script for reading and plotting the experimental data [44].

4.2.4 Xming

Xming is a program that runs a X windows system server that allows graphical user interface software that has been developed in LINUX/UNIX computers to be displayed on Windows computer. To use the inbuilt 2D geometry plotter or viewer in MCNP, Xming must be installed beforehand. Before opening MCNP on the computer Xming must be activated by double clicking on desktop icon. To plot 2D geometry with MCNP the command *"mcnp6 ip n=file + ENTER"* is typed into the command window in MCNP [45]. The function ip checks for errors in the geometry and then starts the geometry plotter [39]. Hence, in this project Xming has been used to enable graphical 2D visualisation in MCNP.

4.3 Geometry model developed in MCNP

The model geometry has been developed in MCNP version 6. Furthermore, visualization of model is done with Moritz, and the inbuilt 2D geometry plotter in MCNP. MCNP uses the following workflow as shown below Figure 28.

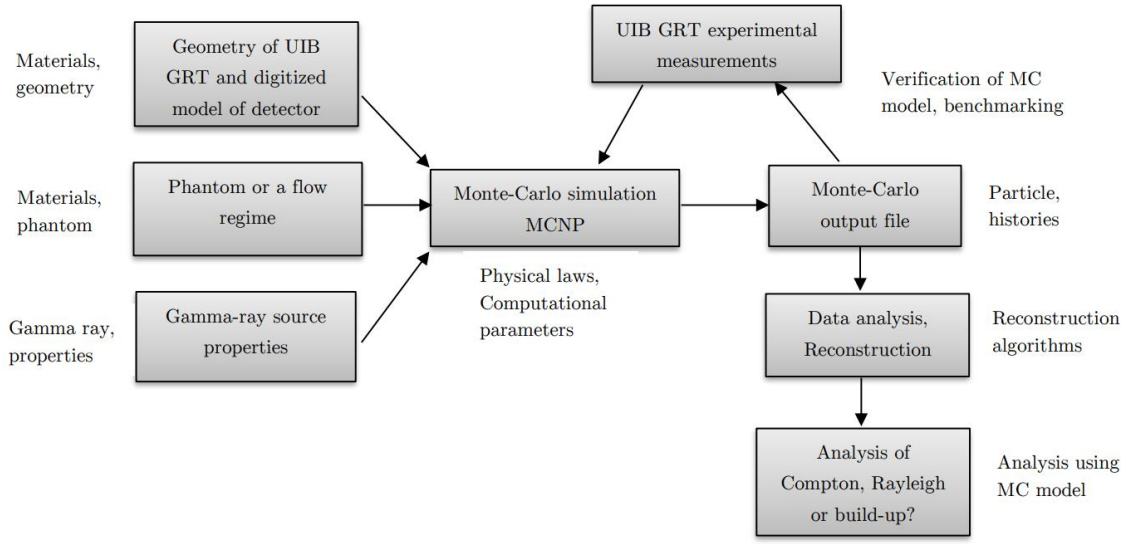

Figure 28. Workflow that shows how an MCNP simulation if developed. Note: digitized detector=f8tally.

4.3.1 Model geometry

Figure 29 shows the geometry that has been developed of the UiB GRT, the visualization is done with Mortiz. Some simplifications have been made in the defined model geometry, e.g. the source -and detector housing is not included, and source definition. While the geometry of the collimator blades and detectors are more accurately implemented. The measurement pipe has a turquoise colour in Figure 29 and has been defined with an inner -and outer diameter of 80.10mm and 88.80mm, respectively. The orange cell inside the measurement pipe is the phantom. These initial pipe dimensions have been chosen since they have been used in a previous MCNP simulation with one detector module and one source module. Thus, this indicates that the dimensions that are needed for benchmarking the model to experimental data is somewhere in this dimension range, thus a good starting point. The five “pink boxes” that surround the measurements pipe are the five detector pentants; these are orientated around a pipe with a circumference of 44cm, thus an angle of 77° between them. In Mortiz

the different colours indicate different cells in the geometry. The different multi-coloured lines on the "pink boxes" are the collimators blades. As mentioned previously, each detector module consists of 35 collimator, which each have a length of 60mm and a thickness of 0.5mm. Furthermore, the multi-coloured squares that are located in front of the "pink boxes" are the 17 CdZnTe semiconductor detectors that are present in each detector module.

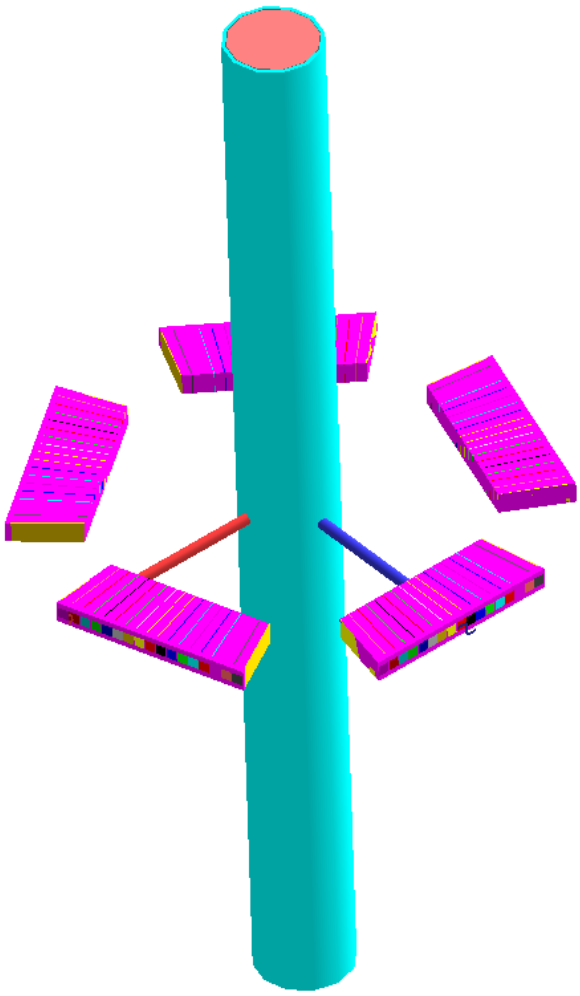

Figure 29. 3D visualization in Moritz of the developed UiB GRT. The broad red line that intersect the pipe is the x-axis and broad blue line z-axis. The blue z-axis passes through detector module 42.

The sources have been implemented as mono energetic disk sources (59.5keV) with a radius of 1cm. Only one source can be defined in an input, thus five separate input files with corresponding source positions have been developed. The sources are orientated around a pipe with a circumference of 44cm, thus an angle of 77° between them. Such simplifications of source geometry may cause a big deviation from true conditions, e.g. since the photons will interact in the source

housing and give a distinct source distribution. However, since the UiB GRT detectors do not have energy resolution, the exact energy distribution cannot be found and simplifications have been made. Figure 30 below shows a 2D visualization of the geometry in Mortiz. The different lines in this Figure 30 are the different planes that have been defined. As stated previous, all planes that are defined in MCNP have an infinite length, hence cells are made by intersections of planes, as seen in Figure 30. Furthermore, the lines that pass through the focal points are used for definition of the collimator blades. Moreover, the different numbers in the Figure 30 are surface numbers. The numbers are only labelled in one detector pentant since this is the original detector 42, the other have been defined using coordinate transformations.

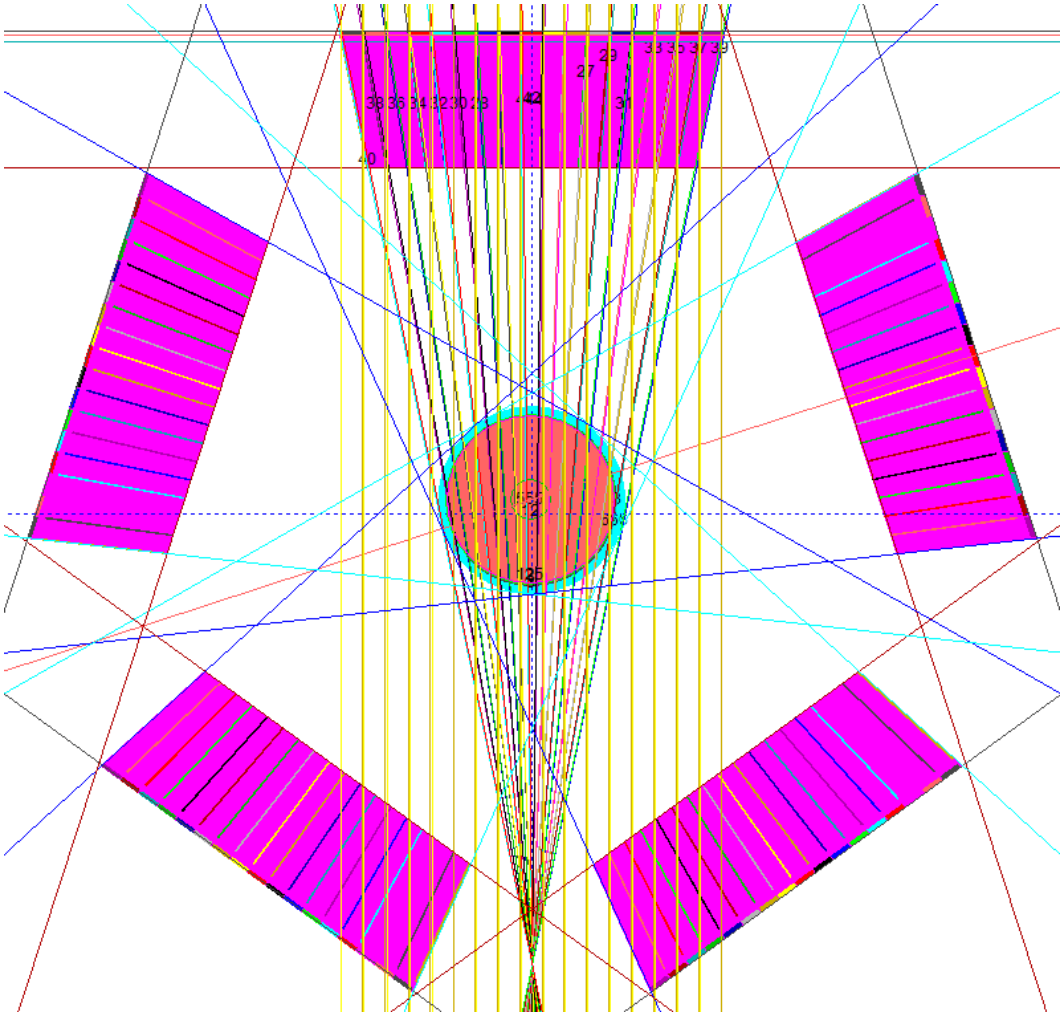

Figure 30. 2D visualization in Mortiz of the UiB GRT geometry in the zx-plane. The lines that pass through the focal point in the center are used for defining the collimator blades.

4.3.2 Material

After defining the geometry, the materials of the different cells must be defined. The inbuilt 2D plotter in MCNP differentiates materials in the geometry with different colours. Thus, Figure 31 shows a labelled 2D illustration that has been developed with the inbuilt MCNP plotter. The definition of the labelling and associated materials can be found in Table 4.

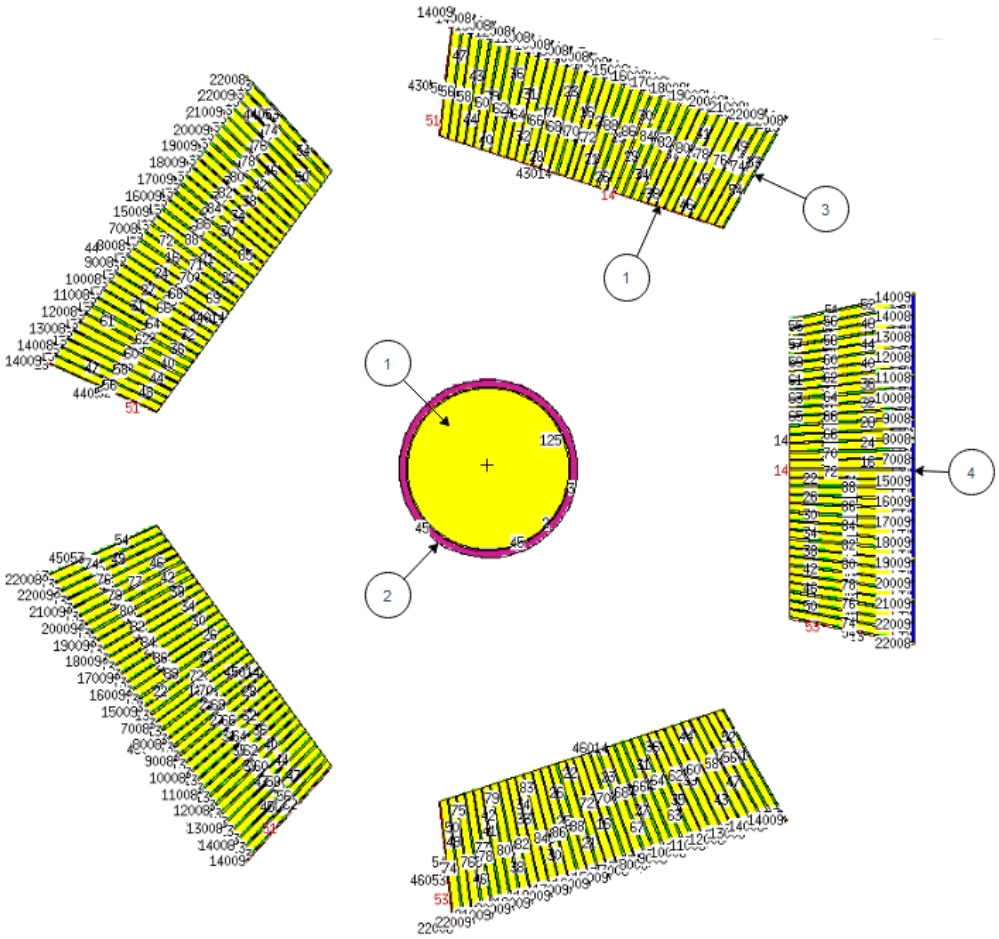

Figure 31. 2D visualization of the UiB GRT model with the inbuilt 2D plotter in MCNP, the plot shows the zx-plane. The detector module on the far right side is detector module 42 (1), the other modules are labelled anti-clockwise from module 42 with the number 43-46. In module 42 the blue detectors are visible; they are not visible in the reaming detectors. When transformations are used for defining repeatable geometry MCNP itself defines new planes with longer names, thus this new long names block the viewing of the blue detectors in modules 43-46.

From Table 4 and Figure 31 we observe that air (yellow) has been defined as the material inside the pipe, as well as the material that is between the collimators (green). As mentioned previously, the phantoms that are used in this project consist of air or polypropylene, thus in experimental -and simulation runs the

content of the measurement volume will be altered depending on the desired output.

Table 4. Material definition of the geometry model

Number and colour	Material	Density range [g/cm3]	Description
1 Yellow	Air	0.001205	At 15°C (Phantom material 1)
	Polypropylene (PP)	0.85-0.92	Phantom material 2
2 Pink	Polyvinyl Chloride (PVC C2H3C1)	1.3-1.45	Pipe-wall (Rigid PVC, synthetic plastic)
3 Green	Lead	11.34-11-35	Collimator blades
4 Blue	CdZnTe	5.75-5.85	Detectors

For further visualization, Figure 32 has been included, which shows the inner geometry of the measurement pipe.

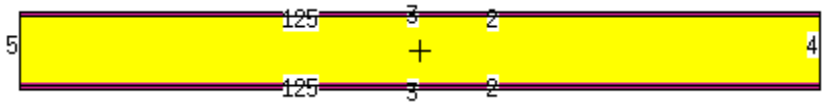

Figure 32. Inner pipe geometry cut through yz-plane. The pipe is defined with a total length of 100cm

Chapter 5

Results from MCNP simulation model and experiments

To ensure that the developed MCNP simulation model gives an adequate and accurate description of the UiB GRT, the simulation model has been benchmarked. Benchmarking is the process of validating the simulation model and ensuring that model in fact describes the physical process within reasonable deviation from the true process. This must be done before the simulation is used to gather additional information and data of interest, e.g. finding the amount of Compton -or build-up scatter that is present in the detectors. It is therefore very important to define the input file as accurate as possible, since the accuracy of the output data from the simulation will never be more accurate than the input definition [35]. The benchmarking has been executed by running the same experiments experimentally with the UiB GRT and theoretically by setting up the same scenario in MCNP. Benchmarking of the model has been conducted by comparing full pipe with 100% polypropylene (PP) relative to empty pipe (100% air) for measurements and for simulation results. Chi-square value test is used for quantifying the comparisons. The best model has been found by comparing the chi-square value of different fine-tuning approaches will be evaluated in this chapter. The following phantoms that are shown in Figure 33 have been used for benchmarking the MCNP simulation model to experimental data. After finalized benchmarking process the optimal model containing the parameters that minimize the chi-sum have been used to quantify the amount of Compton scattering from each of the sources UiB GRT. Lastly, the amount of Compton scattering that is present under normal operating conditions of the UiB GRT has been quantified.

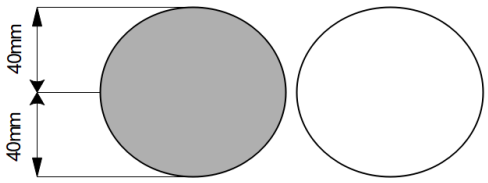

Figure 33. Phantom A (left) and phantom B (centre) which are used in the experiments, where white=air, grey=polypropylene.

5.1 Experimental measurements

The experiments have been conducted on the UiB GRT with assistance from Rachid Maad. The meter is situated in the radiation laboratory, in the Department of Physics and Technology at The University of Bergen. Before starting the experimental work, radiation safety was ensured by using dosimeters ordered from safety authorities of Norway and a radiation-meter to locate high-dose areas. The UiB GRT displays number of photons detected in predetermined integration time, thus is displays number of photons per second(s).

5.1.1 Radiation protection

Radiation protection is important; to ensure a safe working environment a dosimeter and gamma meter (µSv/hour) was used to keep track of radiation levels. Areas of higher radiation where identified to ensure a safe working distance from these areas. The higher radiation areas where identified to be in the area in front the pipe, since the sources are directed inwards toward the pipe some radiation will be scattered outward in the open-ended pipe. The radiation sources are shielded but should not be touched; hands should not enter inside pipe both when sources are open and closed. It was measured a rate of 0,250±0,020 µSv/hours at a distance of 1 meter from the UiB GRT when all the sources where open, which is in the range of background radiation in Norway ≈0,200 µSv/hours. Table 5 presents measured radiation levels at different distances from the UiB GRT, keeping a distance of 1meter from UiB GRT ensures radiation safety. In summary, the most important aspects of radiation protection is time, distance and shielding. When working with radiation it is important to minimize the time spent near the source, always ensure that the work is conducted at a safe distance from source and position yourself behind the source shielding [46].

Table 5. Measured Radiation in the area of UIB GRT

Distance from UIB GRT	Measured Radiation
≈1m	0,240±0,020 µSv/hours
≈0,5m	0,465±0,020 µSv/hours
≈[2]0m	0,850±0,020 µSv/hours

[2] Measured when the radiation counter was placed on top of the source shielding while the source was open

5.1.2 Acquisition experimental data

All experiments have been conducted on a static system, since this gives a clearer and more obvious counting response pattern from the UIB GRT. When comparing experimental data to simulated data it is important, that both data sets have the same uncertainty or quality. Consequently, the integration time of all experimental runs has been set to 20 seconds since this gives the same uncertainty range as the MCNP simulations. In MCNP, the relative error must be less or equal to 0.10 to pass the statistical test. An integration time of 20 seconds in UiB GRT results in counts rates above ≈300 000 photons for all detectors when all sources are open, for both full pipe with 100% PP and empty pipe with 100% air. By using Equation (2.3), we find that the standard deviation of 300 000 photons is equal to

$$\sigma = \sqrt{300\,000} = \pm 547.70 \text{ photons}$$

From this, we can calculate the corresponding relative uncertainty, which is

$$\frac{547.70}{300000} = 0.0018$$

As seen from the calculations above an integration time of 20 seconds gives a relative uncertainty of 0.0018, which is in the same uncertainty range as the MCNP model, which has a relative uncertainty of 0.001. Thus, the experimental measurements and simulation model are in the same uncertainty range. Hence, to minimize the statistical uncertainty an integration time of 20 seconds is selected. As stated in chapter 3, the detectors in UiB GRT counts the number of photons detected in the given integrations. Hence, every 20 seconds the number of detected photon counts are displayed on the computer screen. Thus, output units from the UIB GRT in these experiments will be number of photons counts per 20 sec (counts/20s). When the UiB GRT was turned on there was observed a fluctuation in photon counts per second/seconds (cps), thus a stabilization time of 10-15 seconds was needed to reach system stability, where only minor and random fluctuations are seen in photons counts. The experiments where run according to the plan that is given in Table 6; the following data was collected and stored to a LabVIEW file. The dataset in Table 6 was collected twice at different times and given the names A and B, respectively. The threshold in the detector modules are set to 48keV, thus only photons with energies above or equal to the threshold will be detected. Each logged run gives 85 data points that show cps in each of the 85 detectors, where each data points corresponds to number of counts per

detector. Data points 1-17 correspond to detector module A (42), 18-3 4module D (43), 35-51 module C (43), 52.68 module D (43) and 69-85 module E (43).

Table 6. Detailed plan for the experimental data collection from the UIB GRT, this data will be used for benchmarking the simulation model that has been setup in MCNP6.2-EXE

	Sample	Sources
1	Empty pipe (100% air)	All open
2	Full pipe (100% PP)	All open
3	Empty pipe	Only source A (42)open
4	Empty pipe	Only source B (43)open
5	Empty pipe	Only source C (44)open
6	Empty pipe	Only source D (45)open
7	Empty pipe	Only source E (46)open
8	Full pipe	Only source A (46)open
9	Full pipe	Only source B (46)open
10	Full pipe	Only source C (46)open
12	Full pipe	Only source D (46)open
13	Full pipe	Only source E (46)open
14	Empty pipe (100% air)	All open (1 month later)

The acquired experimental data confirmed that four of the detectors are out of order; they appeared with the value zero in the data sheets. This result was expected since it has been discovered previously. This problem was corrected for by interpolation between the two neighbouring values, thus the number of counts placed above and under the zero. Figure 34 below shows the counting response from the UiB GRT for empty pipe with 100% and full pipe with 100% PP.

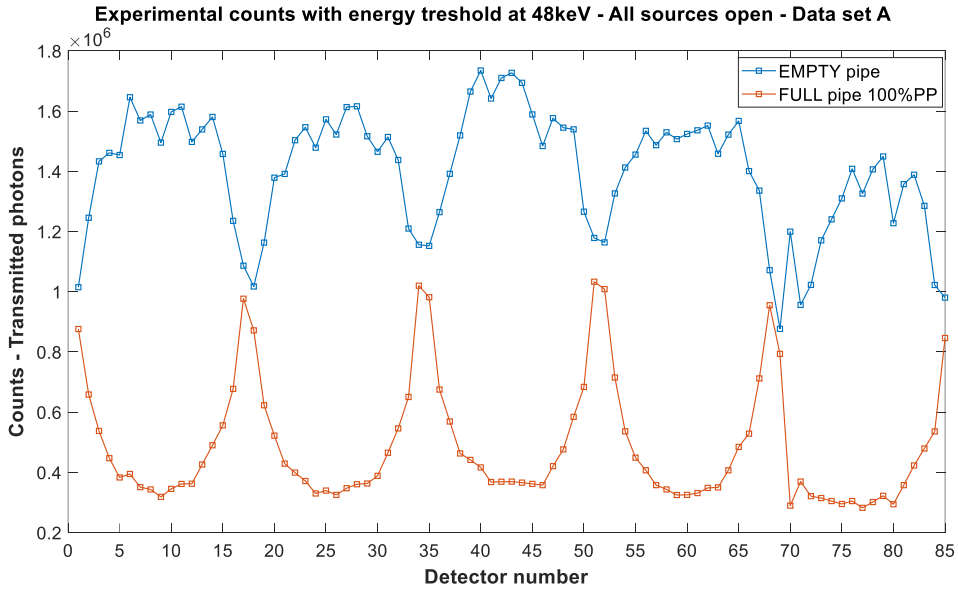

Figure 34. Counting response from UiB GRT. Blue graph is empty pipe counting repose and red is full pipe system counting response.

As expected, the number of detected counts in each individual detector is larger for empty pipe compared to full pipe, which is due to more attenuation of the beam when the photons travel through a material with a higher Z number and density, see Figure 34. As discussed previously, probability of attenuation increases with increasing Z number. For empty pipe, more counts are detected in the middle detectors, which is expected since the beam is directed towards the centre detectors. When we move to the outer detectors for empty pipe, fewer counts are detected since the beam is as mentioned centred at the middle detectors. Furthermore, the outer photons travel through more dense material since they travel through more of the pipe-wall compared to the more centred photons, thus probability for attenuation or scatter is more probable at the outer regions. For full pipe (100% PP) less photons are detected in the middle detectors, since these transmitted photons have to travel a farther distance in dense phantom, compared to the outer photons. Consequently, the probability for attenuation is higher for these transmitted photons since they travel farther in the phantom. Furthermore, in Figure 34 we can also observe the effect of pile-up, which causes the rough, uneven and fluctuating behaviour that can be seen for empty pipe, which leads to an additional associated uncertainty in the data. Pile-up occurs for high-count rates when the detector electronics have too low temporal resolution and are not able to distinguish between the different hits/pulses. The hits/pulses are so close in time that the detectors are not able to distinguish between them and registers several hits as one, which result in an overshoot/peak. The same pile-up behaviour has also been observed in the report by K.Roed [34]. Some fluctuations between neighbouring detectors are observed in full pipe; however, it is not dominant, and this behaviour may also be due to attenuation or scattering events, not necessarily pile-up. From Figure 34 we also observe that there are fewer detected counts in detectors module 45(D) and 46(E), which assumed to be due to source decay. Sources decay with time, which means that the source intensity declines, thus lowering the threshold for modules 45(D) and 46(E) may possibly improve their system counting response. However, a similar system counting response is observed for all modules for full pipe, thus lowering the threshold might not help modules 45(D) and 46(E). Detector module 46(E) exhibits a very different behaviour from the rest, which is may be due to aging of the semiconductor material. Detectors have a lifetime where they work optimal, after a time the semiconducting materials in the detectors will have a change in properties due to aging, thus they will behave different. Thus, the benchmarking process of the developed model to the experimental data will be focused around detectors 42-45 (A-D), since detector 46(E) suffers from aging. In Figure 35 data set A has been presented with error bars that have been calculated with

Equation(2.3), which finds the standard deviation by taking the square root of number of particles or histories.

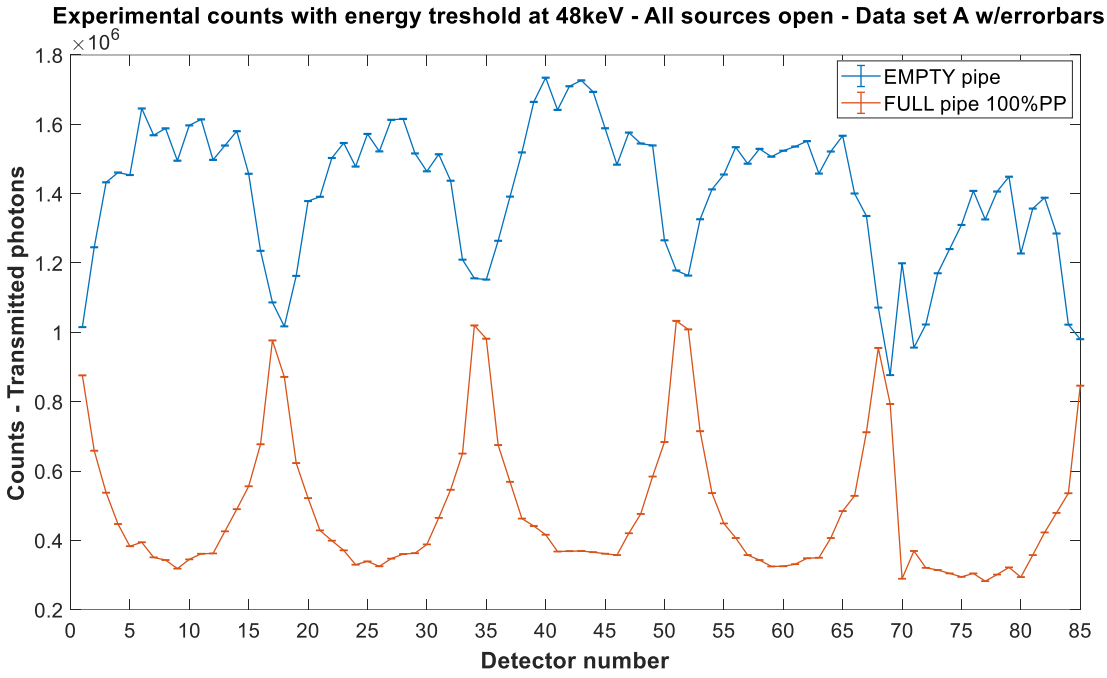

Figure 35. Counting response from UiB GRT with error bars that have been calculated from square root of number of particles, as defined in Equation (2.3). Blue graph is empty pipe system counting repose and red is full pipe system counting response.

From Figure 35 we observe that number of counts is so large that the uncertainty contributions from the square root of counts becomes negligible. Thus, it is assumed that main uncertainty or error contributor in the data sets is the uneven and rough behaviour that is prominent for empty pipe due to pile-up. In Figure 36 the normalized intensity contribution from each detector module has been plotted. Thus, each detector has been normalized to the highest number counts in the data array. From Figure 36 the relative uncertainty is evaluated to be equal to be ± 0.03 or 3% for the 17 detectors in each module, with a confidence interval of 95% (1 of the 17 data points is outside of range ± 0.03). However, detector module 46 (E) exhibits a differing behaviour as mentioned previously, therefore the benchmarking of the simulated model to the true experimental model will be focused around modules 42-45 (A-D) Furthermore, the fluctuation for empty pipe leads to an increased uncertainty for full pipe, since full pipe measurements are normalized by the max intensity for empty pipe. This uneven behaviour will be taken into account by using moving mean for each individual detector. Moreover, in some cases this behaviour will be accounted for by taking the mean of the four or five highest count contribution in each detector module. This done so that to enable comparison between different data sets.

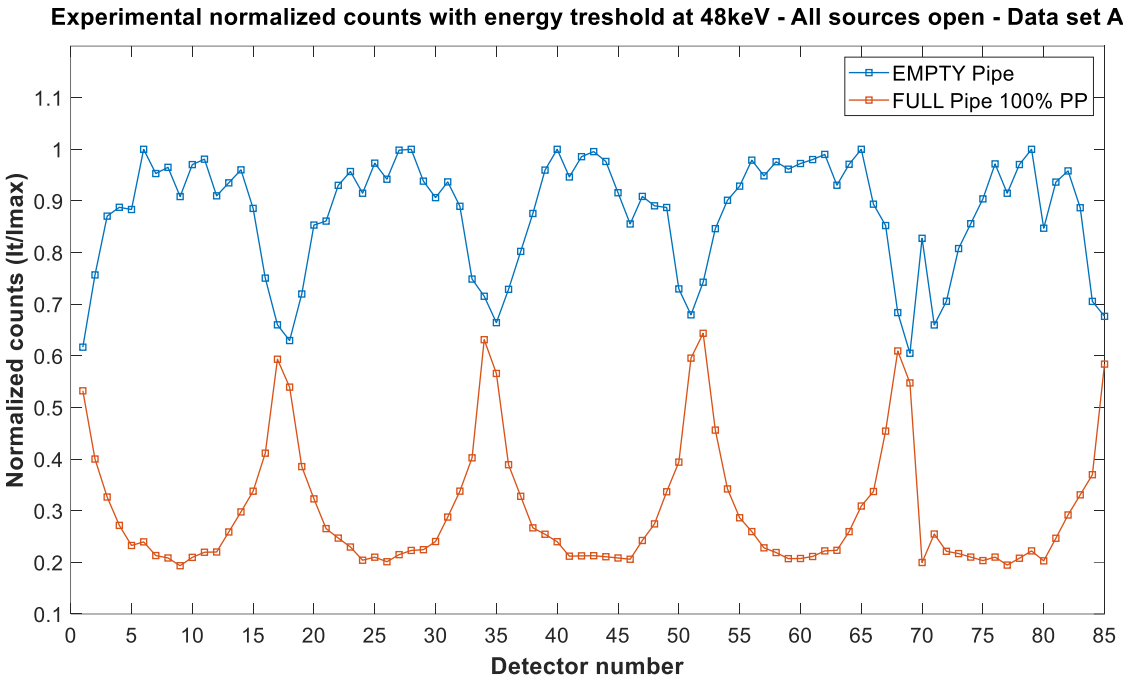

Figure 36. Normalized experimental data for empty and full pipe. Each detector module has been normalized to the highest number of counts in the respective detector module.

5.1.3 Analytic comparison data set A and B

Two separate data sets A and B where collected from the UiB GRT according to the detailed plan in Table 6; a comparison is presented below in Figure 37.

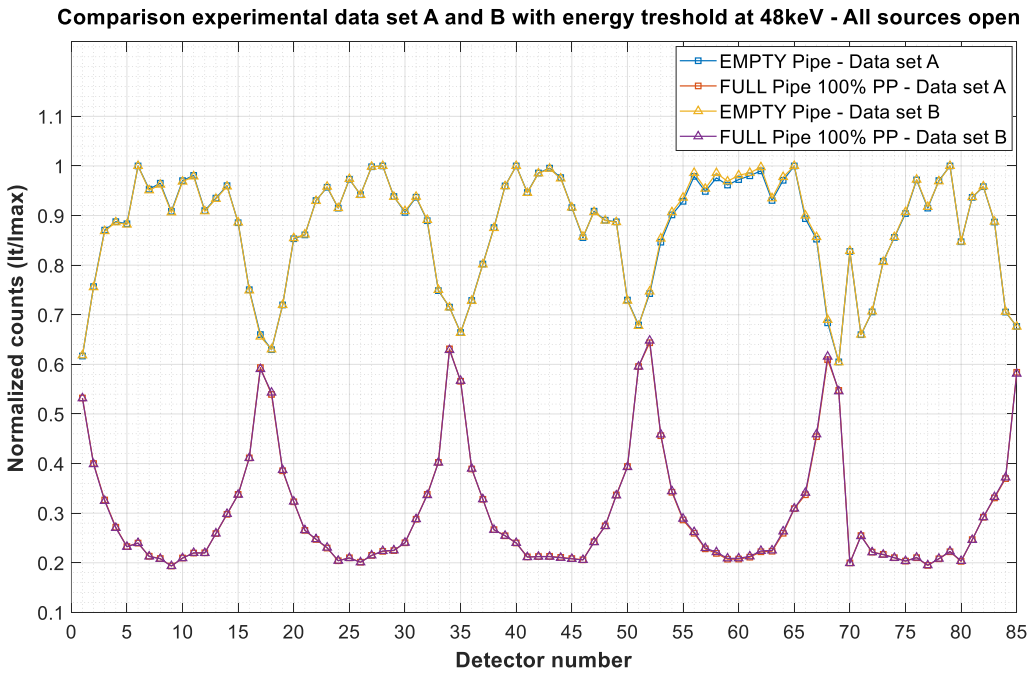

Figure 37. Full and empty pipe data from data sets A and B plotted.

To ensure repeatability of the experimental behaviour in the data from the UiB GRT, two different sets of data A and B where collected at different times. It was especially interesting to study whether the observed fluctuating behaviour that empty pipe has exhibited, repeated itself and to see if there is any drift or change in source activity. Repeatability is the ability of an element to give the same output for the same input, when the same scenario or measuring setup is repeated. Lack of repeatability if due to random effects or fluctuations in the elements or its environment [47]. As mentioned, drift, is a reduction in source activity, since the source activity declines with time, thus the data sets A and B have been collected 2 months apart. Figure 37 shows the data from empty and full pipe from the data sets A and B, the register detector module counts have been normalized to the highest number counts in the data array for empty pipe. From Figure 37 we observe a very good agreement between the two data sets, thus the UiB GRT exhibits repeatability, only minor negligible bias can be seen in detector module 45 (D). Thus, repeatability is assumed for the UiB GRT system.

5.2 MCNP simulation model setup

The developed MCNP model consists of 10 individual input files, thus 10 individual simulation jobs must be run to model the whole UiB GRT MCNP model. This is due to the fact that an input file only can contain one mono-energetic source. Consequently, each of the five ^{241}Am sources have their own location, which has been defined in respective input files. Furthermore, the UiB GRT must always be calibrated to empty and full pipe. By detecting number of photons counts for empty and full pipe we get a maximum and minimums, thus all other with varying phantoms must lie on or between these two extremes. Ten individual input files have been developed to enable simulation of all five sources for both full and empty pipe. The initial random number generator seed is by default set to 19073486328125 for the first particle history run; this is the starting point for the generation of random numbers. The seed is restricted by the condition that is must end with an odd digit [37]. To avoid a strong correlation between the sources 42-46 each of the sources are given a unique initial seed. The unique seed that corresponds to a specific source will be the same for different simulation runs. Firstly, since the sources have identical source distribution and secondly to uphold repeatability, which is crucial since this allows comparison between similar experiments runs [48]. The number generator was set to GEN=4,

which is the longest period of 9.2×10^{18} numbers which means that the period will most likely never be repeated in one simulation run. To pass all of the ten statistical tests for the developed model 2×10^{9} histories must be simulated which gives a run time of 50 hours per input files. The simulation computer that has been used has four cores and is able to simulate three files parallelized, thus simulating all 10 jobs takes ≈200 hours. Thus, for benchmarking purposes a total of 10^{8} histories where run. This is done to keep the total simulation time needed manageable, since several different jobs must be run to find optimal model parameters. Secondly, since the energy range of interest is not in the tail of energy distribution. When running 10^{8} histories all statistical test passed expect for FOM. This is due to the varying bin sizes that have been defined in the input files, which cause a varying sampling density in the defined bin sizes. A simulation with 10^{9} for the model shown below in Figure 38, where the energy bins can be observed

```
cell (16<42)
     energy
   0.0000E+00   0.00000E+00 0.0000
   1.0000E-05   1.93500E-07 0.0114
   1.0000E-03   1.55000E-09 0.1270
   4.8000E-02   5.42263E-06 0.0021
   5.9600E-02   6.67408E-05 0.0006
     total      7.23585E-05 0.0006
```

Figure 38. 2 Tally f8 simulations with 2×10^{9} particles. Left column are the energy bins in MeV, middle column shows number of detected particles in the respective bin and the column to the left shows relative error in respective bins.

In *Figure 38* the row to the left are the different energy bins, which are given in units of MeV. These energy bins correspond to the upper bin energy, thus e.g. 5.96KeV corresponds to the energy range 4.8-5.96keV. The middle column shows the total number of particles detected in the respective bin, which has been normalized to total number of particles. Furthermore, the column on the right side shows relative errors in the respective bin bins. The different bin sizes cause different sampling density in the bins, thus the bins which are sampled less contribute to the FOM test not passing. Furthermore, since the high relative uncertainties occur when few particles are simulated. In Figure 38 2×10^{9} histories where run, which gave good statistics for all bins, thus all test are passed. In the case below in Figure 39, 10^{8} particles have been simulated, this tally corresponds to the same tally as above but with different number of histories. Thus, high relative errors are found in the bins with fewer sampled particles. However, the

bin of interest is 59.6keV. In the 59.6keV bin, all particles with energies in the range 48-59.6kev are detected. From Figure 39 we can see that 5.96keV bin has a low and good relative error of 0.0028. Thus, since the bin size of interest has been sampled sufficiently it is assumed that simulations run with 10^8 is sufficient and gives satisfactory data statistics for the energy bin of interest. This also leads to a manageable simulation run times of about 4 hours.

```
cell (16<42)
     energy
   0.0000E+00   0.00000E+00 0.0000
   1.0000E-05   1.81500E-07 0.0525
   1.0000E-03   5.00000E-10 1.0000
   4.8000E-02   5.38400E-06 0.0096
   5.9600E-02   6.56035E-05 0.0028
     total      7.11695E-05 0.0026
```

Figure 39.Tally f8 simulations with 10^8 particles. Left column are the energy bins in MeV, middle column shows number of detected particles in the respective bin and the column to the left shows relative error in respective bins.

5.3 Benchmarking of MCNP simulation model to experimental measurements

The developed simulation model has been benchmarked by fin-tuning or changing parameters in the input files. In this section the developed simulation model will be fine-tuned and validated. A chi-square test was used to find the optimal model geometry parameter. To enable comparison between all experimental and simulated data all the plots and data will be normalized.

5.3.1 Original MCNP simulation model compared to measurement data

In Figure 40 the original MCNP model without any fine-tuning is presented for full and empty pipe. By first observation, the detector counting response looks similar to the one that was observed in the discussed experimental plots previously, the simulated model shows clearly when the pipe is filled with 100% air and when it consists of 100% PP.

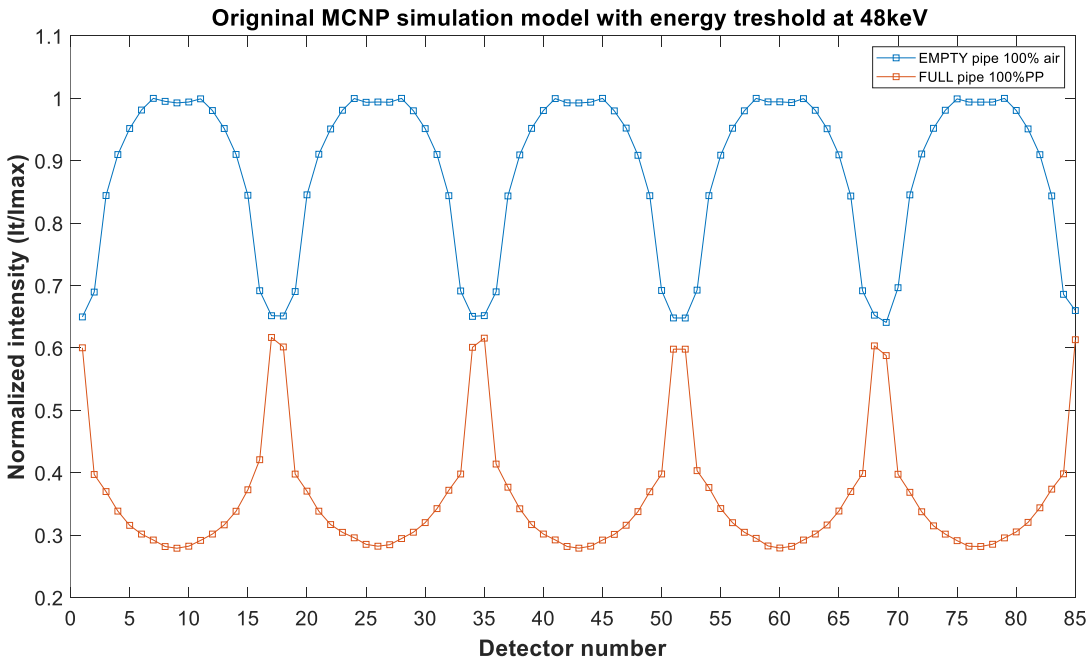

Figure 40. Results from MCNP simulation model, i.e. the detection profiles for empty and full pipe. This is the original MCNP simulation model without fine-tuning.

Below in Figure 41 the original MCNP model without fine-tuning has been plotted against experimental data, we observe overall agreement and similar behaviour.

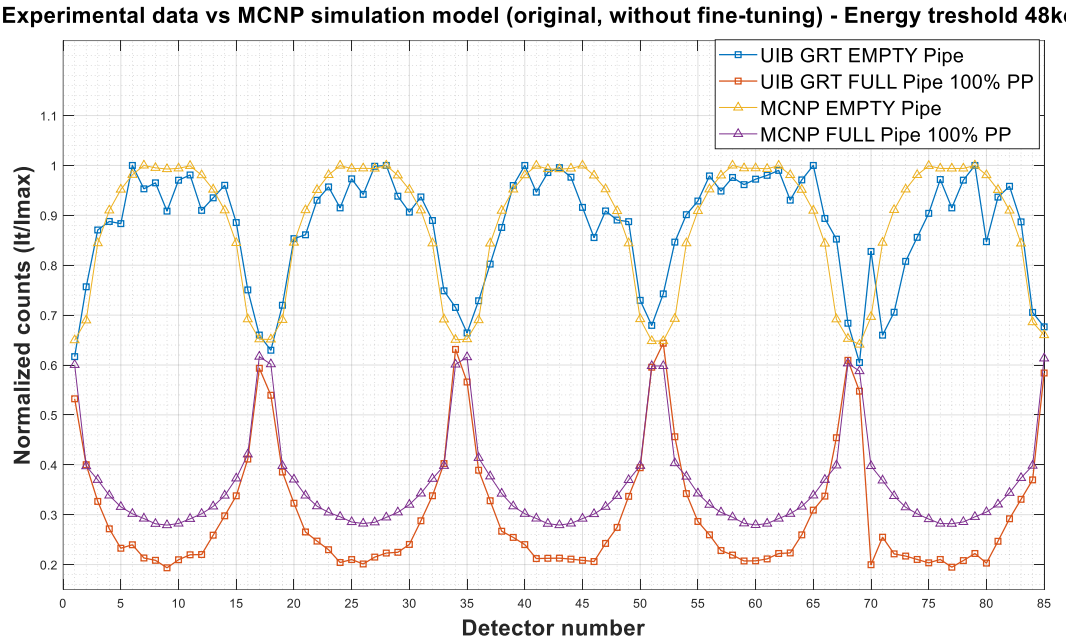

Figure 41. Results from MCNP simulation model versus Experimental measurements from the UiB GRT, i.e. the detection profiles for empty and full pipe.

However, a systematic error or bias is observed for full pipe between the experimental and simulated data of about 10%. This is due to higher count rates in the simulated model compared to the experimental data. Thus, an overestimation is observed in MCNP model, which must be corrected for by fine-tuning parameters in the developed simulation model. Number of registered counts must be reduced in the developed simulation model, to achieve a better fit of the simulation model. Empty pipe counting response shows a better agreement between experimental model and simulation model. However, the effects of pile-up in the experimental data leads to a differing behaviour in simulation model, thus a running mean will be applied later for the experimental data in the benchmarking process so that the trends in the experimental data become more evident.

5.3.2 Fine-tuning MCNP model

Since the geometry in UiB GRT is symmetric the benchmarking will be done for one detector module and corresponding source, thus is assumed that the remaining detectors and sources will exhibit a similar behaviour. The dimensions and sizes that are given in Table 7 must be altered in size to achieve a better simulation model fit to experimental data. Note, these dimension and sizes will be referred to as model parameters or just parameters.

Table 7. Initial parameter dimensions and sizes that will be altered to fine the simulation model that gives the lowest chi-square, thus the best fit.

Main model parameters	Initial value	Density range [g/cm^3]
Pipe-wall density	1.38g/cm^3 (PVC)	1.3-1.45
Phantom full pipe density	0.90g/cm^3 (PP)	0.85-0.92
Phantom empty pipe density	0.001205 g/cm^3	Density of air at 15°C

The benchmarking of the model has been executed by benchmarking detector module A (detectors 1-17), when only source A is open. Thus, below in Figure 42 the counting response in detector module A has been plotted for empty and full pipe for both experimental data and MCNP simulation data. Furthermore, Figure 43 shows the original experimental data plotted against the experimental moving mean data.

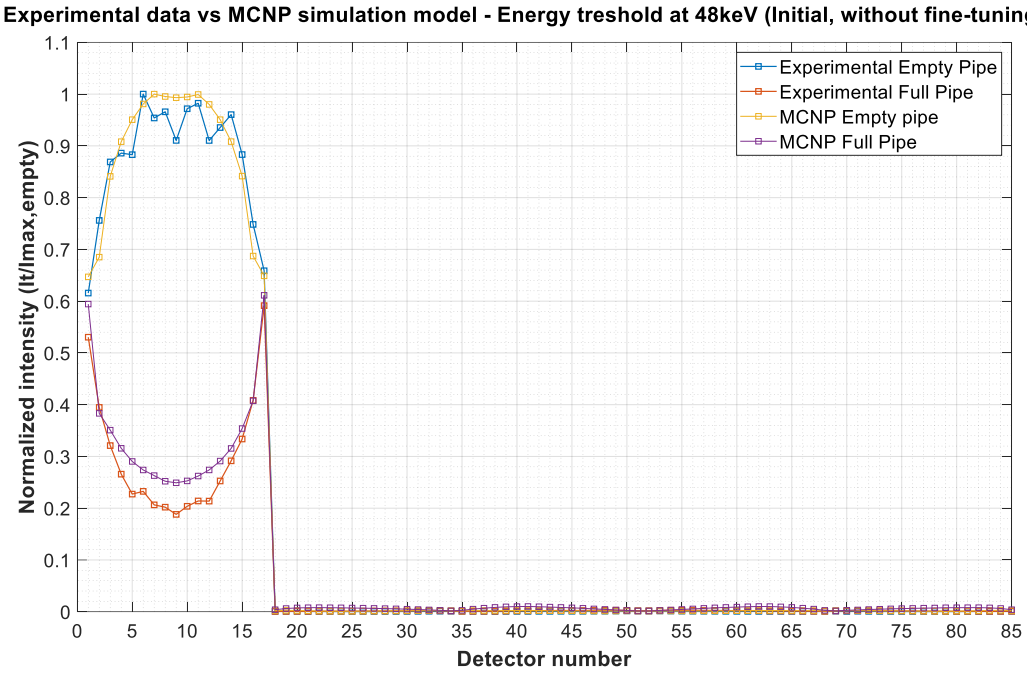

Figure 42. Couting system reponse from detector module A when only source A is open. Experiemntal data vs MCNP simulaton model.

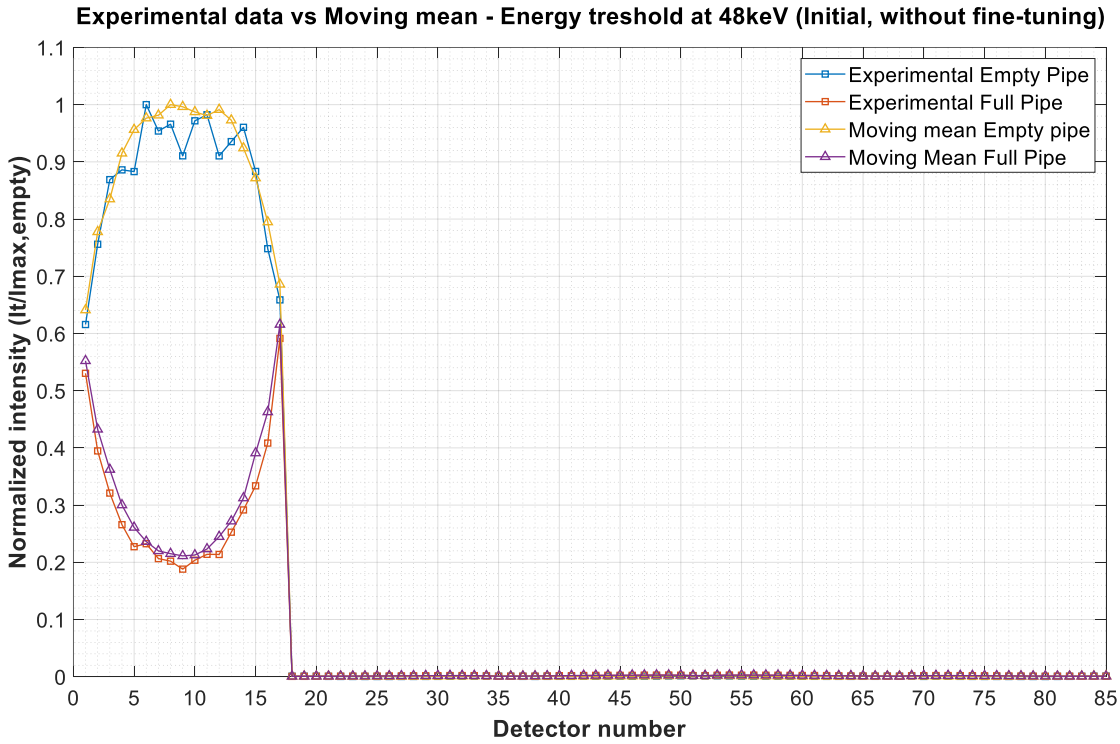

Figure 43. Couting system reponse from detector module A when only source A is open. Experiemntal Moving mean data vs Experiemntal measurements.

From Figure 43 we observe a good agreement between the experimental data and experimental moving mean data. Thus, this moving mean fit will be used when comparing experimental data to MCNP simulation data, since the moving mean

will account for the fluctuation that have been observed for the experimental data when the pipe is empty. Below in Figure 44 the moving mean experimental data has been plotted against the MCNP simulation model data. The initial model without any parameter alterations gives chi-square that are equal to χ^2_{empty}=0.0345 and χ^2_{full}=0.0648. The chi-square values have been calculated by using Equation (2.15).

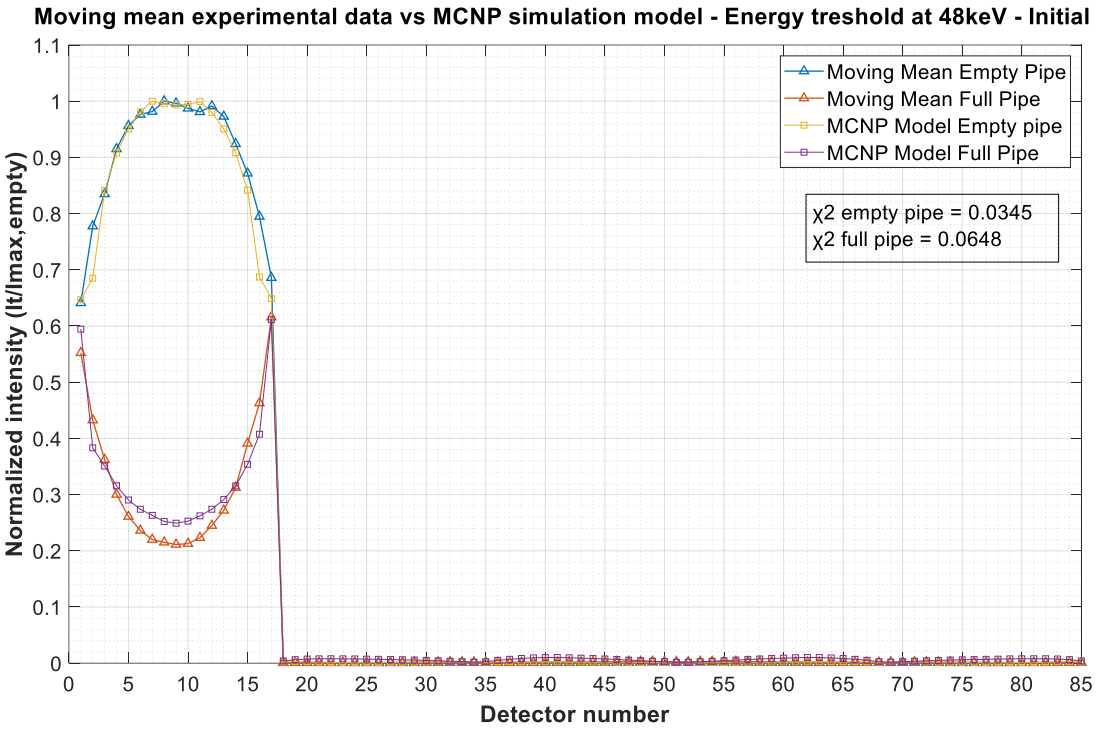

Figure 44. Couting system reponse from detector module A when only source A is open. Moving mean experiemental data vs MCNP simulaton model, intial MCNP model without fine-tuning.

From Figure 44 a statistical error between experimental moving mean data and MCNP simulation model is observed. Firstly, we will try to eliminate the statistical error by increasing the density of phantom which consists 100% PP, this will be done in the next sub section.

5.3.2 Phantom density 0.92g/cm^3

The phantom density for full pipe (PP) was changed from 0.90g/cm^3 to 0.92g/cm^3. Note, this only influences full pipe since when the pipe is empty there is no medium in the pipe. An increase of density leads to fewer particle counts in the detector. We want to reduce or eliminate the statistical error that has been observed between the experimental data and MCNP simulation model in Figure 44. Below in Figure 45 the moving mean experimental data for phantom density of 0.92g/cm3 has been plotted against the MCNP simulation model. This fine-tuning approach gives chi-square values that are equal to χ^2_{empty}=0.0364 and χ^2_{full}=0.0529.

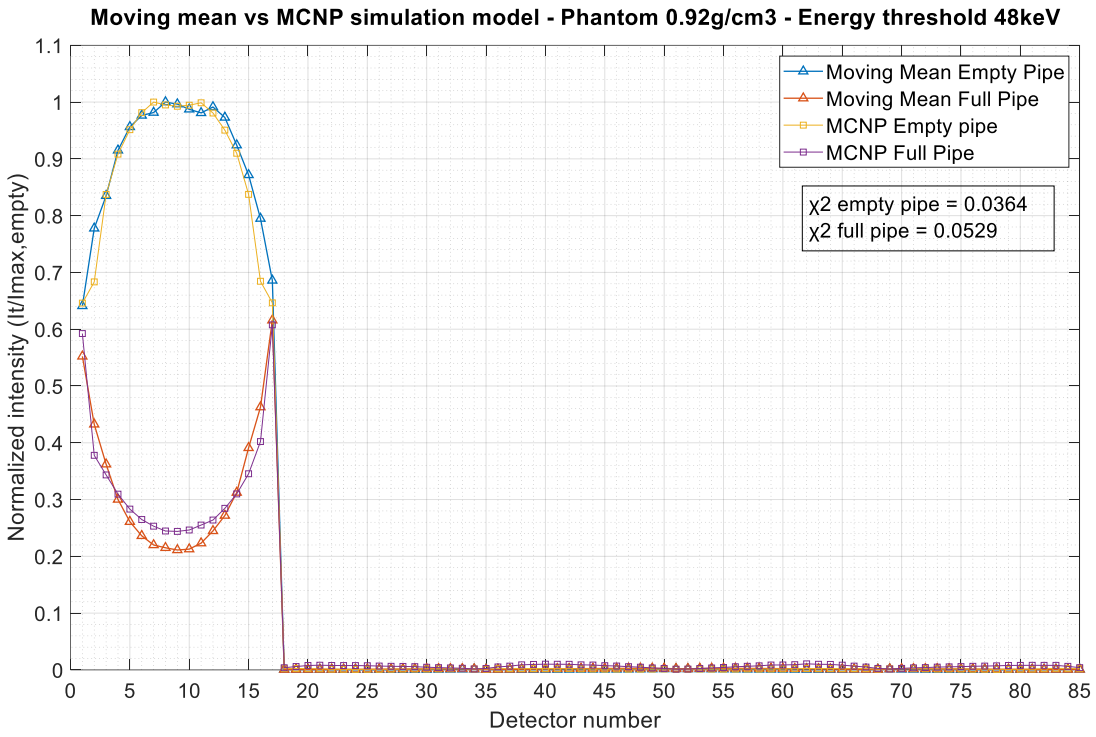

Figure 45. System counting response from detector module A, when only source A is open. Moving mean experimental data plotted against MCNP simulation model. Phantom density increased from 0.90g/cm^3 to 0.92g/cm^3.

5.2.3 Phantom density 0.92g/cm^3 and pipe-wall density 1.45g/cm^3

Furthermore, the phantom density for full pipe (PP) was changed from 0.90g/cm^3 to 0.92g/cm^3. In addition, the pipe-wall density was changed from 1.38g/cm^3 to 1.45/cm^3. Below in Figure 46 the moving mean experimental data for phantom density of 0.92g/cm^3 and pipe-wall density of 1.45g/cm^3 has been plotted against the MCNP simulation model. This fine-tuning approach gives chi-square values that are equal to χ^2_{empty}=0.0470 χ^2_{full}=0.0606.

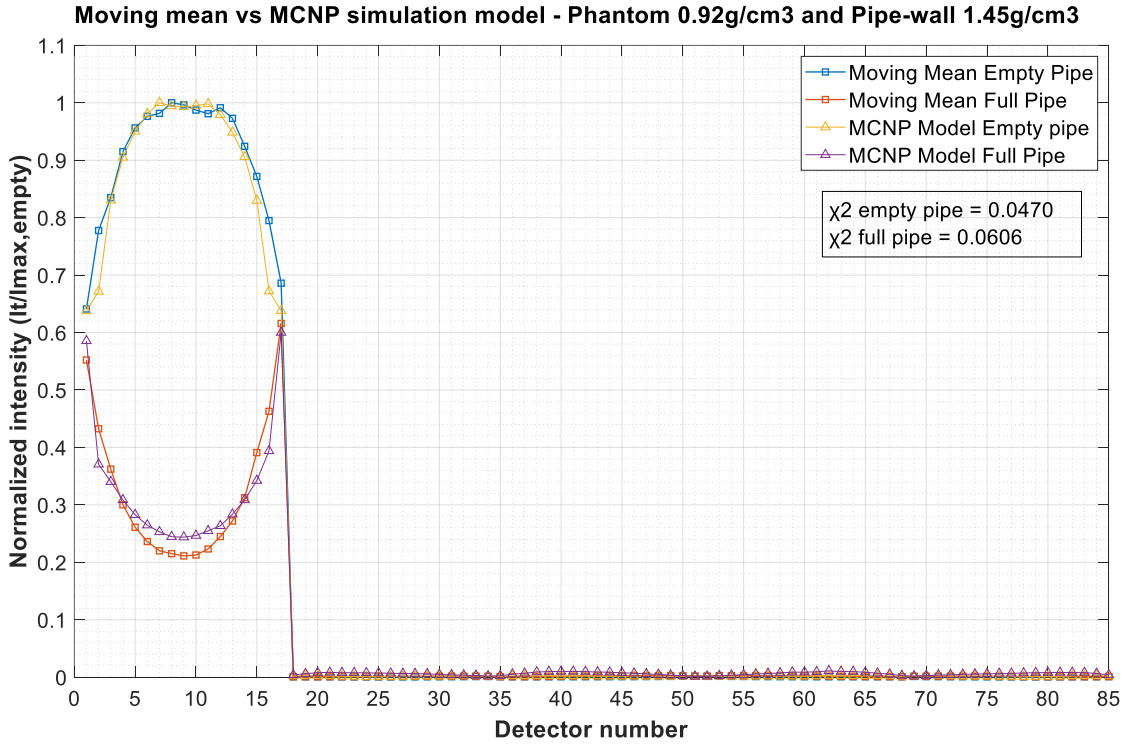

Figure 46. Couting reponse from detector module A when only source A is open. Moving mean experimental data versus MCNP simulation data. Density of phantom and pipe-wall are increased to 0.92g/cm^3 and pipe-wall density 1.45g/cm^3, respectivly.

5.2.4 Phantom density 0.92g/cm^3, pipe-wall density 1.45g/cm^3 and pipe diameter increased by 1%

Furthermore, the phantom density for full pipe (PP) was changed from 0.90g/cm^3 to 0.92g/cm^3. In addition, the pipe-wall density was changed from 1.38g/cm^3 to 1.45/cm^3 and the pipe diameter was increased by 1%. Below in Figure 47 the moving mean experimental data for phantom density of 0.92g/cm3, pipe-wall density of 1.45g/cm^3 and 1% increase of pipe diameter has been plotted against the MCNP simulation model. This fine-tuning method gives a chi-squares values that are equal to χ^2_{empty}=0.0478 χ^2_{full}=0.0609.

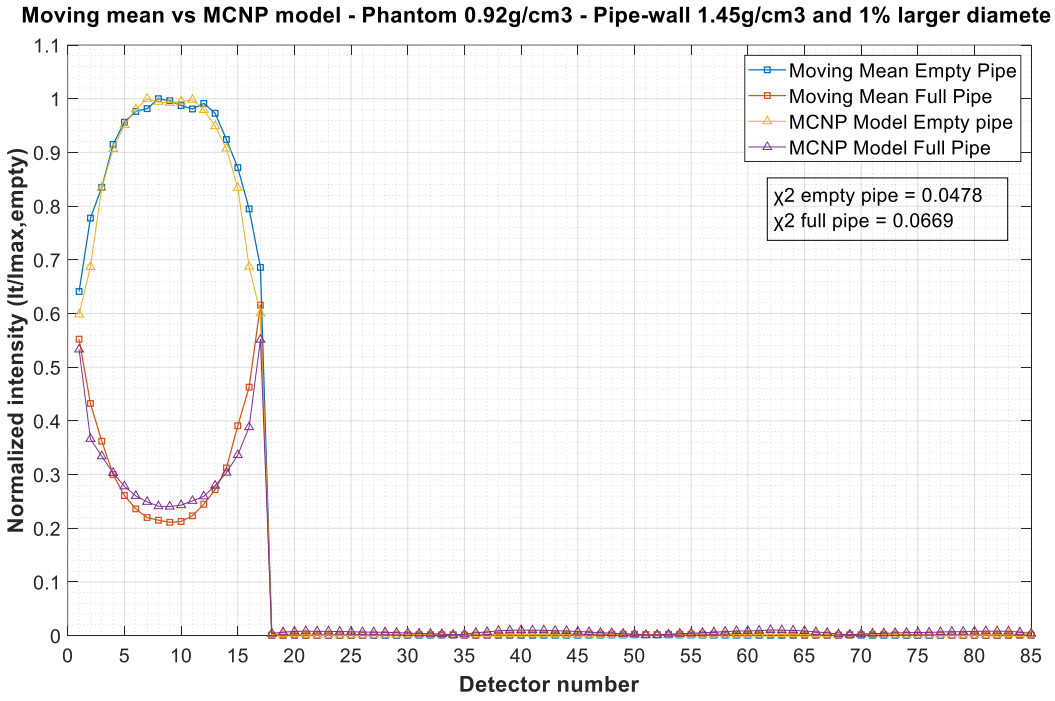

Figure 47. Couting reponse from detector module A when only source A is open. Moving mean experimental data versus MCNP simulation data. Density of phantom and pipe-wall are increased to 0.92g/cm^3 and pipe-wall density 1.45g/cm^3, respectivly. In addition, the pipe-wall diameter has been increased by 1%.

5.2.5 Overall discussion benchmarking parameters

Table 8 below summarises the chi-square sums from all the conducted fine-tuning approaches. The fine-tuning method that minimized the chi-square sums is the first approach, where the phantom density consisting of PP was altered from 0.90g/cm^3 to 0.92g/cm^3. This fine-tuning approach gives a chi-squares values that are equal to χ^2_{empty}=0.0364 χ^2_{full}=0.0529, thus the optimized parameters for the MCNP simulation model has been found.

Table 8. Chi-square values for the different fine-tuning approaches.

Fine-tuning method	χ^2_{empty}	χ^2_{full}
1 Phantom density PP 0.92g/cm^3	0.0364	0.0529
2 Phantom density PP 0.92g/cm^3 and Pipe-wall density PVC 1.45g/cm^3	0.0470	0.0606
3 Phantom density PP 0.92g/cm^3, Pipe-wall density PVC 1.45g/cm^3 and Pipe diameter increased by 1%	0.0478	0.0609

The uncertainty of the experimental measurements in UiB GRT where evaluated to be equal to be ±0.03 or 3% for the 17 detectors in each module, with a confidence interval of 95% (1 of the 17 data points is outside of range ±0.03). Due to the fluctuation that was observed for full pipe in the experimental data. As mentioned, number of counts where so high that the uncertainty contribution of square root of number of counts became negligible for the experimental measurements. Moreover, the uncertainty of the MCNP simulation model software is 0.1% (95% confidence interval).

By using the grid in Figure 45, this figure contains the plots that show the simulation model with 0.92g/cm^3 phantom density versus experimental moving mean data, which is the model with the minimized chi-square value. From this figure it can be found that are there is a deviation of 1.5 squares between the MCNP simulation model and moving mean experimental data for full pipe, which is equal to 3%. From this discussion the uncertainty of the developed MCNP model with 0.92g/cm^3 phantom density is evaluated to be a sum of the 3% uncertainty, which is the uncertainty for each detector in a module. And the deviation of 3% between the simulated and experimental data, due to overestimation of the simulation model. The combined relative uncertainty for the MCNP simulation model is given below (95% confidence interval).

$$u_{becnmarked,MCNP\ model} = \sqrt{(3\%)^2 + (3\%)^2} = 4\%$$

5.4 Contribution of Compton

Since the detector and source setup in the UiB GRT is symmetric, it is only necessary to find total Compton contribution to one module. It is therefore assumed that the remaining sources and detectors will exhibit the same behaviour. In this sub chapter, the Compton scattering to detector module B will be found by using the developed MCNP model, by plotting and quantifying the contribution from the different sources. When the UiB GRT is running under normal conditions all the sources are open, this enables image reconstruction. Thus, detector module B will detect counts that are transmitted and forward-scattered from source B, in addition to scattering contributions from sources A,C,D and E. Thus, under normal running conditions in the UiB GRT all hits in a detector are assumed to be transmitted and used for image reconstruction. However, we know that these transmitted photons also consist of scattering contributions. Detector module B consists of detectors 18-34 as mentioned previously. Sources D and E are adjacent to module B and positioned on each side of module B. Sources A and C are farther away, and are positioned on separate sides relative to detector module B. Source B is directly opposite of detector module B. A drawing of the setup has been presented in Figure 15. Thus, it is expected that sources A and C, in addition to sources D and E exhibit a similar behaviour since they positioned symmetrical. All counts have been normalized to max transmitted photons for empty pipe, when the corresponding source is open. E.g. Compton scattering from source A for full pipe to detector module B is found by taking number of hits detected when only source A is open divided by max intensity when only source A is open for empty pipe. E.g., if we want to find the number of transmitted photons that are detected in detector module B from source B (only source B open), then this quantity will be normalized to number of counts when only source B is open, and the pipe is empty. Energy threshold for all experimental measurements and MCNP simulations is set 48keV. Moreover, the relative expanded uncertainty for the developed MCNP simulation model is 4%, and the experimental measurements have a relative expanded uncertainty of $\pm 3\%$.

5.4.1 Scattering from sources A, C D and E to detector module B – MCNP – Full pipe

The individual Compton scattering contributions from sources A and C to detector module B is presented below in Figure 48 and Figure 49 for full pipe.

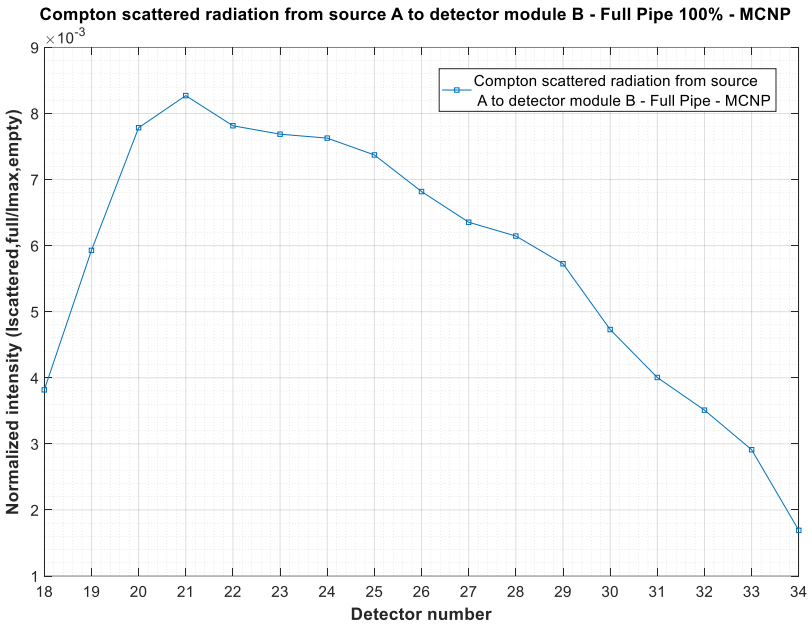

Figure 48. This plot shows Compton scattering from source A to detector model B, for full pipe. The data is based on data from developed MCNP model.

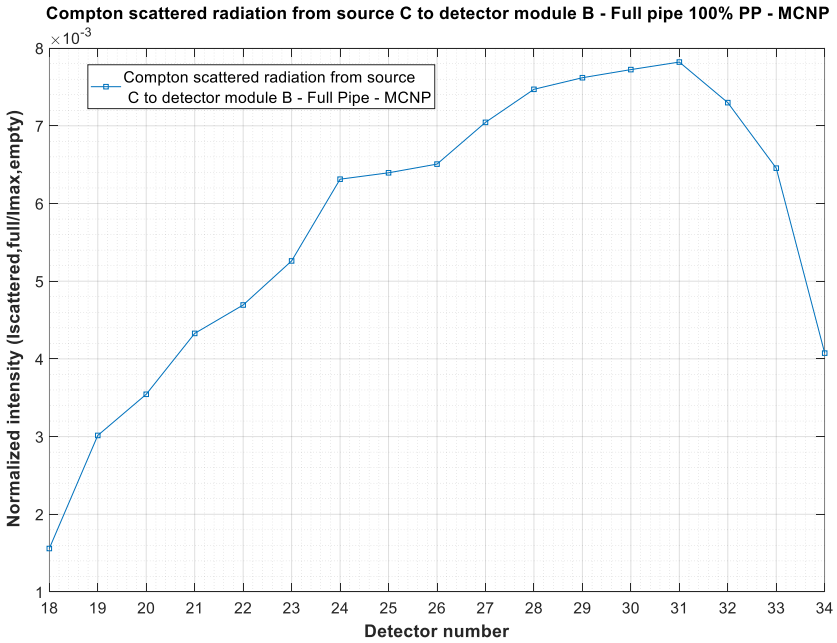

Figure 49. This plot shows Compton scattering from source C to detector model B, for full pipe. The data is based on data from developed MCNP model

As mentioned, detectors A and C are the sources that are positioned the farthest away from detectors module B, they are positioned on opposite sides of detector module B, thus they are symmetrical positioned relative to detector module B. From Figure 48 and Figure 49 we observe symmetry in the counting responses distribution from sources A and C to detector module B. Which can be seen by the fact that the counting response distributions have a similar shape (symmetric) which is skewed to opposite sides. Furthermore, the magnitude of the relative counting intensities are in the same range as for the individual sources A and C. Max scattering from source A in Figure 48 is found in detector 21 and is equal to 0.0083 or 0.82% of total transmitted beam. While maximum scattering from source C in Figure 49 if found in detector 31 and is equal 0.0078 or 0.78% of total transmitted beam. Below in Figure 50 and Figure 51 the individual Compton scattering contributions from sources D and E to detector module B for full pipe is presented.

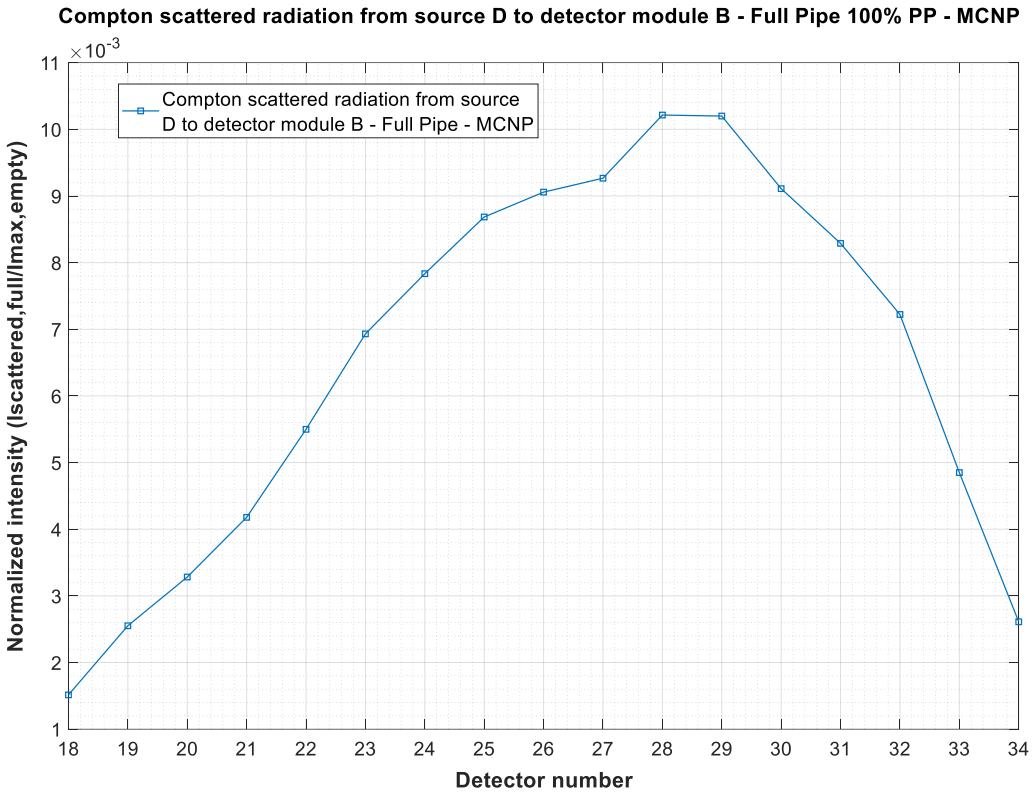

Figure 50. This plot shows Compton scattering from source D to detector model B, for full pipe. The data based on data from developed MCNP model

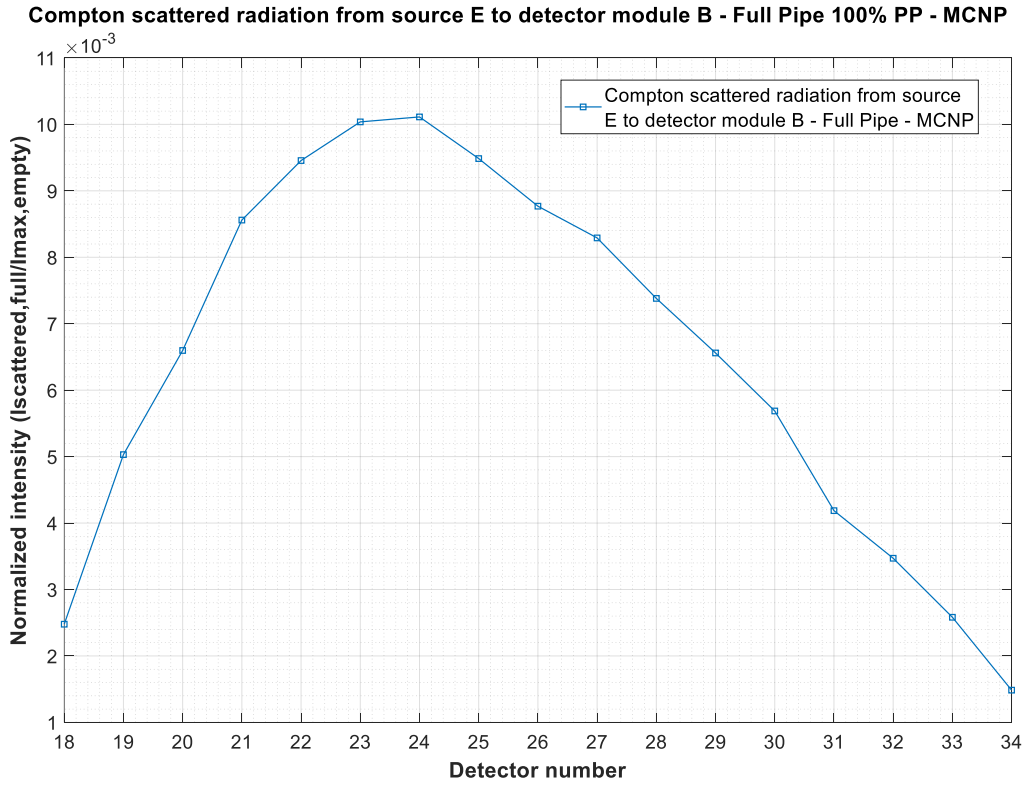

Figure 51. This plot shows Compton scattering from source D to detector model B, for full pipe. The data based on data from developed MCNP model

Table 9 below summarises the mean, maximum and minimum values of Compton scattering from respective sources that have been presented above, for full pipe. The units in the table are given in relative photon intensities, thus the amount of scattering originating from a source can be found in percent by multiplying the values by a 100. Studying the Compton contribution for full pipe shows that the amount of Compton that occurs when there is a medium in the pipe. Thus, the scattering is a sum of scattering in the medium, pipe-walls and collimator blades. As mentioned previously, the source -and detector housing has not been included in the simulation geometry, thus these scattering contributions are not included.

Table 9.. Full pipe normalized to max counts for empty pipe. The ratios in the table show the amount of scattered radiation that been detected relative to the total transmitted intensity.

	Compton from source A	Compton from source C	Compton from source D	Compton from source E
Mean	0,0058	0,0057	0.0065	0,0065
Max	0,0083	0,0078	0.0102	0,0101
Min	0,0017	0,0016	0,0015	0,0015

From Table 9 we observe similar mean, maximum and minimum values of the relative system counting responses to detector module B, from sources A and C,

and the sources D and E. This is due to the symmetrical setup of the UiB GRT. However, the individual mean values for all the sources are not far apart. From all of the scattering contributions from sources A,C,D and E it is observed higher count rates in the detectors that are positioned farthest away from the sources. E.g. scattering from source D to detectors module B can be seen in Figure 48. Source D is positioned directly besides module B on the left side, and the higher counts rates are detected in the detectors 26-34, which are farthest away from source D. Furthermore, source E which is positioned directly besides detector module B on the left side, gives the highest scattering contribution in detectors 18-26, these are the detectors that are farthest away from source E. Forward scattering or build-up from source B has not been considered in this study and may be included in future work.

5.4.2 Scattering from sources A, C D and E to detector module B – MCNP – Empty pipe

The individual Compton scattering contributions from sources A and C to detector module B are presented below in Figure 52 and Figure 53 for empty pipe.

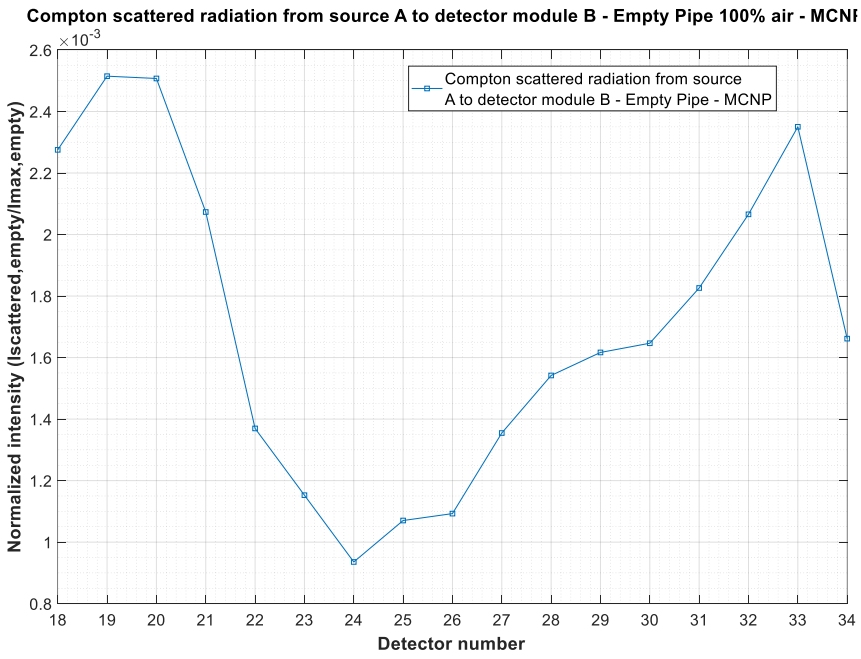

Figure 52. This plot shows Compton scattering from source A to detector model B, for empty pipe. The data is based on data from developed MCNP model.

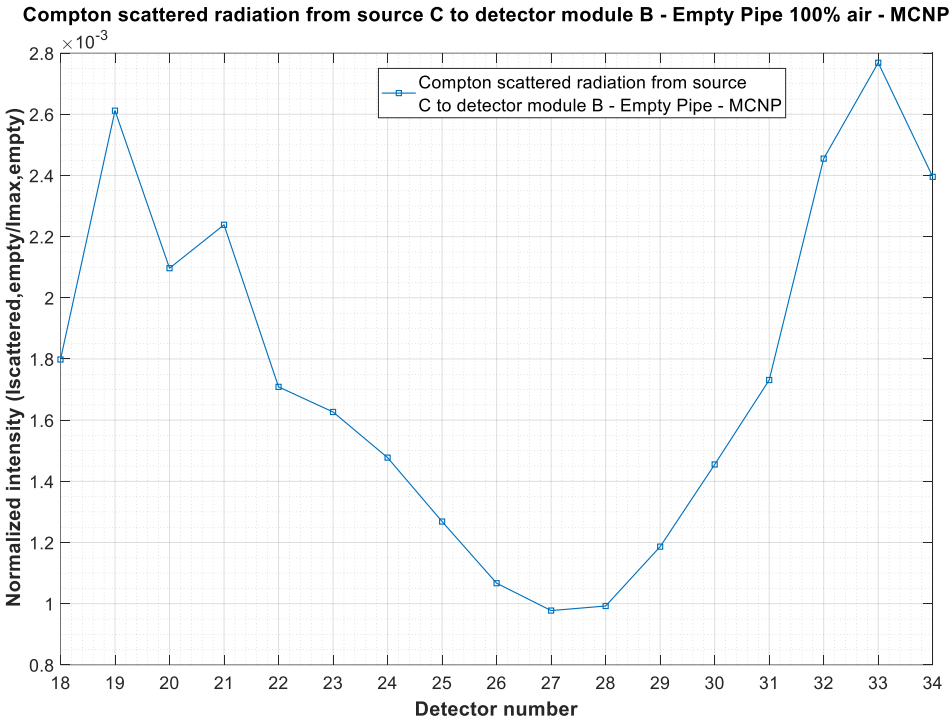

Figure 53. This plot shows Compton scattering from source C to detector model B, for full empty. The data is based on data from developed MCNP model.

The same behaviour that was observed for empty pipe can been seen for full pipe. A skewed symmetry can be seen from the counting responses from sources A and C in detectors module B, respectively Figure 52 and Figure 53. This skewed symmetry is clearly illustrated when observing the areas of minimum counting response, since these minima are skewed in opposite directions. Studying the Compton contribution for empty pipe shows the amount of Compton scattering that occurs when there is no medium in the pipe. Thus, the scattering contributions for empty pipe is primarily due to scattering that has occurred in pipe-walls and collimators blades. As mentioned previously, the source -and detector housing has not been included in the simulation geometry, thus these scattering contributions are not included. The increased Compton scattering contribution that can be seen in the outer detectors in Figure 52 and Figure 53 might be due to increased scattering in the pipe-wall. Since the outer photons from the sources might travel a farther distance in the pipe-wall compared to photons that are detected in the middle detectors. Thus, these outer photons might experience more Compton scattering since the probability of Compton scattering increases with increasing distance travelled in the absorber material. Moreover, for the ^{241}Am sources that are used in the UiB GRT that emit E_γ=59.5 keV photons, backscattering and scattering in all directions will occur since the photons have low energy. The scattering that occurs in the middle detectors in

Figure 52 and Figure 53 could primarily be due to scattering events in the collimator blades. Below in Figure 54 and Figure 55 the individual Compton scattering responses from sources D and B in detector module B are presented for empty pipe.

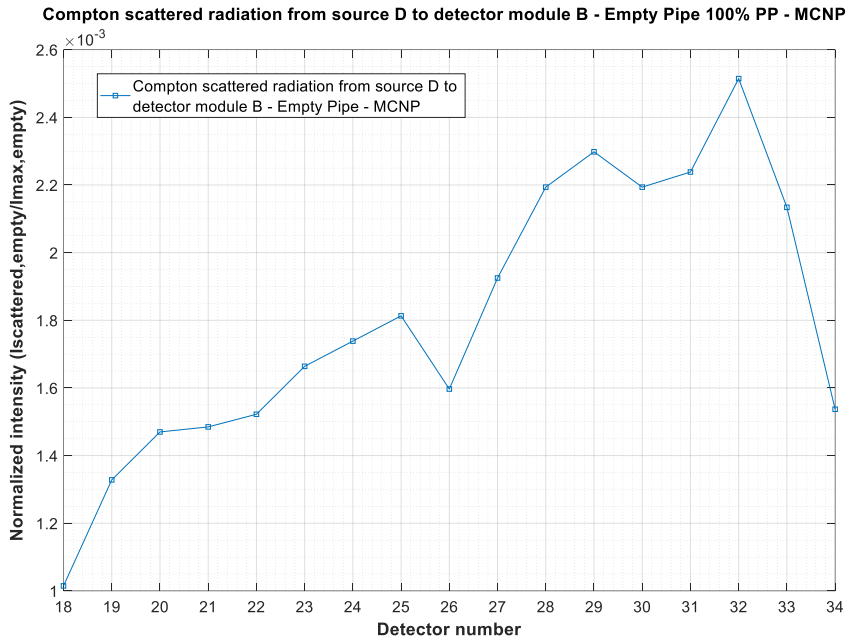

Figure 54. Compton scattering from source D in detector module B

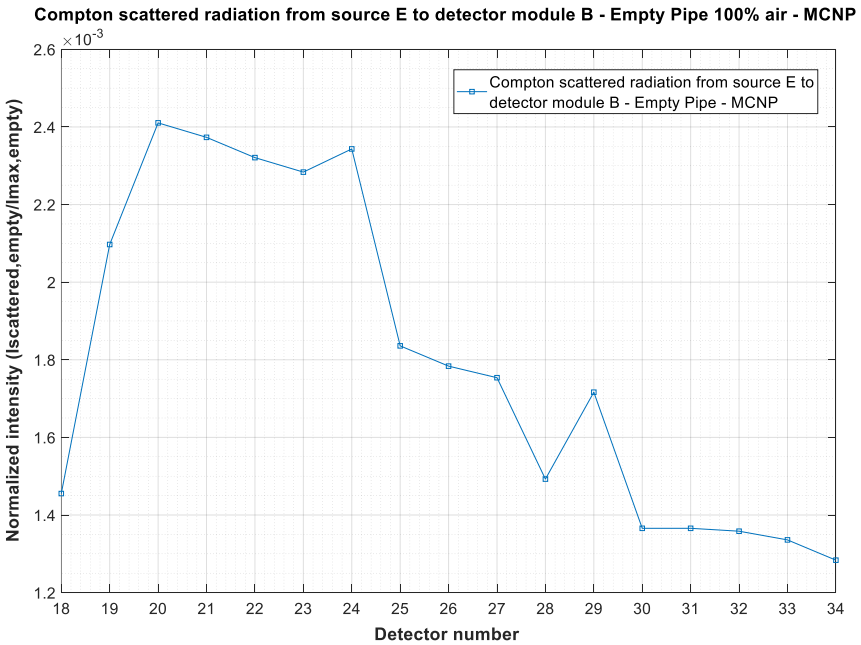

Figure 55. Compton scattering from source E in detector module B

As previously, a skewed symmetry can be seen for counting responses from sources D and E which are positioned directly besides and on opposite sides of detector module B, respectively Figure 54 and Figure 55. Higher scattering rates detected in the detectors that are farther away from the sources which could be due to photons that have been scattered in the pipe-wall, and backscattered to detector module B. Table 10 below summarises the mean, maximum and minimum values of Compton scattering from respective sources A,C,D and E to module B.

Table 10. Empty pipe normalized to max counts for empty pipe. The ratios (numbers between 0 and 1) in the table show the amount of scattered radiation that has been detected relative to the total transmitted intensity in detector module B

	Compton from source A	Compton from source C	Compton from source D	Compton from source E
Mean	0,0017	0.0018	0,0018	0,0018
Max	0,0025	0,0028	0,0025	0,0024
Min	0,00094	0,00098	0,0010	0,0013

From Table 10 we observe similar values of mean, maximum and minimum of the relative counting responses from sources A and C, and the sources D and E, which is due to the symmetrical setup in the UiB GRT. From all of the scattering contributions from sources A, C, D and E to detector module B, it is simulated higher count rates in the detectors that are positioned farthest away from the sources. By comparing the mean values that are presented for empty pipe in Table 10 and for full pipe in Table 9, there is observed almost identical mean values for all the individual counting responses for empty pipe in Table 10. In addition, significant higher relative system counting rates are observed for full pipe in detector module B, which can be seen in Table 9.

5.5 Discussion and conclusion

5.5.1 Comparison between Total Compton scattering for Full -and Empty pipe – MCNP simulation data

In Figure 56 the total Compton scattering contribution from sources A, C, D and E for full pipe has been plotted against the total Compton scattering contribution for full pipe, the system counting response is from detector module B. Thus, the total contributions have been found by summing the individual contributions that have been discussed previously. From Figure 56 we observe significant higher relative counting rates for full pipe compared to empty, which is expected since more Compton scattering will occur when the photon travel through denser matter. For full pipe the relative contribution for scattered radiation is found in the middle detectors of module B. While for empty pipe there is observed a more homogenous scattering distribution in all the detectors. However, higher count rates can be observed in detectors 19-26 in detector module B. Energy threshold for all experimental measurements and simulations is set to 48 keV. Moreover, the relative expanded uncertainty for the developed MCNP simulation model is ±4%, and ±3% for the experimental measurements (95% confidence interval).

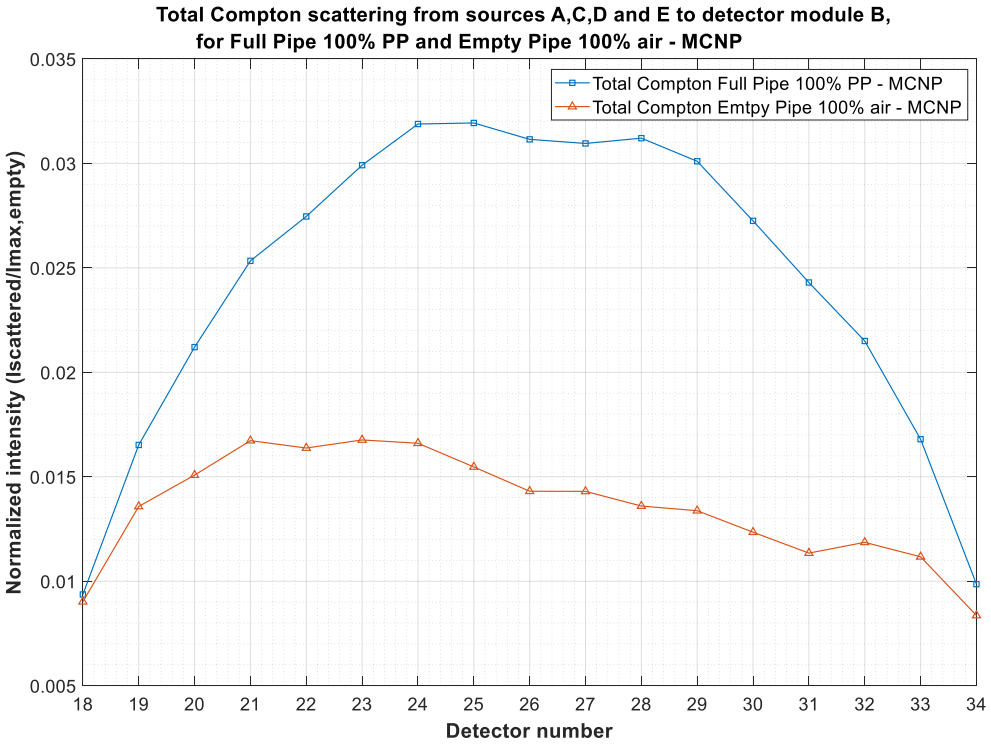

Figure 56. Total compton scattering from sources A,C,D and E to detector module B. Total compton scattering controbution for Full pipe vs Total compton scattering controbution for empty pipe

Table 11 summarises the mean, maximum and minimum values of total Compton scattering for full pipe and total Compton scattering for empty pipe, the data is obtained from the developed MCNP simulation model.

Table 11. Total Compton scattering for full pipe and empty pipe based on developed MCNP simulation model. The ratios (numbers between 0 and 1) in the table show the amount of scattered radiation that been detected relative to the total transmitted intensity, in the system counting response from detector module B.

	Total Compton Full Pipe MCNP	Total Compton Empty MCNP
Mean	0,0245	0,0135
Max	0.0319	0,0168
Min	0,0094	0,0084

5.5.2 Comparison of Experimental data vs MCNP simulation data - Total Compton scattering

Figure 57 shows the total Compton scattering contributions for full pipe from sources A, C, D and E to detector module B. Where the blue plot shows the total Compton scatter in module B based on experimental data, while the red plot shows total Compton scatter in module B based on MCNP simulated data.

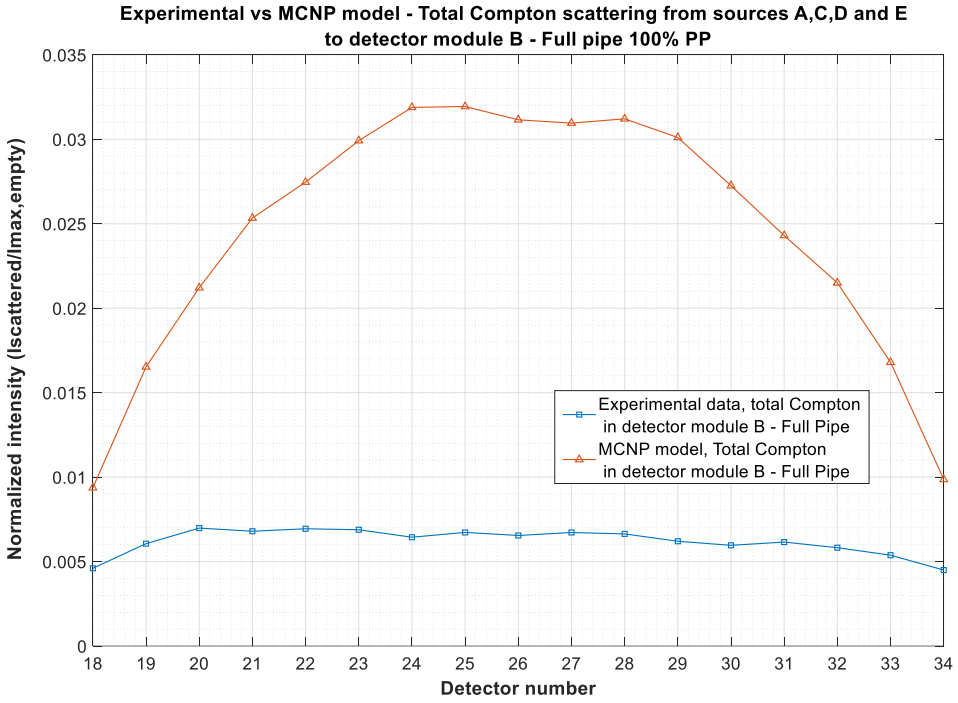

Figure 57. Total Compton scatter in detector module B from sources A, C, D and E for Full Pipe. Experimental data vs MCNP simulation data

In Figure 57 there is observed significant higher Compton scattering rates in the developed MCNP simulation model compared to the acquired experimental data from the UiB GRT. In the MCNP simulation a mean of 0.0245 or 2.45% of the transmitted counts are due to Compton scattering for full pipe. While the experimental data shows that a mean of 0.0062 or 0.62% of the transmitted counts are due to Compton scattering. This difference between experimental data and MCNP simulations might be due to the detector electronics of the UiB GRT. E.g. pile-up, detector dead time and to low timing resolution, where the latter is the detectors inability to detect counts since the hits are too close in time, thus several counts may be detected as one count. It could also be due to simplifications in the geometry setup for the MCNP model. Implementation of more geometry might reduce the overestimation in the MCNP simulation model, since more dense material in the system will lead to fewer detected counts. Figure 58 below shows the total Compton scattering from sources A, C, D and E to detector module B for empty pipe. Where the blue plot shows the total Compton scatter in module B based on experimental data, while the red plot shows total Compton scatter in module B based on MCNP simulation data.

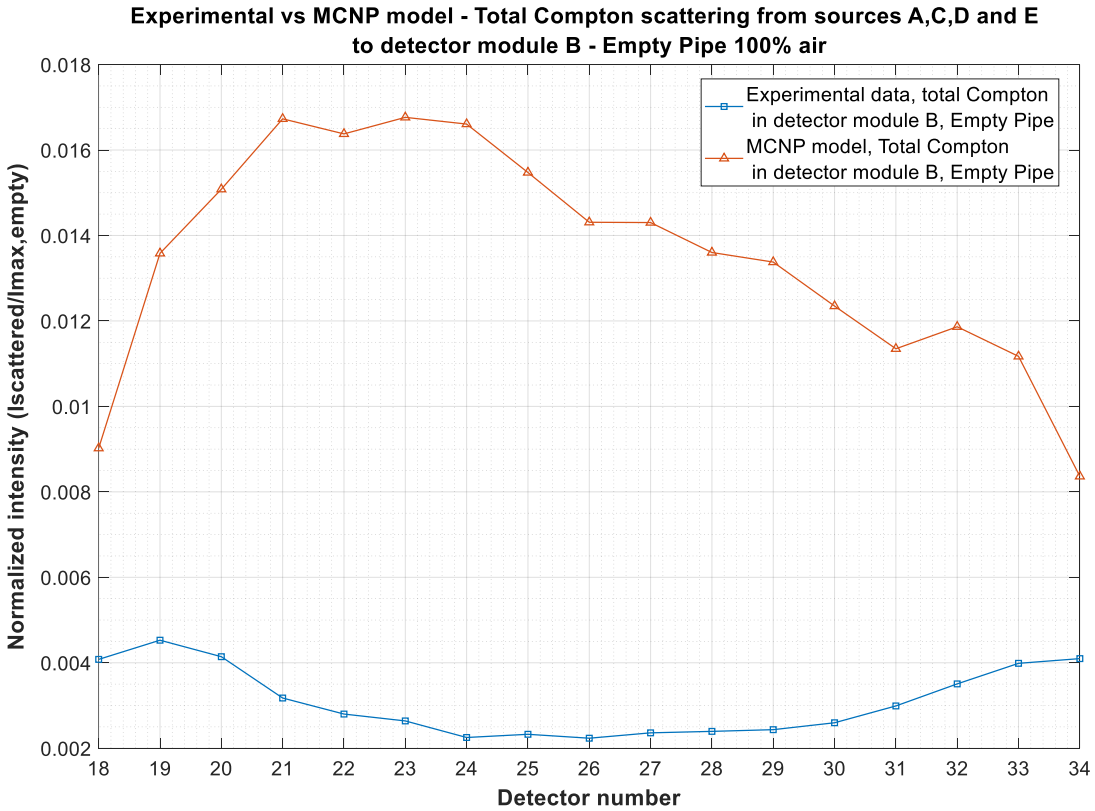

Figure 58. Total Compton scatter in detector module B from sources A, C, D and E for Empty Pipe. Experimental data vs MCNP simulation data

In Figure 58 we observe higher relative Compton scattering rates in the developed MCNP simulation model compared to the experimental data. This could be due to simplifications in the geometry setup for the MCNP model, e.g. source -and detector housings are not included in the developed model. Both MCNP simulation model and experimental data show significant lower counting rates for full pipe compared to empty which is expected. Table 12 summarises the mean, maximum and minimum values of total Compton scattering for experimental data and MCNP simulation model data that has been detected in detector module B. From Table 12 we observe significant higher counting rates in MCNP simulation model and higher Compton scattering rates for full pipe.

Table 12. Total Compton scattering for full pipe and empty pipe for experimental data and MCNP simulation model data. The ratios (numbers between 0 and 1) in the table show the amount of scattered radiation that been detected relative to the total transmitted intensity in system counting response of detector module B

	Total Compton Full Pipe MCNP	Total Compton Full Pipe experimental	Total Compton Empty Pipe MCNP	Total Compton Empty Pipe experimental
Mean	0,0245	0.0062	0,0135	0.0031
Max	0.0319	0.0070	0,0168	0.0045
Min	0,0094	0.0045	0,0084	0.0022

5.5.3 Compton contribution under normal running conditions of UiB GRT

During normal running conditions in the UiB GRT all the sources are open, which means that the detectors in the UiB GRT registers all hits as transmitted photons. When all sources in the UiB GRT are open, detector module B will receive counts due to Compton scattering from sources A, C, D and E, transmitted photons from sources B and forward-scattering from source B. In this scope of this work forward scattering will not be quantified. In the UiB GRT all detectors hits are assumed to be transmitted photons, thus both Compton scattered, and un-collided photons are detected as transmitted counts and used as input to the reconstruction algorithm. Consequently, the Compton scattered photons that are detected as photons contribute to additional noise which may blur and make the reconstructed image less accurate. Furthermore, this addition noise may result in less contrast in the reconstructed image. Therefore, it is of interest knowing the

amount of Compton scattering the input data to the reconstruction algorithm contains. Thus, to find the amount of Compton scatter in the experimental data the following relationship below must studied. It is important to acknowledge and understand that the relationship that is given in the denominator of this ratio is how actual measurements are taken experimentally in UiB GRT. Since under normal running conditions all of the sources (A,B,C,D and E) in the UiB GRT are open. Furthermore, the relationship in numerator, which is Compton scatter to module B was found by adding the individual contributions in detectors 18-34 from each of the sources A,C,D and E. As previously, an integration time of 20 seconds has been used to minimize statistical uncertainty. To find the same relationship for the MCNP simulation model, the following relationship below must be found for the experiments:

$$\frac{\text{Total Compton scatter to detector module B (sum contributions from sources A, C, D and E)}}{\text{All sources open, system counting response from detecor module B (18 to 34)}}$$

Where the numerator is detected counts in detector module B when sources A, C, D and E are open, thus this is the scatter contributions from adjacent sources to module B. While the denominator is the system counting response in detector module B, when all sources are open. By calculating this ratio, we find the ratio of Compton scattered radiation in detector module B from adjacent sources. As can be seen, the numerator quantity is found by the same means for the simulation data and experimental data. However, the denominator for the MCNP must be found by adding different quantities, since as mentioned, the denominator for the experimental relationship is the data output under normal running conditions from the UiB GRT. Thus, the denominator quantity for MCNP simulation has been found by summing total Compton scatter to detector module B and number of counts in detector B when only source B. The latter must be included too, so that build-up and un-collided hits from source B are detected in the system response of detector module B. The ratio for the MCNP simulation results is then:

$$\frac{\text{Total Compton scatter to detector module B (sum contributions from sources A, C, D and E)}}{\text{Total Compton scatter in source B + Number of counts in detecor B when only source B is open}}$$

Below in Figure 59 and Figure 60 these discussed ratios that show the amount of Compton scattering in actual measurement data have been plotted for both experimental data and MCNP simulation data, for full and empty pipe. The blue plots are based on the developed MCNP model and the red plots are experimental data from the UiB GRT. We observe significant higher Compton scattering rates in the simulation MCNP simulation model compared to the experimental data.

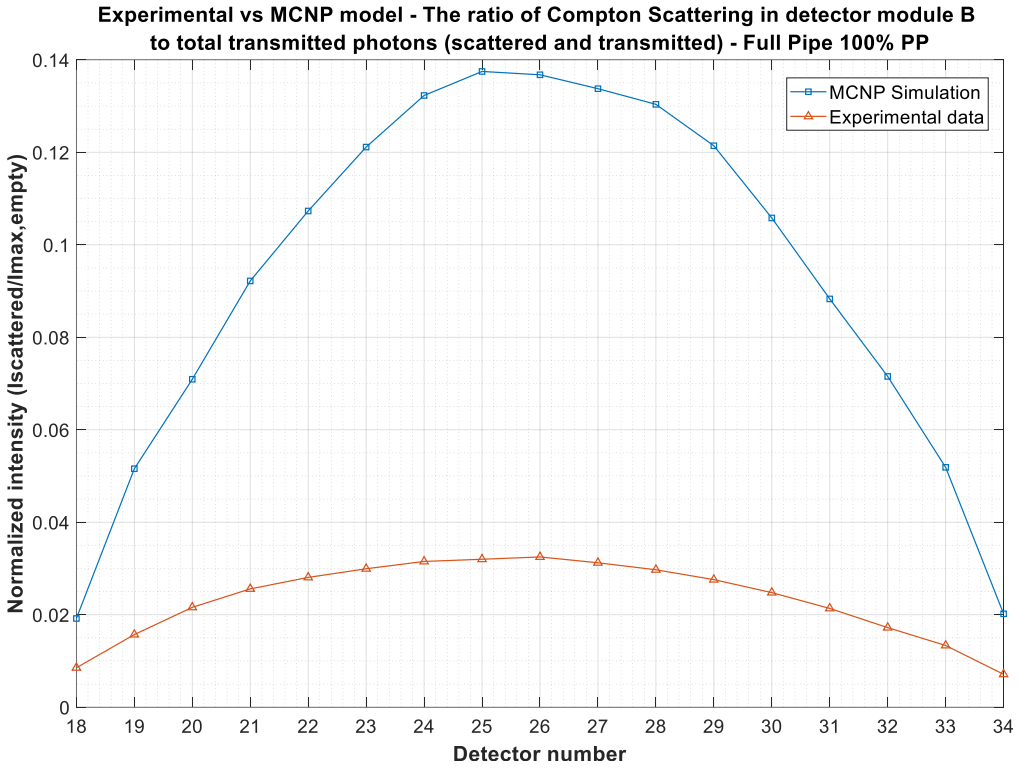

Figure 59. Ratio of Compton in actual reconstruction data. Experimental data vs MCNP model, Full pipe

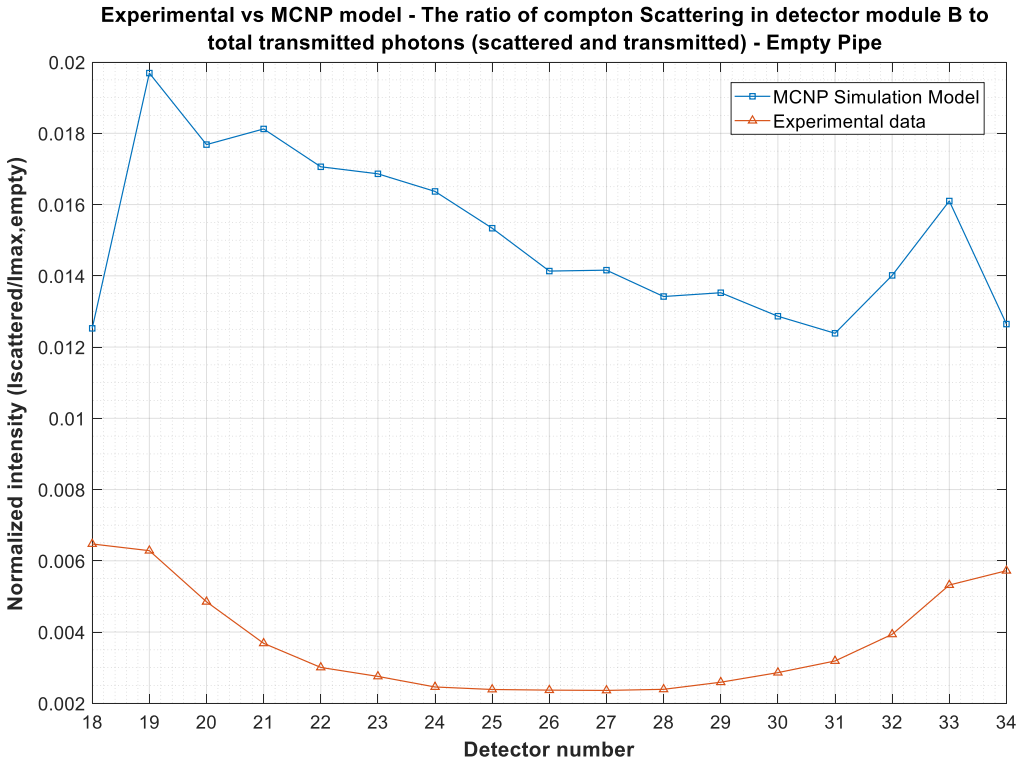

Figure 60. Ratio of Compton in actual reconstruction data. Experimental vs MCNP model, Empty pipe

Table 13 summarises the mean, maximum and minimum values of the amount of Compton scattering that is present under normal running conditions in the UiB GRT for both experimental data and MCNP simulation model data.

Table 13. The ratio/amount of Compton scattering that is present in actual measurement data UiB GRT which is used for reconstruction of images. The ratios (numbers between 0 and 1) in the table show the amount of scattered radiation that been detected relative to the total transmitted intensity

	MCNP Full pipe	Experimental Full Pipe	MCNP Empty pipe	Experimental Empty Pipe
Mean	0.0937	0.0234	0.0151	0.0037
Max	0.1375	0.0325	0.0197	0.0065
Min	0.0192	0.0071	0.0124	0.0024

Thus, from Table 13 and Figure 59 we observe that with a medium in the pipe (full pipe) the MCNP simulation model finds that reconstruction data in the UiB GRT contains 9.37% Compton scattering counts (mean). While the experimental data gives a total of 2.34% Compton scattering in data that is input to the reconstruction algorithm. As mentioned, this difference between experimental data and MCNP simulation model may be due to the limited model geometry description in the MCNP model or the detector electronics of the UiB GRT. Significant higher Compton scattering rates are found for full pipe compared to empty pipe which is expected.

5.6 Over all discussion and summary

In this thesis project a MCNP simulation model of the UiB GRT has been developed. This has been done by benchmarking the developed model to experimental and finding the parameters that minimize the chi-square sum, which was found when the density of the pipe-wall material was set to a density ρ=0.92 g/cm^3 (PP). Thus, this thesis has consisted of both simulations, experimental runs on UiB GRT and comparison between simulation runs and experimental response. By studying the scattered radiation for with a medium inside the pipe, the total scatter contribution was studied. While the study of scattered radiation when the pipe is empty allows the study of scatter contribution from collimator and pipe-wall.

Significant more Compton scattering occurred for full pipe compared to empty pipe, which was expected since the probability of Compton scattered increases with a farther travel distance in denser material. When simulating normal running conditions of the UiB GRT in MCNP the following results where obtained: For empty pipe 1.51% of the transmitted photons where due to Compton scatter, and for full pipe 9.37% of the transmitted photons where found to be due to Compton scatter. While the experimental data from the UiB GRT showed that for empty pipe, 0.37% of transmitted photons where due to Compton scatter, and full pipe showed that 2.34% of the transmitted photons where due to Compton scatter. The empty pipe simulations indicate the amount of scatter that is due to the collimator blades and pipe-walls, while full pipe indicates the scatter of the whole system. From this we can observe that the developed MCNP model overestimates the Compton scatter contribution compared to the experimental data. Implementation of more geometry to the MCNP model may reduce the overestimation, since this will both make the model more accurate. Moreover, adding e.g. the detector housings or source housings will reduces number of detected counts, since there will be more dense material in the system. Thus, this might reduce the overestimation of the developed model. Furthermore, the additional geometry in the actual UiB GRT might cause Rayleigh-scattering of photons away from the detector, which may lead to fewer counts in the experimental measurements, this is something that can be simulated and checked in future projects. More geometry should be added to the simulation model and more simulations should be run before it is possible to conclude and say that the developed model in fact behaves as the experimental data. Energy threshold for all experimental measurements and MCNP simulations is set 48keV. Moreover,

the relative expanded uncertainty with a 95% confidence interval is ±4 for the developed MCNP simulation model and ±3% for all experimental measurements.

Chapter 6

The development of the MCNP simulation model of the UiB GRT enables a vast and deeper study of interactions that occur in the UiB GRT, e.g. build-up, energy spectrum, Rayleigh scattering, finding the optimal collimator blade length of collimator blades, etc. Future work should therefore focus on finding the cause of overestimation that has been observed in the developed MCNP model. By finding and reducing this observed deviation between experimental and MCNP simulation model, one may in the future be able to conclude and say that the developed model in fact behaves as the experimental data. When the model behaves as the experimental data, the model can be used to explore vast areas.

Future work

Future work should include:

1. Implementing a more detailed model of the UiB GRT in MCNP
2. A sensitivity analysis should be performed to reveal the potential causes of the disagreement between the simulated and experimental data. In doing so, one should follow a step-by-step approach and implement first the source holders, thereafter detector housing, followed by other solid structures around the source - detector modules as well as the pipe section in the centre of the UiB GRT.
3. Energy spectra should be included, this enables the study of energies of the scattered photons. This is highly relevant and can help estimate contributions from Rayleigh scattered photons and not just Compton scattered photons.
4. One should also try to identify the major contributor to scattered radiation intensity, explore in which way this contribution can be reduced / optimized without compromising the imaging resolution in the UiB GRT
5. Estimated scatter rates should also be confirmed with the semi-empirical model of R. Maad and the LLS approach of I. Meric.

References

[1] G. A. Johansen and P. Jackson, Radioisotope Gauges for Industrial Process Measurements, West Sussex: Wiley, 2004.

[2] "National Cancer Institute at the National Institutes of Health," National Cancer Institute (NCI), the U.S. government's principal agency for cancer research, 8 April 2018. [Online]. Available: https://www.cancer.gov/about-cancer/diagnosis-staging/ct-scans-fact-sheet. [Accessed 9 July 2019].

[3] IAEA-TECDOC-1589, "Industrial Process Gamma Tomography Final report of a coordinated research project 2003–2007," IAEA International Atomic Energy Agency, Vienna, 2008.

[4] G. A. Johansen, "7 - Gamma-ray tomography," in *Industrial Tomography Systems and Applications*, Woodhead Publishing Series in Electronic and Optical Material, 2015, pp. 197-222.

[5] B. T. Hjertaker, "Multiphase Flow Imaging by Dual Mode Tomography," Department of Physics University of Bergen, Bergen, 1998.

[6] CMR Christian Michelsen Research, "CMR Christian Michelsen Research," CMR Christian Michelsen Research, 2016. [Online]. Available: https://www.cmr.no/projects/10503/gamma-ray-tomographer/. [Accessed 9 July 2019].

[7] R. S. B. H. R.B Spelay. S.A. Hashemi, "Improved backscatter correction model for high attenuation gamma-ray tomography measurements," *ISIPT - The International Society for Industrial Process Tomography ,* p. 12, 2-6 September 2018.

[8] I. Meric, G. A. Johansen and I. V. M. Moreira d, "A library least-squares approach for scatter correction in gamma-ray tomography," *Radiation Physics and Chemistry Elsevier ,* vol. l, no. 108, p. 39–47, 2015.

[9] R. Maad, B. T. Hjertaker and G. A. Johansen, "Semi-empirical scatter correstion model for high-speed gammaa-ray tomography," *IOP Publishing,* p. 6, 24 July 2008.

[10] W. R. Leo, Techniques for Nuclear and Particle Physics Experiments A How-to Approach, La Tour de Peilz: Springer-Verlag Berlin Heidelberg GmbH, 1993.

[11] G. F. Knoll, "Radiation Detection and Measurment Third Edition," John Wiley & Sons, Inc., New York/Chichester/Weinheim/Brisbane/Toront/Singapore, 2009.

[12] H. D. Young and R. A. Freedman, University Physics with Modern Physics 14th Edition, Edinburgh: Pearson Education Limited, 2016.

[13] NASA Science, "NASA Science," NASA Science, 10 August 2016. [Online]. Available: https://science.nasa.gov/ems/02_anatomy. [Accessed 7 June 2019].

[14] T. Frøystein, "Gamma-ray flow imaging," Department of Physics University of Bergen, Bergen, 1992.

[15] D. Røhrich, "Lecture Notes PHYS231 Radiation Physics," UIB, Bergen, 2019.

[16] HyperPhysics, "HyperPhysics," HyperPhysics, August 2000. [Online]. Available: http://hyperphysics.phy-astr.gsu.edu/hbase/ems3.html. [Accessed Thursday June 2019].

[17] F. M. Khan and J. P. Gibbons, KHAN'S The Physics of Radiation Therapy Edition 5, Philadelphia: Wolters Kluwer, 2014.

[18] T. F. Thorsteinsen, "PHYS231 Kompendiet," Fysikk institutt - Universitet i Bergen, Bergen, 1995.

[19] B. T. Hjertaker, R. Maad, E. Schuster, O. A. Almås and G. A. Johansen, "A data aquisition and control system for high-speed gamma-ray tomography," IOP Publishing, Bergen, 2008.

[20] M. L. L'annunziata, Radioactivity (2nd ed.) Introduction and History, From the Quantum to Quark, Amsterdam Boston Heidelberg London New York Oxford Paris San Diego San Francisco Singapore Sydney Tokyo: Elsevier , 2016.

[21] R. Halmshaw, Introduction to the Non-Destructive Testing Non-Destructive Testing Second Edition, Cambridge: ABINGTON PUBLISHING Woodhead Publishing Ltd in association with The Welding Institute , 1996.

[22] G. Manzo, S. Giarrusso, A. Santangelo, F. Ciralli, G. Fazio, S. Piraino and A. Segreto, "The high pressure gas scintillation proportional counter on-board the BeppoSAX X-ray astronomy satellite," *ASTRONOMY & ASTROPHYSICS SUPPLEMENT SERIES Astron. Astrophys. Suppl. Ser. 122, 341-356 (1997),* vol. II, no. 122, pp. 341-356, 1997.

[23] H. Hirayama, "Lecture Note on Photon interactions and Cross Sections," KEK, High Energy Accelerator Research Organization 1-1, Oho, Tsukuba, Ibaraki, 305-0801 Japan, Tsukuba, 2000.

[24] J. H. Hubbell, "Photon Cross Sections, Attenuation Coefficients, and Energy Absorbation Coefficients From 10 keV to 100 GeV," U.S. Department Of Commerce National Bureau Of Standards, Washington, D.C, 1969.

[25] P. Sprawls, "The physical Principles of Medical Imaging online book," Sprawls Educational Foundation, [Online]. Available: http://www.sprawls.org/ppmi2/INTERACT/. [Accessed 20 June 2019].

[26] J. Chou, "LibreTexts," LibreTexts, 5 June 2019. [Online]. Available: https://chem.libretexts.org/Bookshelves/Physical_and_Theoretical_Chemistry_Textbook_Maps/Supplemental_Modules_(Physical_and_Theoretical_Chemistry)/Nuclear_Chemistry/Radioactivity/The_Effects_of_Radiation_on_Matter. [Accessed 20 June 2019].

[27] K. S. Krane, Introductory Nuclear Physics, New York Chichester Brisbane Toronto Singapore: John Wiley & Sons, 1987.

[28] D. Halliday, R. Resnick and J. W. Walker, Fundamentals of Physics 9th Edition, Danvers: John Wiley & Sons, Inc., 2012.

[29] S. H. Byun, "Med Phys 4R06/6R03 Radioisotopes and Radiation Methodology Radioisotopes and Radiation Methodology Lecture Notes (Version 2016-17)," Department of Medical Physics & Applied Radiation Sciences McMaster University, Hamilton, 2016.

[30] J. Coderre, "Principles of Radiation Interactions Lecture notes MIT Course Number 22.55J / HST.560J," MIT OpenCourseWar, Massachusetts, 2004.

[31] B. Ostle, Statics In Research, Ames: The Iowa State Univeristy Press, 1963.

[32] G. A. Johansen,, T. Frøystein, B. T. Hjertaker and Ø. Olsen, "A dual sensor flow imaging," *Meas. Sci. Technol.,* vol. 7, no. 1, p. 297–307, 1996.

[33] G. A. Johansen, I. Meric, R. Maad, E. M. Bruvik, B. T. Hjertaker and C. Sætre, "Non-Destructive Monitoring of Multiphase Hydrocarbon Flow by HighSpeed Gamma-Ray Tomograph," in *11th European Conference on Non-Destructive Testing (ECNDT 2014)*, Prague, 2014.

[34] K. Røed, "Fluka simulation results for the UiB gamma-ray tomography system," Department of physics and technology, University of Bergen, Bergen, 2012.

[35] X-5 Monte Carlo Team, "MCNP — A General Monte Carlo N-Particle Transport Code, Version 5," Los Alamos National Laboratory, California, 2003.

[36] H. E. S. Pettersen, "A Digital Tracking Calorimeter A Digital Tracking Calorimeter Tomography (PhD)," University of Bergen, Bergen, 2018.

[37] C. J. Werner, J. Armstrong, F. B. Brown, L. Casswell, L. J. Cox, D. Dixon, R. A. Forster, J. T. Goorley, H. G. Hughes, J. Favorite and R. Martz, "MCNP6.2-EXE Monte Carlo N–Particle Transport Code System Version 6.2 EXE-ONLY," Los Alamos National Laboratory, Los Alamos, New Mexico. RADIATION SAFETY INFORMATION COMPUTATIONAL CENTER, New Mexico, 2017.

[38] Los Alamos National Laboratory, "MCNP6.2-EXE Monte Carlo N–Particle® Transport Code System Version 6.2 EXE-ONLY MCNP® USER'S MANUAL," RADIATION SAFETY INFORMATION COMPUTATIONAL CENTER U.S. DEPARTMENT OF ENERGY, Los Alamos, 2017.

[39] D. A. Boston, "Introduction to MCNP - the monte carlo transport code V1.4," University of Liverpool, Liverpool, 2014.

[40] J. K. Shultis and R. E. Faw, "AN MCNP Primer," Dept. of Mechanical and Nuclear Engineering Dept. of Mechanical and Nuclear Engineering, Manhattan, 2004.

[41] M. Stilling, "Polyethylene wear analysis experimental and clinical studies in total hip replacement Phd Thesis," *ACATA ORTOPAEDICA SUPPLEMENTUM,* vol. 80, no. 337, 2009.

[42] K. A. Van Riper, "Moritz User's Guide Windows Version," White Rock Science, White Rock, 2000.

[43] National Instruments, "National Instruments," National Instruments, 2019. [Online]. Available: https://www.ni.com/en-us/shop/labview.html. [Accessed 28 July 2019].

[44] MathWorks, "MathWorks," MathWorks, 2019. [Online]. Available: https://se.mathworks.com/discovery/what-is-matlab.html. [Accessed 28 July 2019].

[45] University of Delaware, "Using X-windows (X11) and secure shell (SSH) to connect to a remote UNIX server (host)," University of Delaware, 2012. [Online]. Available: http://www1.udel.edu/it/research/training/config_laptop/puTTY.shtml . [Accessed 28 July 2019].

[46] United States Environmental Protection Agency, "United States Environmental Protection Agency," United States Environmental Protection Agency, 15 February 2018. [Online]. Available: https://www.epa.gov/radiation/protecting-yourself-radiation. [Accessed 8 April 2019].

[47] J. P. Bently, Principles of Measrument Systems Fourth Edition, Edinburgh: Pearson, 2005.

[48] R. P. Gardner, J. Wang, L. Xu and A. Sood, "SOME LESSONS LEARNED FROM MCNP USAGE," Los Alamos National Laboratory, North Carolina, 2007.

[49] G. A. Johansen, "7 Gamma-ray tomography," Elsevier Ltd, Bergen, 2015.

[50] M. L. Kutner, Astronomy A Physical Perspective Second Edition, Cambridge: Cambridge University Press, 2003.

[51] WebFinance Inc. , "Businessdictionary.," WebFinance Inc. , 2019. [Online]. Available:

http://www.businessdictionary.com/definition/probabilistic.html. [Accessed 2 April 2019].

[52] O. Doron, "Simulation of an INS Soil Analysis System," The University of Texas at Austin , Austin, 2007.

[53] K. Buchtela and J. Reedijk, "Reference Module in Chemistry, Molecular Sciences and Chemical Engineering," Elsevier, 2014.

[54] L. Hegenbart, "Numerical Efficiency Calibration of in Vivo Measurement Systems," KIT Scientific Publishing, Karlsruhe, 2009.

[55] B. E. Bakkari, "The Monte Carlo simulation of a Package formed by the combination of three scintillators: Brillance380, Brillance350, and Prelude420.," EURONS I3 506065 JRA9 – RHIB Report made during stay IEM-CSIC Madrid december 2006 , Madrid, 2006.

[56] D. E. Hussein, "Monte Carlo Particle Transport with MCNP," Department of Mechanical Engineering University of New Brunswick, Fredericton.

[57] "Hyper Physics," Hyper Physics, August 2000. [Online]. Available: http://hyperphysics.phy-astr.gsu.edu/hbase/electric/elefie.html. [Accessed 7 June 2019].

[58] Hyper Physics, "Hyper Physics," Hyper Physics, August 2000. [Online]. Available: http://hyperphysics.phy-astr.gsu.edu/hbase/electric/farlaw.html. [Accessed 7 June 2019].

[59] B. Povh, K. Rith, ·. C. Scholz and F. Zetsche, Particles and Nuclei An Introduction to the Physical Concepts, Berlin Heidelberg: Springer, 2008.

[60] E. STORM and H. I. ISRAEL, "PHOTON CROSS SECTIONS FROM 1 KEV TO 100 MEV," Los Alamos Scientific Laboratory, University of California , New Mexico, 1970.

[61] E. Malinen, "Interaction theory – Photons," University of Oslo Department of Physics, Oslo.

Appendix A

```
UiB GRT - Compton Scatter
c        1         2         3         4         5         6         7         |
c
c  Date: 25.02.2019
c  Author: Frida Jogole Sandtorv (fjo015@uib.no)
c
c When testing Em with higher density, no change is needed since this phantom only contains air
c Problem cells
c This file is a new verison of 42empi
1   0    1   imp:p=0  $ Outer world
2   0    -1    #3 #4 #444 #555 #666 #42 #43 #44 #45 #46 imp:p=1 $ Inner world
3   1   -1.38  2  -3 -4  5  imp:p=1 $ PVC pipe
c 3   1   -1.38  -2  -1  imp:p=1 $ PVC pipe
4   2   -5.78  6 -7  8 -9  10 -11  imp:p=1 u=2 $ Central CZT det 1
444 3  -0.001205 14 -7 -51 -53 17 -18 $ Cell 42 filled with air
      #4 #7 #8 #9 #10 #11 #12 #13 #14 #15 #16 #17 #18 #19 #20 #21 #22
      #23 #24 #25 #26 #27 #28 #29 #30 #31 #32 #33 #34 #35 #36 #37 #38 #39
      #40 #771 #772 #773 #774 #775 #776 #777 #778 #779 #780 #781 #782 #783 #784 #785 #786 #787 imp:p=1 u=2 $ Renmove coll and det so that only air between collimator and detectors if left
555   3   -0.001205  -125 -4 5          imp:p=1 $ Empty pipe, 100% Air
666   3   -0.001205   125 -2 -45 -4 5   imp:p=1 $ Volume between phantom and pipe is filled with Air, air gap
c 5   5   -0.92   125 -126 -2 -4 5      imp:p=1 $ No air gap between phantom and pipe
c 6   5   -0.92  -125 -126 -4 5          imp:p=1 $ Half polypropylene phantom
7   like 4 but trcl=1  imp:p=1 u=2 $ CZT det 2
8   like 4 but trcl=2  imp:p=1 u=2 $ CZT det 3
9   like 4 but trcl=3  imp:p=1 u=2 $ CZT det 4
10  like 4 but trcl=4  imp:p=1 u=2 $ CZT det 5
11  like 4 but trcl=5  imp:p=1 u=2 $ CZT det 6
12  like 4 but trcl=6  imp:p=1 u=2 $ CZT det 7
13  like 4 but trcl=7  imp:p=1 u=2 $ CZT det 8
14  like 4 but trcl=8  imp:p=1 u=2 $ CZT det 9
15  like 4 but trcl=9  imp:p=1 u=2 $ CZT det 10
```

```
16  like 4 but trcl=10 imp:p=1 u=2 $ CZT det 11
17  like 4 but trcl=11 imp:p=1 u=2 $ CZT det 12
18  like 4 but trcl=12 imp:p=1 u=2 $ CZT det 13
19  like 4 but trcl=13 imp:p=1 u=2 $ CZT det 14
20  like 4 but trcl=14 imp:p=1 u=2 $ CZT det 15
21  like 4 but trcl=15 imp:p=1 u=2 $ CZT det 16
22  like 4 but trcl=16 imp:p=1 u=2 $ CZT det 17
23  6  -11.35  -13 14 -15 16 17 -18  imp:p=1 u=2 $ Collimator blade 1
24  6  -11.35  -13 14 -21 22 17 -18  imp:p=1 u=2 $ Collimator blade 2
25  6  -11.35  -13 14 -23 24 17 -18  imp:p=1 u=2 $ Collimator blade 3
26  6  -11.35  -13 14 -25 26 17 -18  imp:p=1 u=2 $ Collimator blade 4
27  6  -11.35  -13 14 -27 28 17 -18  imp:p=1 u=2 $ Collimator blade 5
28  6  -11.35  -13 14 -29 30 17 -18  imp:p=1 u=2 $ Collimator blade 6
29  6  -11.35  -13 14 -31 32 17 -18  imp:p=1 u=2 $ Collimator blade 7
30  6  -11.35  -13 14 -33 34 17 -18  imp:p=1 u=2 $ Collimator blade 8
31  6  -11.35  -13 14 -35 36 17 -18  imp:p=1 u=2 $ Collimator blade 9
32  6  -11.35  -13 14 -37 38 17 -18  imp:p=1 u=2 $ Collimator blade 10
33  6  -11.35  -13 14 -39 40 17 -18  imp:p=1 u=2 $ Collimator blade 11
34  6  -11.35  -13 14 -41 42 17 -18  imp:p=1 u=2 $ Collimator blade 12
35  6  -11.35  -13 14 -43 44 17 -18  imp:p=1 u=2 $ Collimator blade 13
36  6  -11.35  -13 14 -45 46 17 -18  imp:p=1 u=2 $ Collimator blade 14
37  6  -11.35  -13 14 -47 48 17 -18  imp:p=1 u=2 $ Collimator blade 15
38  6  -11.35  -13 14 -49 50 17 -18  imp:p=1 u=2 $ Collimator blade 16
39  6  -11.35  -13 14 -51 52 17 -18  imp:p=1 u=2 $ Collimator blade 17
40  6  -11.35  -13 14 -53 54 17 -18  imp:p=1 u=2 $ Collimator blade 18
771   6  -11.35  -13 14 -55 56 17 -18  imp:p=1 u=2 $ Collimator blade 19 Starting
point for mid collimator around 8cm =8,1cm and 7,9cm
772   6  -11.35  -13 14 -57 58 17 -18  imp:p=1 u=2 $ Collimator blade 20
773   6  -11.35  -13 14 -59 60 17 -18  imp:p=1 u=2 $ Collimator blade 21*
774   6  -11.35  -13 14 -61 62 17 -18  imp:p=1 u=2 $ Collimator blade 22*
775   6  -11.35  -13 14 -63 64 17 -18  imp:p=1 u=2 $ Collimator blade 23*
776   6  -11.35  -13 14 -65 66 17 -18  imp:p=1 u=2 $ Collimator blade 24*
777   6  -11.35  -13 14 -67 68 17 -18  imp:p=1 u=2 $ Collimator blade 25*
778   6  -11.35  -13 14 -69 70 17 -18  imp:p=1 u=2 $ Collimator blade 26*
779   6  -11.35  -13 14 -71 72 17 -18  imp:p=1 u=2 $ Collimator blade 27*
780   6  -11.35  -13 14 -73 74 17 -18  imp:p=1 u=2 $ Collimator blade 28*
781   6  -11.35  -13 14 -75 76 17 -18  imp:p=1 u=2 $ Collimator blade 29*
782   6  -11.35  -13 14 -77 78 17 -18  imp:p=1 u=2 $ Collimator blade 30*
783   6  -11.35  -13 14 -79 80 17 -18  imp:p=1 u=2 $ Collimator blade 31*
784   6  -11.35  -13 14 -81 82 17 -18  imp:p=1 u=2 $ Collimator blade 32*
785   6  -11.35  -13 14 -83 84 17 -18  imp:p=1 u=2 $ Collimator blade 33*
786   6  -11.35  -13 14 -85 86 17 -18  imp:p=1 u=2 $ Collimator blade 34*
```

```
787   6  -11.35  -13 14 -87 88 17 -18  imp:p=1 u=2 $ Collimator blade 35*
c 41  3  -0.001205  -2 126 -4 5  imp:p=1 $ Half air phantom
42  0  14 -7 -51 -53 17 -18 imp:p=1 fill=2 $ assembly pentant 1
43 like 42 but *trcl=(0 0 0 72 90 162 90 0 90 18 90 72) $ pentant 2
44 like 42 but *trcl=(0 0 0 144 90 234 90 0 90 54 90 144) $ pentant 3
45 like 42 but *trcl=(0 0 0 216 90 306 90 0 90 126 90 216) $ pentant 4
46 like 42 but *trcl=(0 0 0 288 90 18 90 0 90 198 90 288) $ pentant 5

c  Problem surfaces
1  so  100.0  $ Inner/outer world
2  cy  4.065  $ Pipe inner radius boundary. 10% bigger:  2  cy  4.4715 . original:
2 cy  4.065   5%bigger 4.2683
3  cy  4.415  $ Pipe outer radius boundary.  10% bigger:  3  cy  4.8565  . original:3
cy  4.415  5%bigger 4.6358
4  py  50.0   $ Pipe upper plane boundary
5  py -50.0   $ Pipe lower plane boundary
6  pz  22.0   $ Lower z-extension of CZT det
7  pz  22.2   $ Upper z-extension of CZT det
8  px -0.5   $ Lower x-extension of CZT det
9  px  0.5   $ Upper x-extension of CZT det
10 py -0.5   $ Lower y-extension of CZT det
11 py  0.5   $ Upper y-extension of CZT det
c 12 c/y 0.0 0 1.0   $ Gas bubble radius
13  pz  21.7  $ Upper z-extension of lead blade collimator
14  pz  15.7  $ Lower z-extension of lead blade collimator
15  p  3.4783 0 -0.04545 1   $ Upper x-extension of lead blade collimator
16  p  4.2105 0 -0.04545 1   $ Lower x-extension of lead blade collimator
17  py -1.0   $ Lower y-extension of lead blade collimator
18  py  1.0   $ Upper y-extension of lead blade collimator
21  p  -3.4783 0 -0.04545 1  $ Upper x-extension of lead blade collimator
22  p  -4.2105 0 -0.04545 1   $ Lower x-extension of lead blade collimator
23  p   1.2308 0 -0.04545 1
24  p   1.3115 0 -0.04545 1
25  p  -1.2308 0 -0.04545 1
26  p  -1.3115 0 -0.04545 1
27  p   0.7442 0 -0.04545 1
28  p   0.773  0 -0.04545 1
29  p  -0.7442 0 -0.04545 1
30  p  -0.773  0 -0.04545 1
31  p   0.5333 0 -0.04545 1
32  p   0.548  0 -0.04545 1
33  p  -0.5333 0 -0.04545 1
```

```
34  p  -0.548  0 -0.04545 1
35  p   0.4156 0 -0.04545 1
36  p   0.4244 0 -0.04545 1
37  p  -0.4156 0 -0.04545 1
38  p  -0.4244 0 -0.04545 1
39  p   0.3404 0 -0.04545 1
40  p   0.3463 0 -0.04545 1
41  p  -0.3404 0 -0.04545 1
42  p  -0.3463 0 -0.04545 1
43  p   0.2878 0 -0.04545 1
44  p   0.292  0 -0.04545 1
45  p  -0.2878 0 -0.04545 1
46  p  -0.292  0 -0.04545 1
47  p   0.2488 0 -0.04545 1
48  p   0.252  0 -0.04545 1
49  p  -0.2488 0 -0.04545 1
50  p  -0.252  0 -0.04545 1
51  p   0.22   0 -0.04545 1
52  p   0.2222 0 -0.04545 1
53  p  -0.22   0 -0.04545 1
54  p  -0.2222 0 -0.04545 1
55  p   0.2337 0 -0.04545 1 $ outer plane at 8.0cm. 8  Middel of first detector=8cm
equal to gradient of -0.23375
56  p   0.2367 0 -0.04545 1 $ inner plane at 7.90cm 7,90 plane new -0.236
57  p   0.2671 0 -0.04545 1 $ outer plane at 7.0cm
58  p   0.2710 0 -0.04545 1 $ inner plane at 6.90cm
59  p   0.3116 0 -0.04545 1 $ outer plane at 6.00cm
60  p   0.3169 0 -0.04545 1 $ inner plane at 5.90cm
61  p   0.374 0 -0.04545 1  $outer plane at 5.00cm
62  p   0.3816 0 -0.04545 1 $inner plane at 4.90cm
63  p   0.4675 0 -0.04545 1 $outer plane at 4.00cm
64  p   0.4795 0 -0.04545 1 $inner plane at 3.90cm
65  p   0.6233 0 -0.04545 1 $outer plane at 3.00cm
66  p   0.6448 0 -0.04545 1 $inner plane at 2,90cm
67  p   0.935 0 -0.04545 1  $outer plane at 2.0cm
68  p   0.9842 0 -0.04545 1 $inner plane at 1.90cm
69  p   1.87 0 -0.04545 1 $outer plane at 1.00cm
70  p   2.0777 0 -0.04545 1 $inner plane at 0.90cm
71 px 0.05 $ mid collimator blades 0,5cm
72 px -0.05 $ mid collimator blades 0,5cm
73  p  -0.2337 0 -0.04545 1 $ outer plane at 8.0cm. 8  Middel of first detector=8cm
equal to gradient of -0.23375
```

```
74  p   -0.2367 0 -0.04545 1 $ inner plane at 7.90cm 7.90 plane new -0.236
75  p   -0.2671 0 -0.04545 1 $ outer plane at 7.0cm
76  p   -0.2710 0 -0.04545 1 $ inner plane at 6.90cm
77  p   -0.3116 0 -0.04545 1 $ outer plane at 6.00cm
78  p   -0.3169 0 -0.04545 1 $ inner plane at 5.90cm
79  p   -0.374 0 -0.04545 1  $outer plane at 5.00cm
80  p   -0.3816 0 -0.04545 1 $inner plane at 4.90cm
81  p   -0.4675 0 -0.04545 1 $outer plane at 4.00cm
82  p   -0.4795 0 -0.04545 1 $inner plane at 3.90cm
83  p   -0.6233 0 -0.04545 1 $outer plane at 3.00cm
84  p   -0.6448 0 -0.04545 1 $inner plane at 2.90cm
85  p   -0.935 0 -0.04545 1  $outer plane at 2.0cm
86  p   -0.9842 0 -0.04545 1 $inner plane at 1.90cm
87  p   -1.87 0 -0.04545 1 $outer plane at 1.00cm
88  p   -2.0777 0 -0.04545 1 $inner plane at 0.90cm
c 55  p  -0.9510 0 0.309 22
125 cy cy 3.9975    $ Phantom diameter. 5%bigger 125 cy 4.1974. 10% bigger: 125
cy 4.39725 . original:125 cy 3.9975
126 17 px 0.0       $ Half-cylinder phantom, Plane that cuts cylinger in half

mode p
RAND seed=19073486328121; GEN=4
c Data cards
c phys:p j j 1 j j j j  $ Coherent scattering is turned off, removes rayleigh
c Pipe Wall - (PVC C2H3Cl rho=1.38 g/cm^3)
m1    6000              -0.3843600     $ C
      1000              -0.0483802     $ H
      17000             -0.5672598     $ Cl
c CdZnTe crystal (rho=5.78 g/cm^3)
m2    48000.              0.4          $ Cd
      30000.              0.1          $ Zn
      52000.              0.5          $ Te
c Air
m3    7000.              -0.7553        $ N
      8000.              -0.2318        $ O
      18000.             -0.0128        $ Ar
      6000               -0.0001        $ C
c Water
m4    1000.              -0.111898      $ H
      8000.              -0.888102      $ O
c Polypropylene, original rho = 0.9 g/cc, new rho = 0.92 g/cc, Phantom material
m5    1000.              -0.143711      $ H
```

```
      6000.              -0.856289       $ C
c Lead, rho = 11.35 g/cc
m6    82000.             -1.00           $ Pb
sdef: erg=0.0595 pos=0 0 -22.0 axs=0 0 1 ext=0 rad=d1 dir=d2 vec=0 0 1 par=p
$ Source42, source directed towards pent42/pent1
si1 0  0.9
sp1 -21  1
si2 -1.0  0.97  1
sp2  0 0.95  0.05
sb2  0.  0.   1.
c Transformations begin, used for positioning the 17 detectors. They are used in
cells 7-22.
*tr1  1.05 0 0
*tr2  2.1 0 0
*tr3  3.175 0 0
*tr4  4.225 0 0
*tr5  5.3 0 0
*tr6  6.35 0 0
*tr7  7.45 0 0
*tr8  8.525 0 0
*tr9  -1.05 0 0
*tr10 -2.1 0 0
*tr11 -3.175 0 0
*tr12 -4.225 0 0
*tr13 -5.3 0 0
*tr14 -6.35 0 0
*tr15 -7.45 0 0
*tr16 -8.525 0 0
*tr17  0 0 0  288 90 -198
f428:p (14 13 12 11 10 9 8 7 4 15 16 17 18 19 20 21 22 <42) $ cell 4 to 22 in 42
f438:p (14 13 12 11 10 9 8 7 4 15 16 17 18 19 20 21 22 <43) $
f448:p (14 13 12 11 10 9 8 7 4 15 16 17 18 19 20 21 22 <44) $
f458:p (14 13 12 11 10 9 8 7 4 15 16 17 18 19 20 21 22 <45) $
f468:p (14 13 12 11 10 9 8 7 4 15 16 17 18 19 20 21 22 <46) $
e428 0  1.0e-5 0.001 0.048 0.0596
e438 0  1.0e-5 0.001 0.048 0.0596
e448 0  1.0e-5 0.001 0.048 0.0596
e458 0  1.0e-5 0.001 0.048 0.0596
e468 0  1.0e-5 0.001 0.048 0.0596
c e428 0 1.0e-6 0.001 1022i 1.0
c ft18 geb 1.0210e-2  1.8280e-3  3.7310e+0
c f421:p 6 $ Surface
```

```
c f431:p (6<43) $ Surface 4 in cell 43
c f441:p (6<44) $ Surface
c f451:p (6<45) $ Surface
c f461:p (6<46) $ Surface
c e421 0 1E-5 0.01 0.02 0.03 0.04 0.05 0.055 0.056 0.057 0.058 0.059 0.0594 0.0596
0.06
c e431 0 1E-5 0.01 0.02 0.03 0.04 0.05 0.055 0.056 0.057 0.058 0.059 0.0594 0.0596
0.06
c e441 0 1E-5 0.01 0.02 0.03 0.04 0.05 0.055 0.056 0.057 0.058 0.059 0.0594 0.0596
0.06
c e451 0 1E-5 0.01 0.02 0.03 0.04 0.05 0.055 0.056 0.057 0.058 0.059 0.0594 0.0596
0.06
c e461 0 1E-5 0.01 0.02 0.03 0.04 0.05 0.055 0.056 0.057 0.058 0.059 0.0594 0.0596
0.06
c f14:p 4 7 8 9 10 11 12 13 14 15 16 17 18 19 20 21 22
c e14 0.0 0.048 0.06
c ft14 inc
c fu14 0 1.0e+5 t
print 110
nps 1.0e+8  $nps 2.0e+9
```